JIMMA UNIVERSITY

JIMMA INSTITUTE OF TECHNOLOGY

FACULTY OF MECHANICAL ENGINEERING

SUSTAINABLE ENERGY ENGINEERING STREAM

Transient Performance Analysis of Solar Dish Concentrator Integrated with Stirling and Thermoelectric Generator for Small-Scale Irrigation System

A Thesis Submitted to the School of Graduate Studies of Jimma University in partial fulfillment of the requirements for the award of Masters of Science in Sustainable Energy Engineering

By:

Endeshaw Alemu

January 2021

Jimma, Ethiopia

JIMMA UNIVERSITY

JIMMA INSTITUTE OF TECHNOLOGY

FACULTY OF MECHANICAL ENGINEERING

SUSTAINABLE ENERGY ENGINEERING STREAM

Transient Performance Analysis of Solar Dish Concentrator Integrated with Stirling and Thermoelectric Generator for Small-Scale Irrigation System

A Thesis Submitted to the School of Graduate Studies of Jimma University in partial fulfillment of the requirements for the award of Masters of Science in Sustainable Energy Engineering

By:

Endeshaw Alemu

Main advisor: Prof. A. Venkata Ramayya (PhD)

Co-advisor: Tarekegn Limore (MSc)

January 2021

Jimma, Ethiopia

DECLARATION

I, the undersigned, declare that this thesis entitled **"Transient Performance Analysis of Solar Dish Concentrator Integrated with Stirling and Thermoelectric Generator for Small-Scale Irrigation System"** is my original work and has not been presented by any other person for an award of a degree in this or any other University, and any information or materials used in the thesis from external sources has been appropriately acknowledged.

Endeshaw Alemu	_____	_____
Candidate	**Signature**	**Date**

This thesis has been submitted for examination with our approval.

Prof. Dr. A. Venkata Ramayya	_____	_____
Main Advisor	**Signature**	**Date**
Tarekegn Limore (MSc)	_____	_____
Co–advisor	**Signature**	**Date**

JIMMA UNIVERSITY

JIMMA INSTITUTE OF TECHNOLOGY

FACULTY OF MECHANICAL ENGINEERING

SUSTAINABLE ENERGY ENGINEERING STREAM

Approval sheet

This is to certify that the thesis entitled " **Transient Performance Analysis of Solar Dish Concentrator Integrated with Stirling and Thermoelectric Generator for Small-Scale Irrigation System** " submitted by Endeshaw Alemu to the Faculty of Mechanical Engineering, Jimma Institute of Technology for the award of the degree of Master of Science in Sustainable Energy Engineering is carried out by him under our supervision. This thesis is being submitted, having met all the requirements, and hereby approved.

Prof. Dr. A. Venkata Ramayya	_____	_____
Main Advisor	**Signature**	**Date**
Tarekegn Limore (MSc)	_____	_____
Co–advisor	**Signature**	**Date**

Board of examiners

Dr.Ing. Getachew S. Tibba	_____	_____
External Examiner	**Signature**	**Date**
Eshetu Tadesse (MSc)	_____	_____
Internal Examiner	**Signature**	**Date**
Tarekegn Limore (MSc)	_____	_____
Chairperson	**Signature**	**Date**

ACKNOWLEDGEMENT

Above all, I would like to acknowledge the Almighty God for his guidance and wisdom throughout my journey. I am pleased to express my gratitude to my main advisor Prof. Dr A. Venkata Ramayya, for his supervision, guidance, encouragement, and steadfast support throughout the accomplishment of this research work. My most profound appreciation also goes to my co-advisor, Tarekegn Limore (MSc), for his valuable and constructive comments. I want to express my special thanks to Balewgize Amare (PhD. candidate and Asst. professor) for his guidance during the title's development.

I offer my regards to Jimma Institute of Technology, Mechanical Engineering Department for the enormous support and sponsoring me on the MSc program in sustainable energy engineering. It is my utmost honor to appreciate all my lecturers for their tireless effort, and knowledge's during my study period at Jimma Institute of Technology.

Finally, I would like to express my deepest gratitude, humble respect, and special thanks to my parents for being with me, always by moral and financially. Without their support, the accomplishment of this work indeed would not have been possible.

ABSTRACT

Solar energy is aspired to be one of the most promising sources of energy in the future due to the step-up depletion of fossil fuels. Nowadays, solar irrigation technologies play a vital role in enhancing poverty and food insecurity in a developing country. This thesis presents a transient performance analysis of a solar dish concentrator integrated with Stirling and a thermoelectric generator for the small-scale irrigation system.The estimation of solar radiation was carried out based on the sunshine hour model using Angstrom-Prescott Correlation. The predicted solar data is compared with different software packages, and the site has a remarkable solar radiation for an irrigation system. EES code is used for design calculation and performance analysis of solar dish concentrator at different operating parameters. Increasing beam solar radiation increases outlet fluid temperature, useful heat, and thermal efficiency of the concentrator. At 1000 W/m^2, the outlet fluid temperature and thermal efficiency found to be 488.2 K and 81.23%, respectively. On the other hand, heat flux and temperature distribution at the concentrator focal plane are carried out through SolTrace and COMSOL software. The thermoelectric module is coupled at the top of the concentrator receiver, and the hot side of the module is utilized to harvest useful heat. The Multiphysics analysis shows that at the operational temperature of 488.15K on the hot side of the module, TEG's maximum conversion efficiency achieved is 5.366% with a 0.7256 figure of merit. Transient performance prediction of the thermal Stirling pump was carried out for the selected irrigation period, and thermal efficiency of the Stirling reaches a maximum in May with 18.61%. The Stirling output power and pump flow rate varies with a solar time, and the maximum found at noontime for all selected irrigation season.The system simultaneously provides 11.01 W electrical power through TEG at electrical efficiency of 3.715% and a flow rate of 3.917 m^3/hr through a thermal Stirling pump at a thermal efficiency of 27.93% for a given heat source temperature of 488.15 K. Life cycle cost analysis is performed to compare the proposed system with solar PV and diesel water pumping systems. The result shows that the proposed system is an appropriate and economically feasible for small scale irrigation system.

Keywords: Dish concentrator, Heat flux, Multiphysics, Small-scale irrigation, Stirling pump, Thermoelectric

TABLE OF CONTENTS

LIST OF TABLES

LIST OF FIGURES

NOMENCLATURE

A	Area	m^2
C	Concentration ratio	-
C_p	Specific heat capacity at constant pressure	J/ (kg. K)
C_v	Specific heat capacity at constant volume	J/ (kg. K)
D	Diameter	m
EoT	Equation of time	-
f	Focal length	m
g	Gravitational acceleration	m/s^2
H_T	Total dynamic head	m
h	Heat transfer coefficient	W/ (m.K)
I	Solar irradiance	W/m^2
L	Length	m
m	Mass flow rate	kg/s
P_H	Hydraulic power	W
P_{OUT}	Output power	W
P_{shaft}	Shaft power	W
Q	Flow rate (discharge)	m^3/s
Q_h	Heat supplied to Stirling engine	KJ
Q_{LT}	Total heat loss	W
Q_R	Heat absorbed by the receiver	W
Q_S	Heat supplied	W
Q_U	Useful heat	W
r_r	Rim radius	m
s	Arch length	m
S_{opt}	Optimum spacing of heat sink	m
T	Temperature	K, ^oC
V_C	Compression space volume	cm^3

V_{DC}	Compression space dead volume	cm^3
V_{DE}	Expansion space dead volume	cm^3
V_E	Expansion space volume	cm^3
V_{SD}	Swept volume of a displacer	cm^3
V_{SP}	Swept volume of the piston	cm^3
V_w	Wind velocity	m/s
W	Work done	W
ZT	Figure of merit	-

SYMBOL

δ_s	Solar azimuthal angle	Degree
η_C	Concentrator efficiency	%
η_{opt}	Optical efficiency	%
$\eta_{TEG,max}$	Maximum conversion efficiency of TEG	%
$\eta_{th,striling}$	Thermal efficiency of the Stirling engine	%
ϕ_r	Rim angle	Degree
k	Thermal conductivity	$Wm^{-1}K^{-1}$
α	See-beck coefficient	VK^{-1}
η	Efficiency	%
ρ	Electrical resistivity	Ωm
α	Altitude angle	Degree
β	Coefficient of thermal expansion	1/K
γ	Azimuthal angle	Degree
ε	Emissivity	-
θ	Acceptance angle	Degree
σ	Stefan Boltzmann constant	$W\ m^{-2}K^{-4}$
ω	Hour angle	Degree
ϕ	Local latitude	Degree

Subscript

c	Cold side	out	Outlet
h	Hot side	a	Aperture
amb	Ambient	conc.	Concentrator
conv.	Convection	c	Compression
rad.	Radiation	k	Cooler
hf	Heat fluid	h	Heater
rec.	Receiver	e	Expansion
cond.	Conduction	r	Regenerator

Abbreviation

COMSOL	COMputer SOLution
CSA	Central Statical Agency
CSP	Concentrated Solar Power
CTC	Cylindrical Trough Collector
DC	Direct Current
GDP	Gross Domestic Product
HFC	Heliostat Field collector
HSTE	Hybrid Solar Thermoelectric Generator
LCC	Life Cycle Cost
LFR	Linear Fresnel
NREL	Renewable energy laboratory
PDA	Power Data Access
PDR	Parabolic Dish Reflector
PTC	Parabolic Trough Collector
PV	Photo-Voltaic
SWERA	Solar and Wind Energy Resource Assessment
TEG	Thermoelectric Generator
UN	United Nation
USAID	United State Agency for International Development

CHAPTER ONE

1. INTRODUCTION

1.1 Background of the study

The estimation shows that by 2050 the global human population will be raised by 2.2 billion, and the global energy demand can be double from now, while water and food demand will be increased by 50% [1, 2]. The increasing number of populations forces many countries to initiate a Water-Energy-Food nexus policy to meet the demand and reduce environmental impact. Furthermore, food insecurity in developing countries necessitates more farming to satisfy the need for reducing poverty in the region [3].

According to the United Nations report released in 2019, the Ethiopian population reaches 110.3 million, and 80% of the population is living in rural areas of the country where their daily activities rely on agriculture with a low level of productivity [4]. The rapid growth of the population number emphasizes the need for sustainable and high-quality access to food. The USAID country profile report released in 2018 shows that the agriculture sector accounts for 40 per cent of GDP and 90 per cent of its export, so agriculture is considered a backbone of a country's economy. Around 85% of the Ethiopian population is engaged in agriculture activities, mainly in a subsistence and rain-fed farming and livestock production [5].

Despite economic development and social improvements, millions of family farmers in Ethiopia are still struggling with food insecurity. Lack of technology adoption by a family farmer often results in the root cause of low agricultural productivity and food insecurity [6]. Traditional mechanism and rain based agriculture activities are mainly affecting the capacity of crop productivity throughout, and most of the independent and small-scale farmers are faced with the problem mostly. The average size of small-scale farms for the independent farmer in the country is between 0.5 to 2 hectares, and even the crop yield and income from the land farm is not enough to feed their family [7]. The contribution of energy in the country's agriculture sector is relatively low, especially in an irrigation system. The majority of farmers in the country practice the river diversion manually and diesel pump technology for the irrigation system.

Even though diesel pumps are better than manual irrigation systems in many ways, farmers do not practice it so far due to the expensive initial investment, high operation cost, and maintenance costs. The rising of fuel price and environmental issues is another impact of this technology that opens the door for alternative irrigation technology. Now a day's, a variety of techniques have been developed using renewable energy as a source of energy from a small scale to an extensive irrigation system. The two most applicable renewable energy for the irrigation systems are solar and wind energy. Since wind energy is based on geographical conditions and limited to a specific location, solar energy has been applied widely for the irrigation system.

Solar energy is a plentiful energy source available all over the world with huge potential. Both solar PV and thermal collectors can be applicable for ground and surface water pumping systems. PV solar uses for pumping systems now a day for irrigation and water supply systems. However, it is not recommended for independent farmers with low income to utilize small-scale irrigation systems due to the expensive initial capital cost of available irrigation technology. Thus, the utilization of appropriate technology for small scale irrigation systems is required to meet those smallholder farmers' necessity.

Generally, the utilization of hybrid energy as an alternative energy source in the agriculture sector will minimize dependence on fossil fuel and reduce energy demand. Providing cost-effective and appropriate technology in an irrigation system enables farmers to improve crop productivity, improving livelihoods, and food security [8, 9]. Furthermore, access to small scale irrigation enables low-income farmers to produce crops more than once a year, generate more income, and improve their food security status [10].

1.2 Motivation

The key constraints to agricultural productivity in Ethiopia are low availability of improved seed, lack of hybrid seed multiplication capacity, lack of irrigation and water constraints [8]. Agriculture is a backbone of the country economy, and it accounts 46.3 % of GDP and 83.9% of exports. But the contribution of irrigation system in a country’s economy is insignificant [6-7]. The agricultural developmental goal is to increase the volume of irrigated land farm. But, initiation and development of irrigation technology in the country is still in infant stage.

The available diesel and solar PV irrigation system is not affordable for small holder farmers in application of small-scale irrigation system. Therefore, designing and developing of reliable, cost effective and environmentally friendly hybrid technology is required for small scale irrigation system in rural and remote area of the country. This paper presents about solar dish concentrator integrated with Stirling and TEG for small scale irrigation system. Majority of the population live in rural area of the country where there is no access to electricity ,and the families farmers still struggling with kerosene lump and they are facing to a health problem. So, the proposed system provides an electrical energy form thermal energy of working fluid through TEG for lighting purposes while the Stirling engine drive the pump for water pumping system. Further, there is no published or reported solar radiation data in selected study area, thus this paper attempt to address the assessment and estimation of solar radiation data for system performance analysis.

1.3 Statement of the problem

The main challenges of irrigation technology in Ethiopia are lack of access and poor economic background of the users for irrigation infrastructure development where the price increment is not affordable for the farmers [8]. The rapid growth of the population increases the demand for food and shortage of food outbreaks throughout a time. Even though a majority of the population practices agricultural activities, the crop yield cannot meet the demand, and food insecurity is still rising. Rain-based agricultural activity mainly affects the crop's productivity, and lack of modern irrigation technology during off-season alleviates the problem. The irrigated land farm in the agriculture sector accounts for less than one per cent of the total agricultural area, and solely surface water uses for irrigation systems [6].

Few of the country's farmers practice diesel and solar pumps for irrigation system during the off-season. The depletion of fossil fuel, intermittence, and initial capital cost discourage the utilization of the technologies, and only a few can practice it. PV solar irrigation technology is also limited so far due to high initial investment cost and reduction of collector performance through a time due to overheating of the panel, dust accumulation, and fluctuation of solar radiation that results around 25% overall losses [11].

By taking into account the performance, cost and environmental issues many researchers focus on designing and developing a solar thermal water pump system for small-scale irrigation. The literature confirmed no specific work reported on a solar dish concentrator system coupled with a thermoelectric generator and a thermal Stirling pump for water pumping application. Previously, a solar parabolic dish integrated with TEG has been studied using a flat plate as an absorbing material to transfer heat into a TEG module that is kept at the concentrator's focal plane. Still, the system's effectiveness and reliability are inherently lower due to losses encountered in the system. So, detailed performance analysis is needed to identify the system's losses by varying different operating parameters.

1.4 Objective

1.4.1 General Objective

The main objective of the study is to analyze the transient performance of a solar dish concentrator integrated with Stirling and a thermoelectric generator for the small-scale irrigation system.

1.4.2 Specific Objective

- To assess and estimate the solar radiation in the study area
- To design parabolic dish receiver coupled with TEG module
- To analyze the solar radiation flux distribution at the receiver, and its effect on temperature distribution at a focal plane of the concentrator using Sol-Trace software
- To analyze and simulate the performance of TEG using COMSOL Multiphysics software
- Design and transient performance prediction of solar thermal Stirling pump

1.5 Significance of the Study

The implication of this study is to make the possibility of using solar thermal energy for the application of small–scale irrigation. The proposed model aims to improve the system's performance and reliability to extend power generation capability. The system provides thermal and electrical energy simultaneously from solar radiation through a parabolic dish concentrator and thermoelectric generator module.

The electric power produced through TEG has stored in a battery for the tracking system, night pumping, and lighting systems. The thermal Stirling engine uses the steam from the concentrator receiver to pump water for irrigation application. The study intends to solve community-based problems by providing eco-friendly and cost-effective appropriate technology for smallholder farmers to allow them for more income generation and resolving the risk associated with rainfall. The proposed system aims to improve food security toward mitigating poverty and promoting sustainable development goals (Water-Energy-Food nexus policy).

1.6 Scope of the Study

The scope of this work is limited to analytical and numerical methods. The study addresses prediction of weather data in selected site, design and performance analyzing of solar dish concentrator using EES code, and solar heat flux and temperature at focal plane of the concentrator using SolTrace software. Multiphysics analyze of thermoelectric generator and transient performance prediction of thermal Stirling pump through second-order is also a part of this work. Furthermore, the study addresses the projection of the proposed for 10 hectares of land farm and economic evaluation of the proposed system in comparison with PV solar and diesel water pumping system . The experimental work is beyond the scope of this research.

1.7 Outline of the Thesis

This thesis report is organized into six main chapters, including the first chapter, which deals with the background of the study, statement of the problem, objective, scope, significance of the study, and outline of the thesis. The second chapter provides insights into the solar irrigation system and a thermoelectric generator. The chapter also gives an overview of the literature related to solar irrigation, solar TEG, and solar dish Stirling engine.

The third chapter presents the study area's location, data collection and analysis methods, description of the proposed model, solar radiation components, and the solar data prediction methods. The fourth chapter provides the design and analysis of the system. The chapter presents design and performance analysis of dish concentrator considering heat losses, analysis of solar radiation flux distribution at the receiver using SolTrace software, performance analysis of TEG, and ideal adiabatic analysis of beta Stirling engine.

The fifth chapter gives the result and discussion. This chapter describes the predicted solar radiation data for the selected site and validates the work with solar data analysis software. Performance analysis of dish concentrator at different operating parameters, flux intensity, and temperature distribution at the receiver of the concentrator was presented. The chapter also describes the Multiphysics simulation of the Stirling engine's TEG and performance simulation by second-order ideal adiabatic analysis. The sixth chapter provides the overall conclusion of the thesis and the recommendation for future work.

CHAPTER TWO

2. LITERATURE REVIEW

2.1 Solar Irrigation System

Solar energy is one of the most abundant and available renewable energy sources in the universe. It is one of the hottest research areas now a day in various applications. Solar irrigation system takes an advantage over others due to inconsistency of available fossil fuel and environmental impact issues. The irrigation system's initiation in the agricultural sector is promoted through time because food insecurity happens due to population growth worldwide. Solar photo-voltaic and solar thermal technology is widely applicable for water pumping systems in the drinking water supply and irrigation system. PV solar pumping was limited from medium to large scale irrigation systems due to expensive initial investment cost. PV makes the system unaffordable for small-scale farmers. Some researchers have come up with solar thermal technology to mitigate the problem and meet many farmers' needs in small-scale irrigation. Regarding reliability and initial investment cost, solar thermal is preferable than that of PV solar small-scale irrigation systems [11].

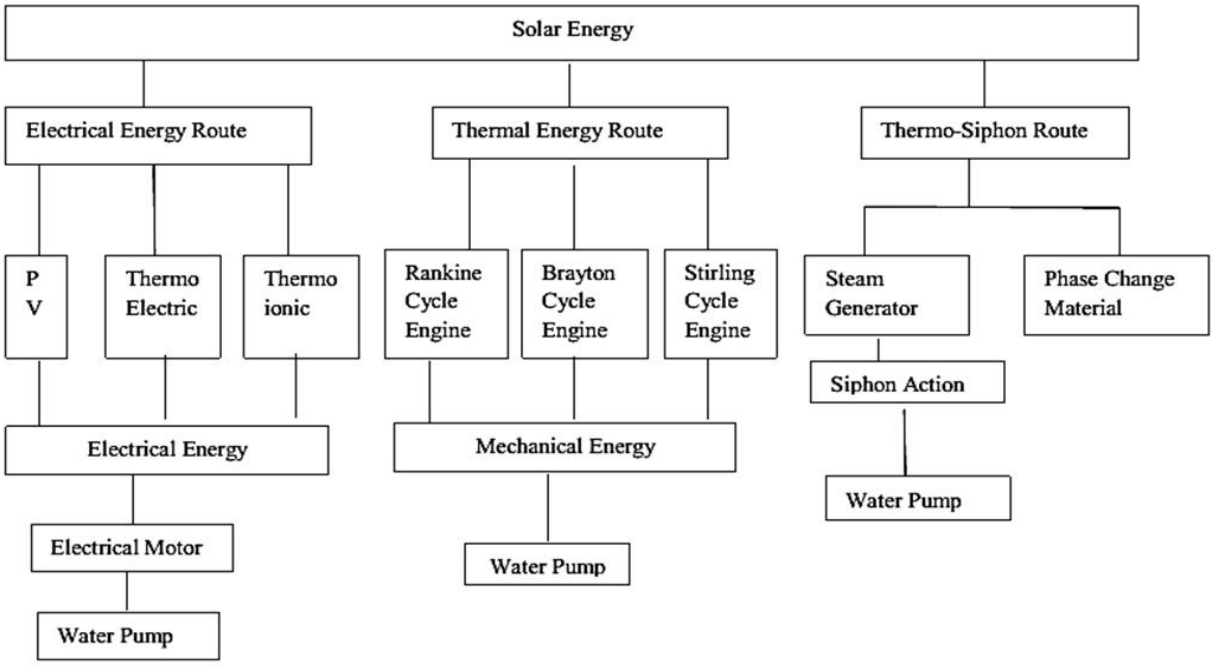

Figure 2.1: Classification of Solar Water Pump [12]

2.1.1 Solar Thermal Irrigation System

In a solar thermal irrigation system, the working fluid is first produced at high temperature and pressure using different solar collectors. Then thermal energy produced is directly converted to mechanical energy through Rankine, Brayton, or Stirling cycle. The mechanical energy allows the pump to lift the ground or surface water to the farmlands.

The thermal Stirling pump is one of the most effective solar thermal irrigation systems due to its simplicity, compact size, and capability to manufacture using locally available resources. The Stirling cycle-based technology systems are investigated mostly to reduce the cost. Thus, the research undertaken investigated medium to low power solar collection/temperatures with a difference of 60–95 °C. Higher temperatures should be able to provide better outputs [13].

Wazed M.S et al. investigate the Stirling engine for an irrigation system that provides low head losses and flow. However, some provision is shown to add more heat into the system or inject mechanical assistance to further elevate the technology to provide a more significant output. They state the Stirling engine's advantages, as any heat source may be used to provide thermal energy and hence suitable for use in a hybrid system. The Stirling cycle holds the highest potential for small scale remote farms usage if the correct infrastructure is available for solar power concentration [3].

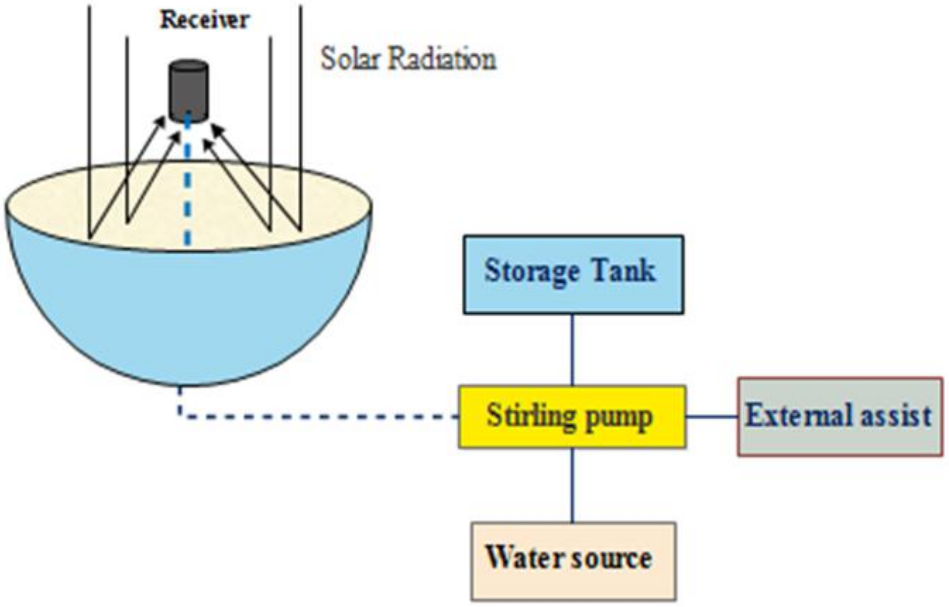

Figure 2.2: Solar Thermal Stirling Pump [3]

2.2 Thermoelectric Generator (TEG)

The global energy crisis has motivated researchers to explore alternative means of generating power. One approach to providing electrical energy is the direct conversion of heat to electricity using thermoelectric generators (TEG) [14].

A thermoelectric generator (TEG) is a device that converts thermal energy into electrical energy directly through a temperature gradient based on the see-beck effect. In the thermoelectric power cycle, electrons (charge carriers) serve as the working fluid based on thermodynamics' fundamental laws. Thermoelectric power generation is one of the current interests in clean energy research because of direct solar power generation. Thermoelectric power has enormous potential to become an alternative power source for electrical power supply, as they could provide a cogeneration system anywhere thermal gradients exist. The most efficient way to improve thermoelectric power generation systems' performance is by integrating with other energy sources [15]. The thermoelectric module can be coupled with flat plate solar collectors, evacuated tube solar collectors, and parabolic dishes for the cogeneration system.

2.2.1 Working Principle of Thermoelectric Generator (TEG)

TEG works according to the principle of see-beck effects. The effects state that electric potential can be generated between two junctions at different temperatures if the circuit is formed with two dissimilar metals.

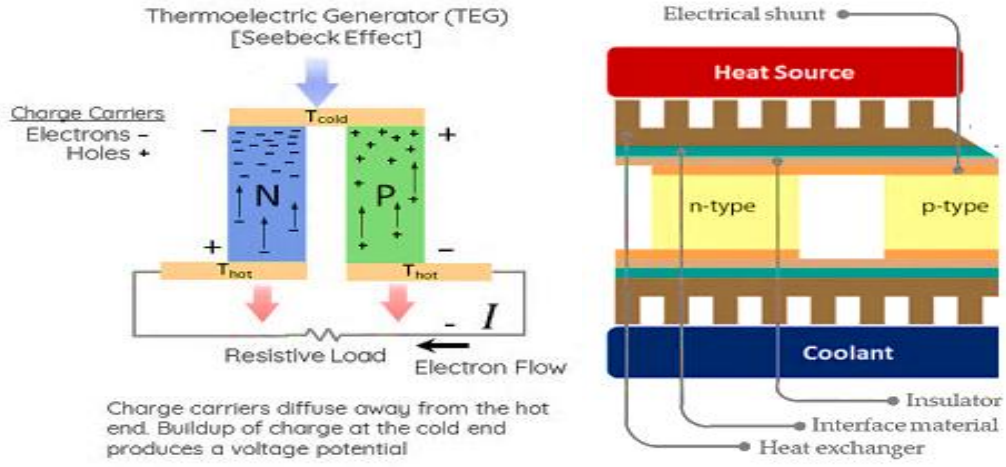

Figure 2.3: Working Principle and Components of TEG [17]

The thermal energy is directly converted to electrical energy (An open circuit electric voltage is generated) when the temperature gradient occurs between the junction. A TEG consists of many thermocouples formed by n-type and p-type semiconductor materials sandwiched between ceramic plates connected electrically in series and thermally in parallel [16].

The performance of a thermoelectric generator is expressed in terms of the figure of merit. The figure of merit depends on different material parameters like the See-beck coefficient, thermal conductivity, and electrical resistance. A value of the figure of merit increases with high electrical resistance, low thermal conductivity, and high See-beck coefficient [16,17]**.** It is given as;

$$ZT = \frac{\alpha^2}{\rho * k} * T \tag{1}$$

Where; α,ρ, k, and T are the See-beck coefficient, electrical resistance, thermal conductance, and absolute temperature, respectively.

The electrical efficiency of the thermoelectric generator is expressed as;

$$\eta_{TEG} = \left(\frac{T_h - T_c}{T_h}\right) * \left(\frac{\sqrt{1+ZT}-1}{\sqrt{1+ZT}+\frac{T_c}{T_h}}\right) \tag{2}$$

Where; T_h and T_c are the temperature at the hot and cold side of the thermoelectric generator, respectively.

2.2.2 Cooling mechanism of TEG

As TEG feat the temperature difference between their two sides, maintaining a higher temperature difference will increase the power yield. The hot side of the TEG is in thermal contact with a heat source such as a waste heat pipe or concentrated solar radiation. In contrast, the cold side temperature is kept low by cooling it to the maximum possible extent. To maintain the higher temperature difference, the heat that is diffused from the hot side must be dissipated from the cold side. Thus, the output power will be increased.

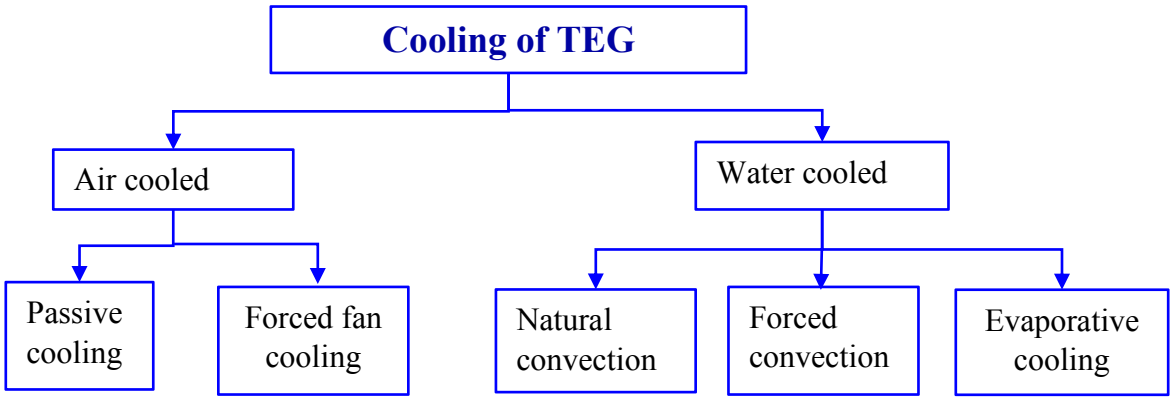

Figure 2.4: Schematic of a cooling system for TEG [16]

2.3 Review of previous studies related to the study topic

Feiyang, S. et al. [18] proposes to design an experimental investigation of solar thermoelectric (STEG) cogeneration system. The experimental analysis of the solar heat pipe collector, coupled with the TEG module, was done. The system can generate electricity and hot water simultaneously in electrical power and hot water models. The power generation section and the heat transfer section of the system are the double-layer water tank with TEG modules in the middle heat insulation layer. The collector's heat pipe coupled into the upper layer of the double-layer heat exchange box and the thermoelectric sheet's heat end relates to the heat conduction copper block. The results show that the STEG system, which consisted of 10 heat pipes in 10 evacuated tubes with 10 TEG modules, can generate 0.2 KW and 100 L of hot water at 41 ^{o}C in a day at 1000 W/ m^2. The collector efficiency and electrical efficiency is 42.2 % and 2.1%, respectively.

Wazed, S.M et al. [3] investigate the solar-powered irrigation technologies, both PV and solar thermal, that can be utilized by independent farmers in small-scale remote rural farms of sub-Saharan Africa. The research's main objective is to identify an affordable solar-powered irrigation system that will effectively use local resources for drip irrigation. They found that PV solar (C_dT_e PV module) running a permanent magnet DC motor that drives the pump is most effective among different PV technologies. The system works only during extended sun hours and stores water in a storage tank instead of utilizing a battery.

The main drawback of the system is the expensive initial investment. Thus, it is not affordable for independent farmers with low incomes. On the other hand, the most effective solar thermal irrigation system is the Stirling pump utilized by a solar concentrator. Its simplicity, locally produced, environmentally friendly, and low cost is preferable among farmers with low income. Finally, the authors concluded that solar thermal is suitable for the irrigation systems in the remote areas of sub-Sahara Africa due to its simplicity, locally produced, and initial investment costs.

Nenad, M. and Wang, E.N. [15] present the modelling and optimization of a new hybrid solar thermoelectric system that uses a thermosyphon to transfer heat to a bottoming cycle for various application passively. A parabolic trough mirror concentrates solar energy into a selective coated thermoelectric to produce electrical power. Meanwhile, a thermosyphon adjacent to the thermoelectric backside maintains the cold junction's temperature and carries the remaining thermal energy to a bottoming cycle. Three different TEG modules and working fluid are considered in the study.

An energy-based model of the HSTE system with a thermal resistance network was developed to determine overall performance. The HSTE system efficiency was investigated for a temperature of 300K- 1200K, the solar concentration of 1-100, and different thermosyphon and thermoelectric material with geometry resembling an evacuated tube solar collector. The optimization of the HSTE show an outstanding efficiency as high as 52.6 % at a solar concentration of 100 and the bottoming cycle temperature of 776 K.

Lertsatitthankorn, C. et al. [20] study the concept of generating electricity from the sun using the hybrid solar -TEG. The system is composed of a parabolic dish with an aperture area of 1.5 m and a 10*10 cm^2 receiver plate. One bismuth telluride-based TEG module is installed on the receiver plate to convert the concentrated solar thermal energy directly into electric energy.

A rectangular fin heat sink coupled with a fan was used to dissipate heat from the TEG module's cold side, and a tracking system was used to track the sun continuously. Under maximum heat flux of 1400 kW/m^2, the TEG module was able to produce 1.32W at 0.42 m^3/min of the airflow (pushing air) and 2.89% of conversion efficiency. The authors found that the heat transfer and conversion efficiency of pushing air is more than pulling air by 6% and 12.8%, respectively.

Muthu, G. et al. [21] conduct a solar parabolic dish collector driven the TEG experimental model with a diameter of 3.56 m and a focal length of 1.11m. The receiver is embedded by the bismuth telluride TEG module with an absorber plate, and it is enclosed in an acrylic cover. The author presents the experiment work at a constant flow rate of heat transfer fluid of water and an empirical relationship to find system efficiency with and without acrylic cover. The result shows a maximum receiver temperature of 383 K, maximum power of 3.7 W, and overall system efficiency of 1.68% at beam solar radiation of 1050 W/ m^2. Considering acrylic cover, receiver temperature is improved by 1.56%, output power by 2.1%, and efficiency by 2.51%.

Çolak, L. & Kıllış, B. [22] developed the concept of sandwiched PV cell with thermoelectric generator (TEG) modules for generation of more solar electric power for the irrigation systems. The PHVT module comprised a sandwiched structure of a PV cell with a multiple of TEG units bonded at the back and sandwiched, overcooling a layer acting as the cumulative heat sink. The heat rejected from PV solar cells due to overheating is absorbed by the TEG module to generate additional power. The temperature at the cold side of TEG is cooled by cold well water used for irrigation. PV and TEG's two-hybrid arrangement options were analyzed in the study, namely vertical sandwiched and side-by-side arrangement. The result shows that a vertical sandwiched hybrid system generated 31 % higher power than stand-alone PV solar. The side-by-side configuration boosts the output power by 24% than vertical sandwiches if the condition is kept the same.

Bamroongkhan, P. et al. [23] conduct the experimental performance study of a hybrid solar parabolic dish photo-voltaic-thermoelectric generator. The performance analysis of focal length and the system is taken under realistic outdoor circumstances. The forced air-cooling system is used to remove the heat from the cold side of TEG and PV. The results show that the thermoelectric generator and PV conversion performance is 2.96% and 16.69%, respectively. The output power obtained from TEG and PV is 2.94 W and 1.93 W, respectively, at a temperature difference of 113.6 ^{o} C. The optimum focal point obtained from the analysis is 57 cm, and at this point, maximum hot side temperature and power are recorded.

2.4 Research gap

A solar dish concentrator can be used with various electrical power generation systems like Stirling engines, photo-voltaic cells, steam generators, and thermoelectric generators. There are many studies that have been carried out using solar dish concentrator integrated with TEG,and solar dish Stirling for different application [13,14,20-23,34,36]. But, literature review confirmed no specific work reported on the solar dish concentrator integrated with the thermoelectric generator and a thermal Stirling pump for water pumping.

In order to harness a maximum energy a dish concentrator must flow the path of the sun. Most of the time PV solar is used as energy source by servomotor of a dish concentrator, which increases the overall cost of the system. The proposed system intend to use an electric power converted by TEG to reduce the cost and to increase the reliability of the system.

Integration of Photo-Heat-Voltaic-Thermal system for irrigation system also studied, but the effectiveness and feasibility for small scale irrigation system are not as expected. The performance of the system is also decline due to a various losses encounter by the system. So, a detailed transient performance analysis is required to identify the system's losses by varying operating parameters. Even though currently available irrigation technology plays a vital role in poverty reduction, the depletion of fossil fuel, initial capital cost, and environmental impact discourage the utilization of the technology. So, the proposed system can address hybrid technology for small scale irrigation system to benefit smallholder farmers toward enhancing food security and poverty reduction.

CHAPTER THREE

3. METHODOLOGY

3.1 Location of Study Area

The study is carried out in Fiche, north of Ethiopia, located 114 km from the capital city Addis Ababa. It is the administrative Centre of the Semien Shewa Zone (Selale) of the Oromia Region. Fiche is located at a coordinate latitude of 9°48′N and longitude 38°44′E and an elevation between 2,738 and 2,782 meters above sea level and with an estimated total population of 37,861 based on the central statistical agency of Ethiopia (CSA). It lies in the climatic zone locally known as Dega and Woynā Degā, which is considered as ideal for agriculture and human settlement [24].

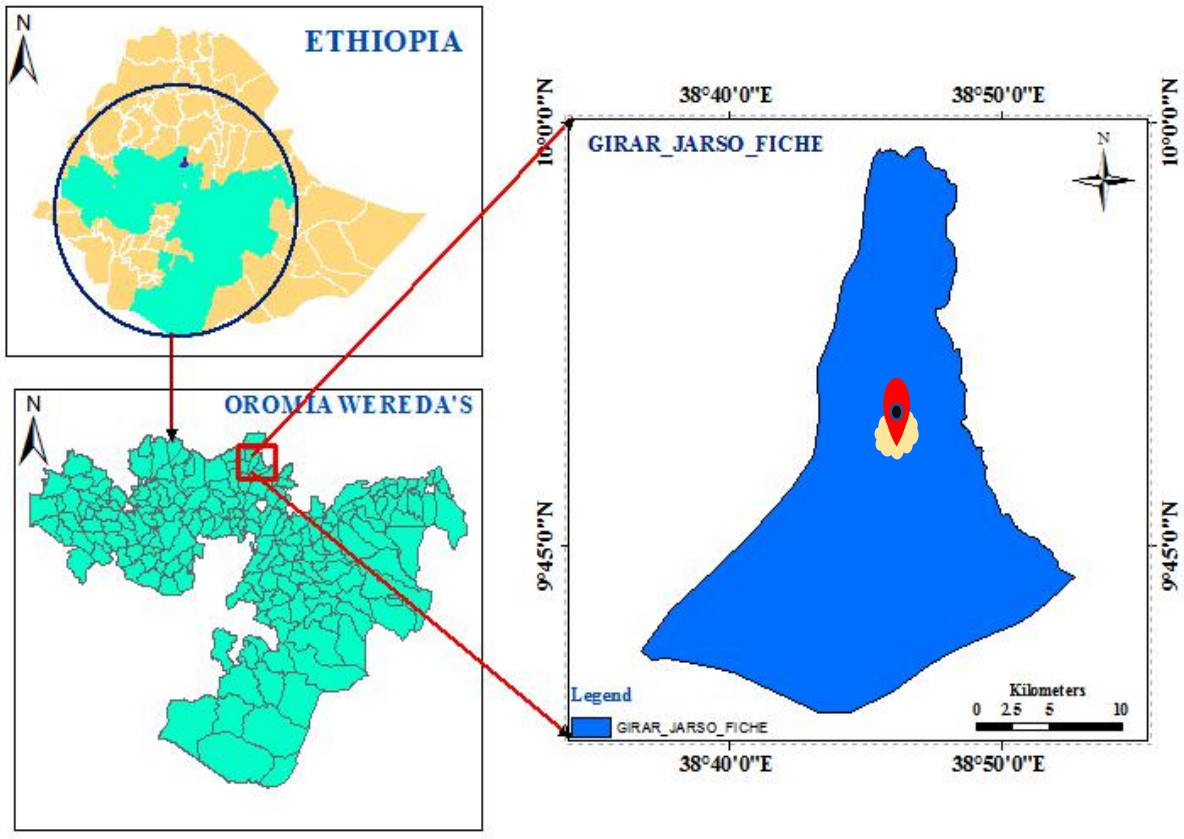

Figure 3.1: Map of the study area

3.2 Data Collection and Analysis Methods

To achieve the desired objective, primary and secondary data are collected from literature and other relevant resources. The solar radiation and other weather data are predicted based on the site's latitude and longitude using open-access software. The sunshine hour data obtained from Newloc-Clim software and the estimation of the solar radiation data is performed according to Angstrom-Prescott Colleration. The estimated data were compared with data generated from Meteonorm, SWERA, Power data access (NASA-based), and RETScreen.

Data analysis and process were carried out through Matlab, ESS, and Origin Pro software. For ray tracing and flux distribution analysis at the receiver of the concentrator, SolTrace software was used. The temperature distribution at the concentrator's focal plane and performance analysis of a thermoelectric generator was carried out through COMSOL Multiphysics software.

3.3 Description of the Proposed Model

The parabolic dish solar concentrator receives the electromagnetic radiation of solar energy falling from the sun. The receiver kept at the concentrator's focal point absorbs the solar beam radiation received by a parabolic dish. The solar energy at the receiver's surface is directly transferred to the working fluid inside of absorber to produce the steam at the desired temperature. Due to the density difference (thermosiphon principle), the steam rises inside the receiver, and the fluid temperature will also increase.

The useful heat of fluid is converted to electrical power through the thermoelectric generator coupled at the receiver's top. The energy conversion is taking place due to temperature differences between the hot and cold side TEG modules. The hot side of the TEG module is in direct contact with the working fluid inside the receiver, and the cold side of the module integrates with a heat sink. The heat sink dissipates the heat from the module's cold side through natural convection to maintain a high-temperature gradient across the module.

In another case, the outlet steam from the absorber is used as a heat source for the thermal pump (Stirling pump). The heat is transferred from the steam to the compressed air inside the closed chamber through convection and conduction heat transfer mode.

The working gas volume expanded in expansion space to produce work as heat supplied from heat source. The conversion of the thermal energy to mechanical energy causes the piston's movement to rotate the centrifugal pump's impeller, and the mechanical energy of the engine is converted to hydraulic power to pump the water at a given head through a centrifugal pump.

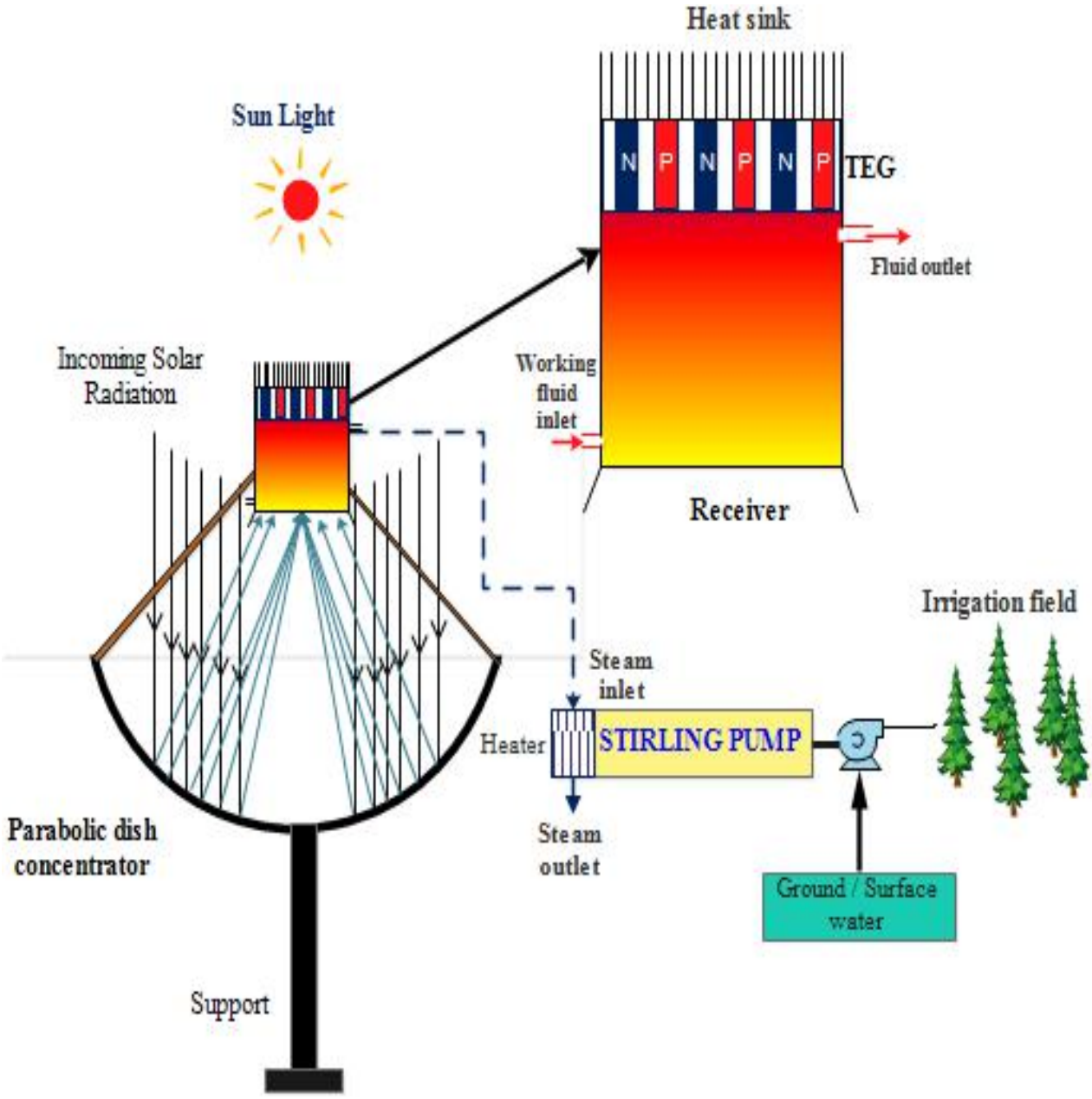

Figure 3.2: Working Principle of the proposed model (Solar dish concentrator integrated with Stirling and TEG)

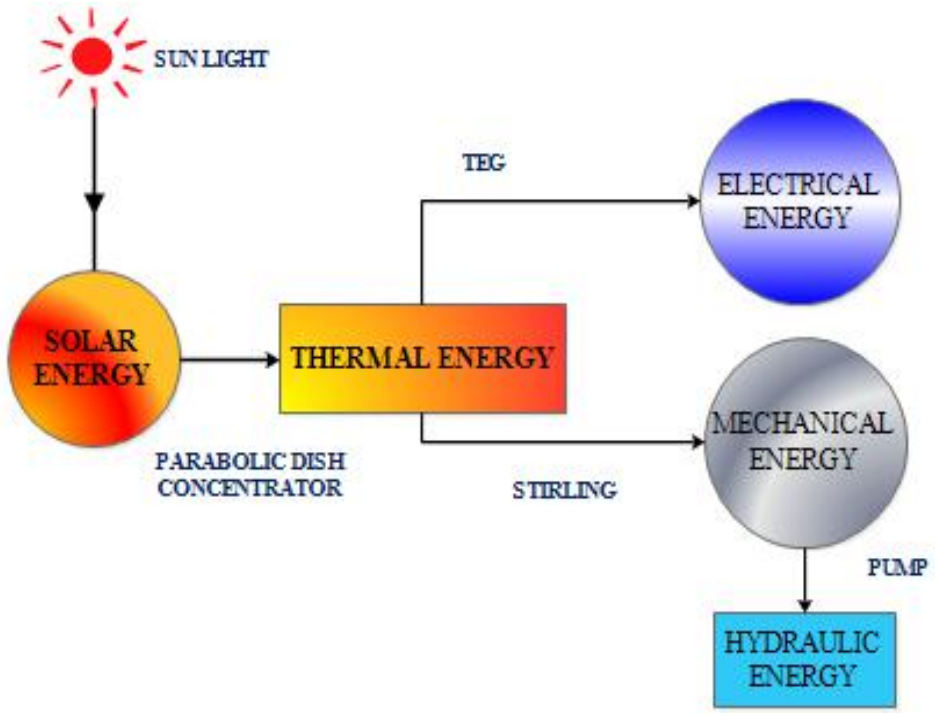

Figure 3.3: Schematic diagram for the conversion of energy

Figure (3.3) show the conversion of energy from one form to another in a proposed system. Primary solar energy is converted to thermal energy through a dish solar concentrator. The concentrator dish reflects the incoming solar radiation to the absorber kept at the focal point. So, the supplied heat is directly converted to useful heat by a working fluid inside the receiver. The thermoelectric generator is coupled with the receiver concentrator to recover the fluid's thermal heat, as shown in figure (3.2). TEG converts thermal heat to electric power as a temperature gradient maintained between the hot side and cold side of the module. Meanwhile, the outlet fluid from the absorber is used in the Stirling engine as a heat source to produce mechanical work, which allows the pump to deliver the water for the irrigation system.

3.4 Solar Radiation Components

3.4.1 Hour Angle

Hour angle (ω) shows the angular distance between the observer's meridian and the meridian that contains the sun. It is an angle at which the earth rotates around its polar axis. i.e., +15^o per hour during the morning and -15^o in the afternoon time. It can be estimated according to Equation (3.1);

$$\omega = 15^o\,(ST - 12) \tag{3.1}$$

Where; ST is the local solar time

$$\text{ST= Standard Time} + 4(L_{st}\text{-}L_{loc}) + \text{EoT}$$

Where; L_{st} is the standard meridian for the local time zone (degrees)

L_{loc} is the longitude of the location (degrees)

EoT is the equation of time (min)

$$\text{EoT} = 229.2(0.000075 + 0.001868\cos(X) - 0.032077\sin(X) - 0.014615\cos(2X) - 0.04089\sin(2X))$$

And where, $X = (n-1) * \frac{360}{365}$

3.4.2 Declination Angle

The angular distance from north or south of the sun to the earth equator is called the declination angle. It ranges between positive 23.45 degrees to the north and negative 23.45 degrees to the south direction. Solar declination (δ) is the angle between the earth-sun line and the line's projection through the equatorial plane.

The solar declination angle can be calculated using the approximated Cooper's Equation [25]

$$\delta = 23.45 \sin\left[360\frac{(284+n)}{365}\right] \tag{3.2}$$

Where 'n' is the number of days in a year, i.e., starting from 1st January to 31st December as given in table (3.2).

Table 3.2: The average day of each month as recommended by Klein [25]

Month	Date of the month	Day of the year	Declination angle
January	17th	17	-20.92
February	16th	47	-12.95
March	16th	75	-2.42
April	15th	105	9.41
May	15th	135	18.79
June	11th	162	23.09
July	17th	198	21.18
August	16th	228	13.45
September	15th	158	2.22
October	15th	288	-9.60
November	14th	318	-18.91
December	10th	344	-23.05

The graphical representation of the solar declination angle throughout a year is shown below in figure (3.4).

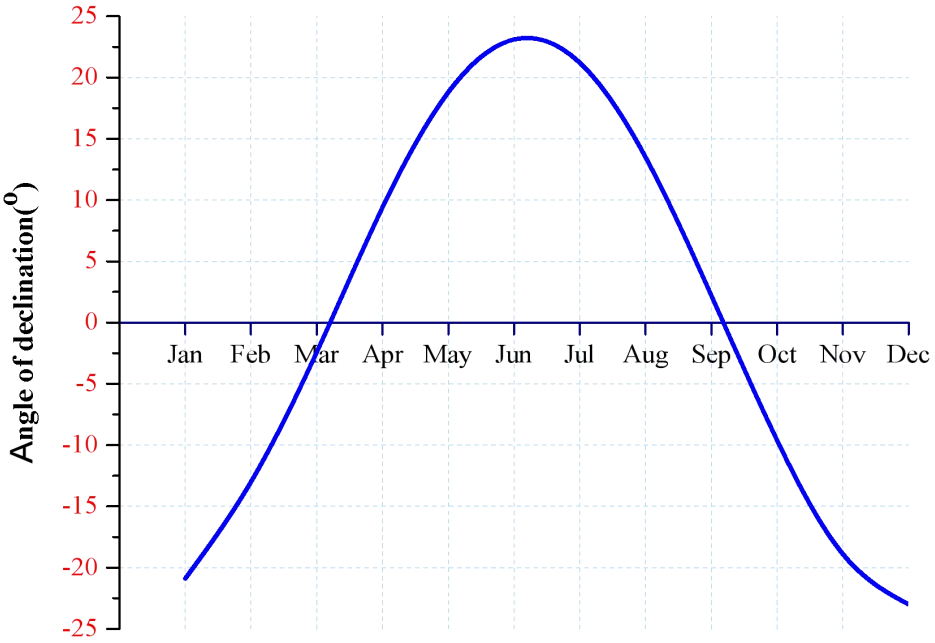

Figure 3.4: Variation of Solar Declination Angle through a Year

3.4.3 Solar Azimuth Angle

According to Kalogirou, the solar azimuth angle is defined as the angle measured between the sun's ray and south direction for a northern hemisphere or north direction for southern hemisphere from the horizontal surface [30]. It is obtained from Equation (3.3).

$$\gamma_s = \sin^{-1}\left(\frac{\cos(\delta) * \sin(\omega)}{\cos(\alpha)}\right) \tag{3.3}$$

Where; δ is a declination angle given in Equation (3.2), ω *is a* hour angle in Equation (3.1), and α is altitude angle.

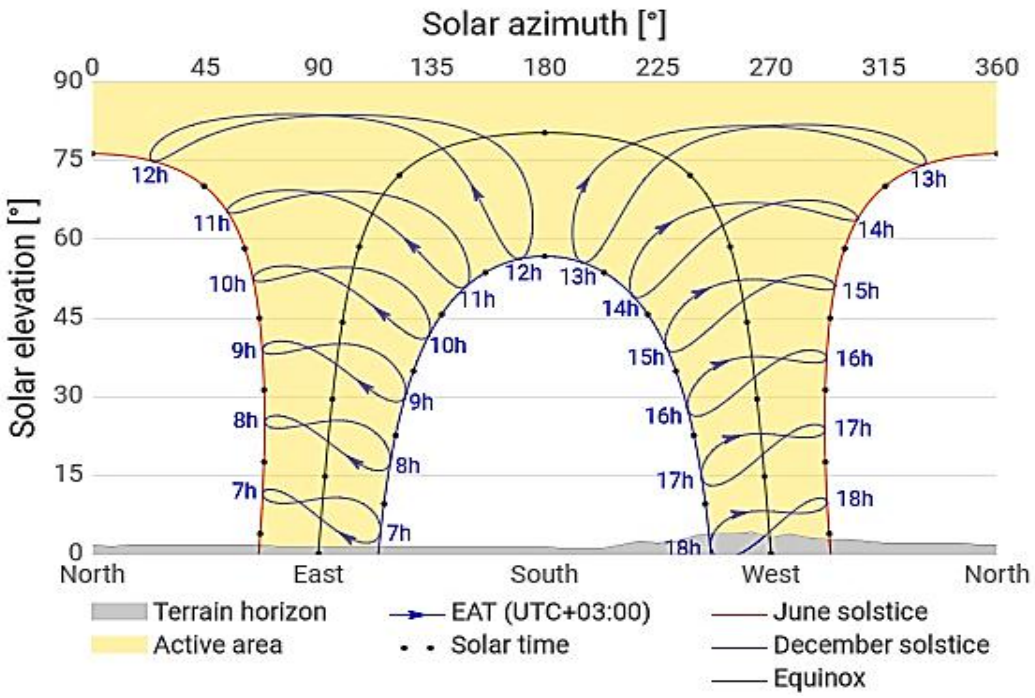

Figure 3.5: Solar azimuthal angle [27]

3.4.4 Incidence Angle

The angle of the incident is the angle between beam solar radiation on the surface and normal to that surface. The incidence angle has a significant effect on the beam solar radiation absorbed by the solar concentrator. To increase the concentrator's energy, the angle of the incident should be minimal. A possible tracking system is required to adjust the concentrator with the sun's motion.

3.5 Estimation of Hourly, Daily, and Monthly Solar Radiation on Horizontal Surfaces

3.5.1 Estimation of Monthly Average Daily Global Radiation on Horizontal Surface

Angstrom-Prescott proposed the estimation of global solar radiation using a linear regression model. The correlation was given as [26];

$$\frac{\overline{H}}{\overline{H_0}} = a + b\frac{\overline{n}_s}{\overline{N_s}} \tag{3.4}$$

Where; $\overline{H}$ is a monthly average daily global radiation on the horizontal surface.

$\overline{H_0}$; Monthly average daily extraterrestrial radiation on a horizontal surface

$\overline{n}_s$; Monthly average daily hour of sunshine duration at a clear sky

$\overline{N_s}$; Monthly average of the maximum possible daily hour of bright sunshine

$\frac{\overline{H}}{\overline{H_0}}$; Clearness index

$\frac{\overline{n}_s}{\overline{N_s}}$; Relative sunshine duration

a, b: Empirical constants obtained using regression correlations

The regression parameters "a" and "b" is given as;

$a = -0.110 + 0.235cos\phi + 0.323\left(\frac{\overline{n}_s}{\overline{N_s}}\right)$, and $b = 1.449 - 0.533cos\phi - 0.694\left(\frac{\overline{n}_s}{\overline{N_s}}\right)$

The monthly average radiation outside of the atmosphere ($\overline{H_0}$) can be obtained using the Klein relationship [26, 28]. It is solar radiation received at the top of the Earth's atmosphere on a horizontal surface.

$$\overline{H_0} = \left[\frac{24*3600}{\pi} I_{sc}\right]\left[\left(1 + 0.033cos\left(\frac{360n}{365}\right)\right)\right]\left[cos\phi\, cos\delta\, sin\omega_s + \frac{\pi}{180}\omega_s sin\phi\, sin\delta\right] \tag{3.5}$$

Where; $I_{SC} = 1367\ W/m^2$ (Solar constant)

The geometric mean sunset hour angle for the month on a horizontal surface can be calculated (except in the absence of sunrise and sunset, during the polar day and night) in degrees from [25];

$$\omega_s = arccos(-tan\phi tan\delta)$$

Where; (ϕ) is the local latitude and (δ) is the solar declination angle

The length of sunshine duration ($\overline{N_s}$) are computed by Cooper's formula [25], and the plotting of the Equation is shown in figure (3.6).

$$\overline{N_s} = \left(\frac{2}{15}\right)\omega_s \tag{3.6}$$

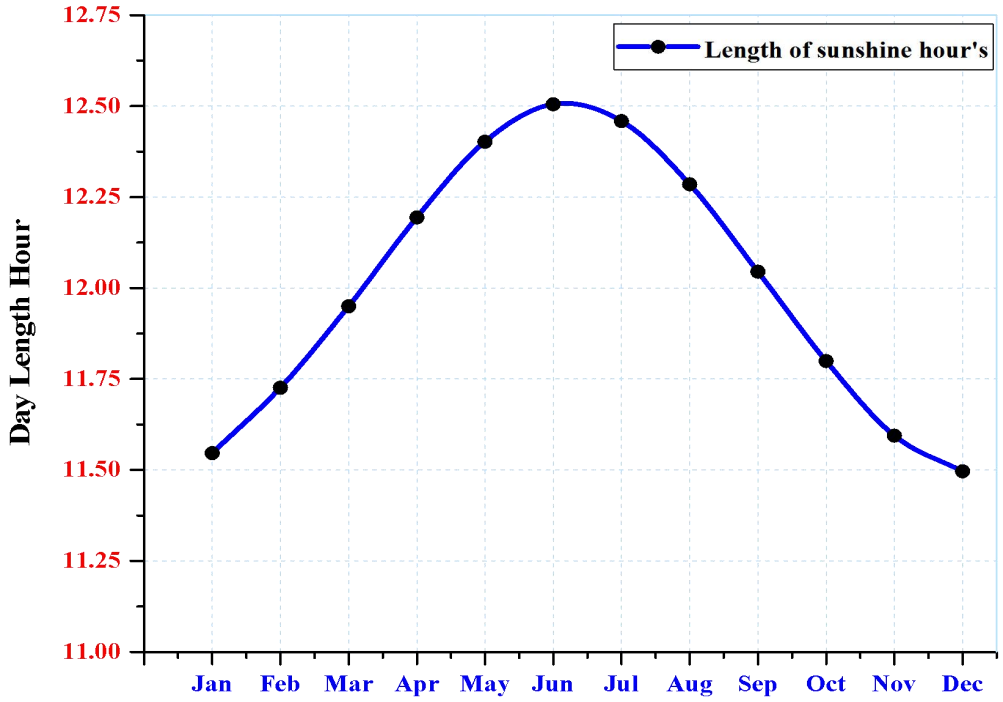

Figure 3.6: Monthly Average Value for maximum Length of bright Sunshine Duration in a day

3.5.2 Estimation of Monthly Average Daily Diffuse Radiation on a Horizontal Surface

The estimation of monthly average daily diffuse radiation on a horizontal surface is based on monthly average daily global radiation on a horizontal surface and the number of bright sunshine hours.

$$\frac{\overline{H_d}}{\overline{H}} = 0.931 - 0.814\left(\frac{\overline{n}_s}{\overline{N_s}}\right) \tag{3.7}$$

3.5.3 Estimation of Monthly Average Hourly Global Radiation on a Horizontal Surface

The monthly average hourly global solar radiation on a horizontal surface can be calculated from the knowledge of the monthly average daily global radiation on a horizontal surface.

$$\frac{\bar{I}}{\bar{H}} = \frac{\pi}{24}(a + b\cos\bar{\omega})\left[\frac{\cos\bar{\omega} - \cos\bar{\omega}_s}{\sin\bar{\omega}_s - \frac{\pi}{180}\bar{\omega}_s \cos\bar{\omega}_s}\right] \quad (3.8)$$

Where;

$$a = 0.409 + 0.5016\sin(\bar{\omega}_s - 60)$$

$$b = 0.6609 - 0.4767\sin(\bar{\omega}_s - 60)$$

3.5.4 Estimation of Monthly Average Hourly Diffuse Radiation on a Horizontal Surface

The monthly average hourly diffuse radiation on a horizontal surface can be calculated using Equation (3.9). It depends on the value of monthly average daily diffuse radiation on a horizontal surface.

$$\frac{\bar{I}_d}{\bar{H}_d} = \frac{\pi}{24}\left[\frac{\cos\bar{\omega} - \cos\bar{\omega}_s}{\sin\bar{\omega}_s - \frac{\pi}{180}\bar{\omega}_s \cos\bar{\omega}_s}\right] \quad (3.9)$$

3.5.5 Estimation of Monthly Average daily Maximum, Minimum and Average Temperature on Horizontal Surface

The monthly average daily maximum, minimum, and average temperature on the horizontal surface can be calculated using the monthly average hourly variation of temperature. The estimation was performed depending on the Newloc-Clim estimator using the site-local latitude and longitude. The result shows a minimum and maximum temperature of 7.8 and 25.02 ^{o} C recorded in December and April, as illustrated below in figure (3.7).

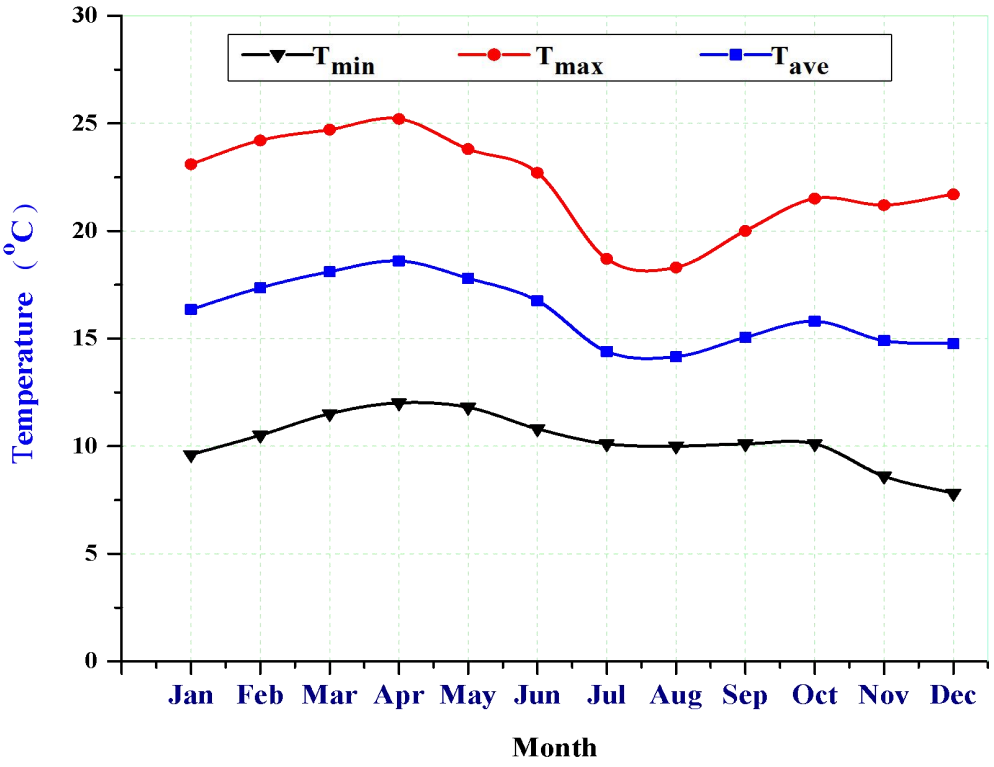

Figure 3.7: Monthly Ambient Temperature Variation

3.5.6 Estimation of Monthly Average Daily Precipitation and Evapotranspiration

Based on the local climate estimator software, the pumping water requirement period is limited with a range of time. The estimated actual precipitation and potential evapotranspiration is an essential factor that determines the amount of water requirement for crops under current and future conditions. The irrigation system is significant only if the potential evapotranspiration exceeds the actual precipitation in a site [29]. The energy can be required to pump the water to the irrigation field under this condition. Mathematically;

$$P_a - P_{et} \geq 0 \tag{3.10}$$

Where; P_a is actual precipitation of the area and P_{et} is potential evapotranspiration

When the value of potential evapotranspiration exceeds actual precipitation, water pumping is required for the irrigation systems, unless if it is a wet season and no need for water pumping due to excess rainfall. So, an irrigation system is only applicable when potential evapotranspiration (crop water requirement) exceeds the actual precipitation (available rainfall) for a given season (i.e., from October to the end of May), as shown in figure (3.8).

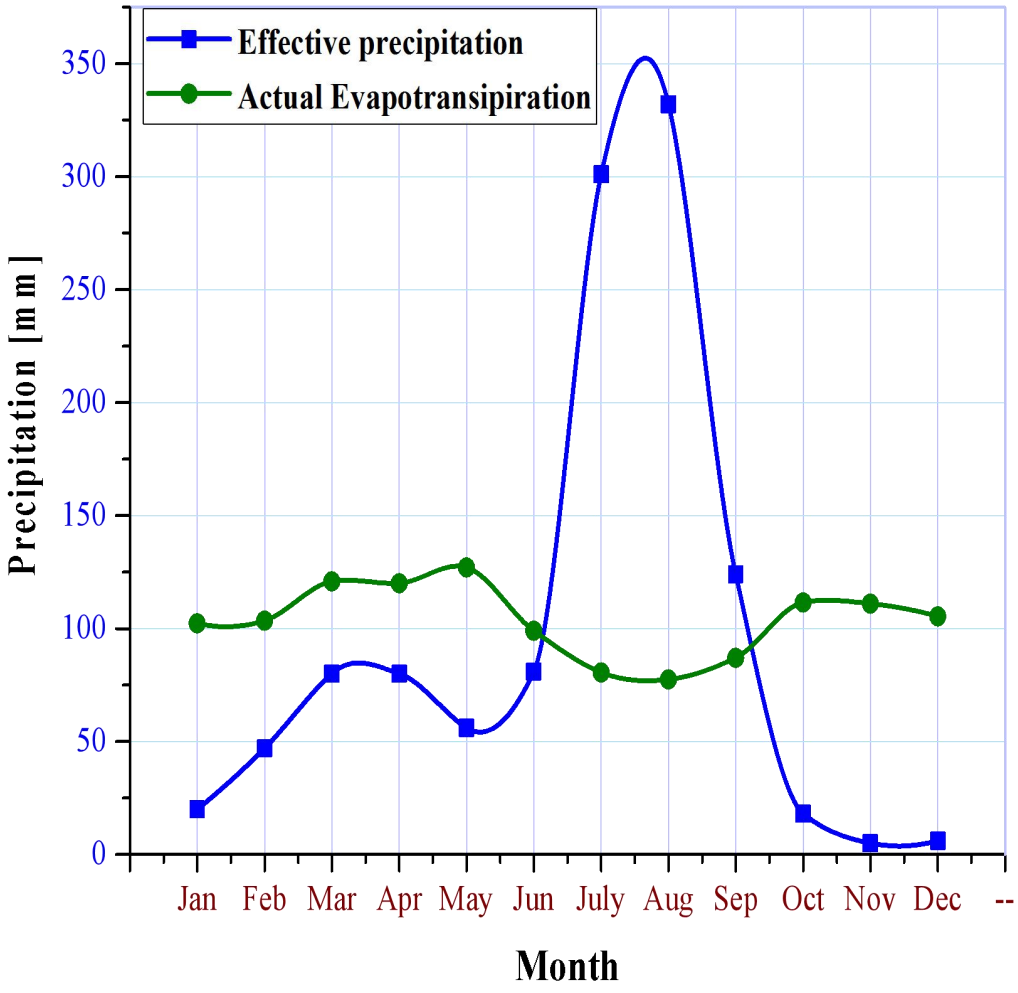

Figure 3.8: The local growing season of the selected site relative to actual precipitation and evapotranspiration

CHAPTER FOUR

4. DESIGN AND ANALYSIS

4.1 Design of Solar Dish Concentrator

4.1.1 Concentrated Solar Power (CSP)

Concentrated solar power (CSP) is a device that transfers solar energy into the internal energy of the transport medium. The incoming solar radiation was falling on the concentrator's aperture area covered with a reflecting material, and the receiver kept at focal plane absorb the energy reflected from the concentrator. The solar heat flux reaches the absorber's surface was transferred to a working fluid kept inside the concentrator's receiver to produce the desired thermal energy. In concentrating solar power, all incoming solar radiation focuses on small receivers to increase the radiation flux and produce high-temperature steam. CSP also has a remarkable advantage: achieving high temperatures, high thermal and thermodynamics efficiency, requiring less material, and having a simple structure than a non-concentrator collector**.**

The concentrated solar collector can be classified into imaging and non-imaging, depending on the formation of the sun's image at the absorber of the concentrator [25, 30]. Imaging concentrators produce an optical image of the sun on the receiver. Non-imaging concentrators do not create a sun image. Instead, they disperse the sun's light over the receiver's whole area and have low concentration ratio than the imaging type. Solar dish concentrator, parabolic trough collector, linear Fresnel, and central receiver are falling under imaging types.

A parabolic dish is a point-focused collector that tracks the sun in a two-axis to concentrate solar energy into a receiver located at the dish's focal point [31]. The incoming solar radiation focused on the single focal point, i.e., all sun rays parallel to the parabola axis directed towards the receiver. The tracking was allowing the mirrors to maximize the amount of DNI that is reflected onto the receiver and achieve a high concentration ratio and high working temperatures for the heat transfer fluid.

The solar dish concentrator is selected for this study due to the following advantages listed according to Kalogirou [30]:

- The dish concentrator is the most efficient of all types of solar reflectors, and it faces the sun.
- They are modular collectors and receivers because each system can function by itself or as part of an array of dishes in a more extensive system.
- Dish concentrator has high concentration ratio that make them more efficient for absorbing thermal energy.

Table 4.1: Classification of Concentrated Solar Power (CSP) [30]

Collector type	**Focus**	**Tracking system**	**Concentration ratio**	**Indicative temperature (º C)**
Linear Fresnel reflector (LFR)	Line (Tubular)	Single-axis	5-15	60-250
Parabolic trough collector (PTC)	Line	Single-axis	10-40	60-300
Cylindrical trough collector (CTC)	Line	Single-axis	15-45	60-300
Parabolic dish reflector (PDR)	Point	Double axis	100-1000	100-1500
Heliostat field reflector (HFC)	Point	Double axis	100-1500	150-2000

4.1.2 Design calculation of parabolic dish concentrator

The first step that should be taken while designing a solar dish concentrator is by considering a locus of points that lies at an equal distance from a line (directrix) and a focal point.

Each coordinate point of the parabola generated using parabola calculate software [32], and the coordinate values are performed for 18 points, as shown in table (4.2). The mathematical Equation of the solar parabolic dish concentrator in a Cartesian coordinate system is defined as;

$$x^2 + y^2 = 4fz \tag{4.1}$$

Where; ***x, y*** coordinates in aperture plane, z is the distance from the vertex measured along the line parallel with the parboiled axis of symmetry, and ***f*** is the focal length of the parabola.

The Equation of a parabola that represents the coordinate of this parabolic curve is given as

$$y = ax^2 + bx + c \tag{4.2}$$

Where; a,b and c are constant with $a = 2.778 * 10^{-4}$, $b = 0$ and $c = 3.638 * 10^{-16}$, and by substituting the values into the Equation (4.2), the Equation of the parabola can be as follows;

$$y = 2.778 * 10^{-4}x^2 + 3.638 * 10^{-16}$$

Table 4.2: x-y coordinates of designed parabolic dish concentrator using Parabola Calculator 2.0 software [32]

X1(mm)	-1200	-1050	-900	-750	-600	-450	-300	150	0
Y1(mm)	400	306.25	225	156.25	100	56.25	25	6.25	0
X2(mm)	0	150	300	450	600	750	900	1050	1200
Y2(mm)	0	6.25	25	56.25	100	156.25	225	306.25	400

The aperture area of the dish concentrator is the total surface of the concentrator, where the incoming solar radiation incident [33]. The solar dish concentrator's size will affect the amount of energy delivered to the receiver of the concentrator [34] and the thermoelectric generator integrated within it. The aperture area of the concentrator can be obtained using Equation (4.3)

$$A_a = \frac{\pi D_c^2}{4} \tag{4.3}$$

Where; Dc is the diameter of the concentrator, as shown in figure (4.1).

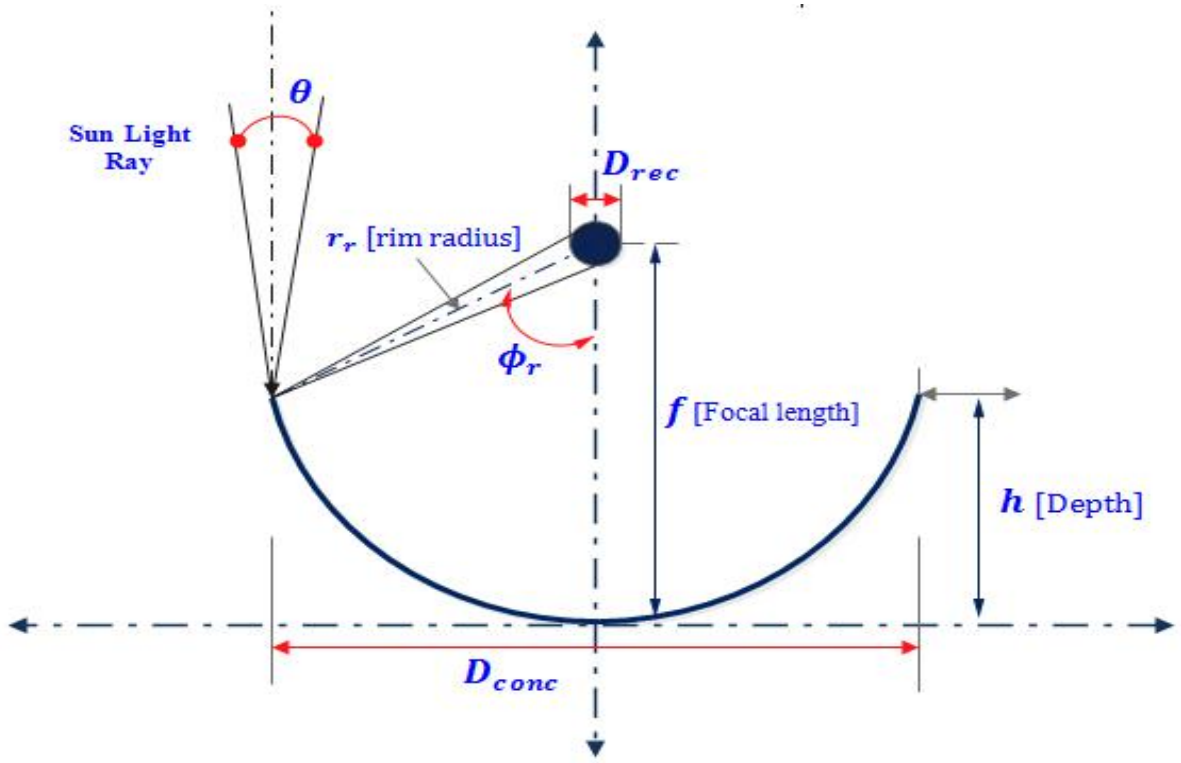

Figure 4.1: Schematic Diagram of Parabolic Dish Concentrator Geometry with Concentrator Diameter, Receiver Diameter, Focal Length, Rim Angle, Acceptance Angle, and Depth of the parabola

The solar dish concentrator is made up of the reflecting material that reflects the radiation falling in the concentrator to the focal point. The focal length is the distance between the vertexes of the parabola to the focus [33]. It is related to the size of the concentrator and the depth of the parabola. Focal length can be obtained using the following Equation.

$$f = \frac{D_c^2}{16 * h} \tag{4.4}$$

According to William B. Stine [38], the rim angle is defined as the angle measured at the focus from the axis to the solar parabolic truncated rim. Fraser [39] describes the rim angle as an indicator of the parabolic concentrator's curvature. The rim angle affects the incoming solar radiation and the shape of the parabolic dish during manufacturing [40]. It varies from less than 10° to more than 90°. The value of rim angles decreases when the focus point increases [38].

Solar concentrator's use a truncated portion of the primary parabola curve. The extent of this truncation is usually defined in terms of rim angle or ratio of the focal length to aperture diameter f/d [33]. The figure shows the value of (f/Dconc.) at the same diameter of the concentrator at different rim angles. Rim angle can be determined using Equation (4.5).

$$\frac{f}{D_{conc}} = \frac{1}{4\tan\left(\frac{\phi_{rim}}{2}\right)} \tag{4.5}$$

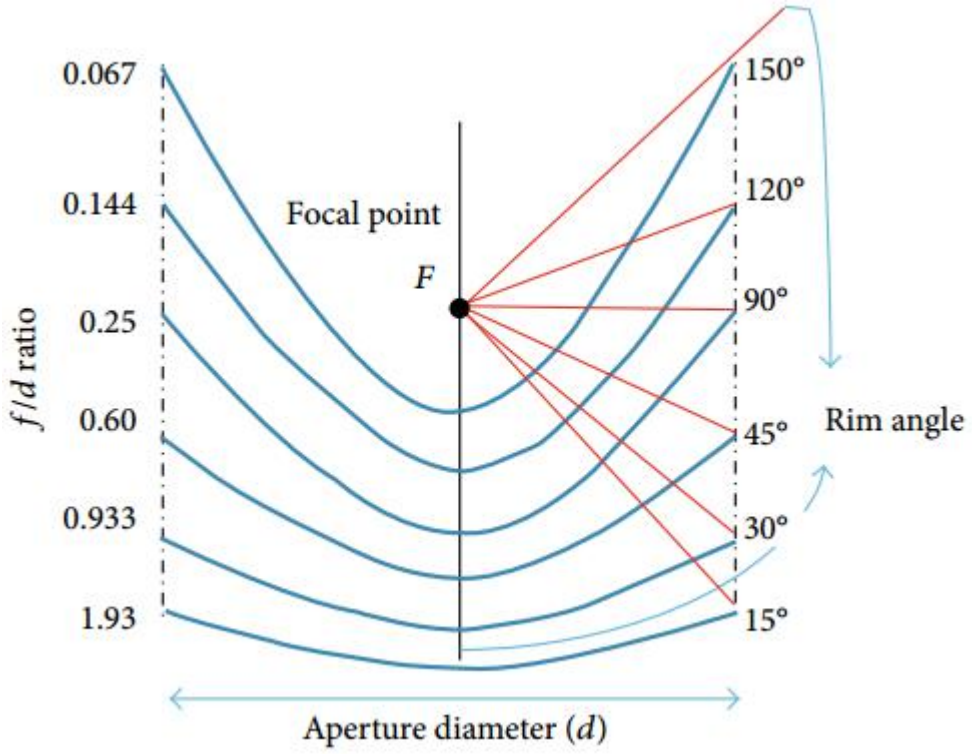

Figure 4.2: Relation between focal length and rim angles with the common focus point and same aperture diameter [31]

The receiver absorbs energy reflected by the concentrator and transfers it to the working fluid to produce the required usable thermal energy. The absorbing surface is usually placed behind the focus of the concentrator to reduce the flux intensity incident on it [35].

$$D_{rec} = \frac{D_{conc} * sin(\theta)}{sin(\phi_r)} \tag{4.6}$$

The receiver is used to collect the maximum amount of reflected solar radiation from the dish concentrator.

$$A_r = \frac{\pi D_r^2}{4} \tag{4.7}$$

The concentration ratio is defined as the ratio between the aperture area and the area of the receiver, as shown in Equation (4.7). It can be defined as the factor by which the incident energy flux at the aperture area of the concentrator is enhanced optically in the receiving area[36].

The higher the concentration ratio, means higher the temperature reaches the working fluid inside the receiver of the concentrator. The receiver's surface's heat losses decreased due to the smaller receiving area, and high energy conversion was achieved [37]. Concentration ratios vary from unity for flat plate collectors to a maximum of 46,747 for concentrated collector theoretically [30]. In a real system, that limit of solar concentration is unreachable due to non-ideality and losses.

$$C = \frac{A_{conc}}{A_{rec}} = \left(\frac{D_{conc}}{D_{rec}}\right)^2 \tag{4.8}$$

Arch length is found by integrating a differential segment of the basic parabola curve in Equation (4.9) and applying the limits x = h and y = d/2.

$$S = \left\{\frac{d}{2}\sqrt{\left(\frac{4h}{d}\right)^2 + 1}\right\} + 2f\ln\left\{\frac{4h}{d} + \sqrt{\left(\frac{4h}{d}\right)^2 + 1}\right\} \tag{4.9}$$

Another essential parameter to adequately define the geometry of the solar dish concentrator is the edge radius (r_r) or maximum distance value existing between the focal point and the paraboloid extreme.

$$r_r = \frac{2f}{1 + \cos(\phi_r)} \tag{4.10}$$

Design parameter and the calculated dimension of the parabolic dish concentrator through EES codes are summarized in table (4.3);

Table 4.3: Design parameter for parabolic dish solar concentrator

Parameters	**Numerical value**	**Unit**
Aperture diameter	2.8	m
Focal length	1.2	m
Depth of concentrator	0.4	m
Rim angle	59.5	Degree
f/d ratio	0.428	-
Minimum possible receiver diameter	0.015	m
Receiver diameter	0.2	m
Arch length	4.067	m
Concentration ratio	196	-
Rim radius	1.625	m

4.1.3 Performance Analysis of Solar Dish Concentrator

The optimal performance of the parabolic dish concentrator is mainly dependent on rim angle, the diameter of the receiver, and the concentration ratio of the concentrator [34]. The solar dish concentrator's performance is carried out based on the energy analysis using the first law of thermodynamics.

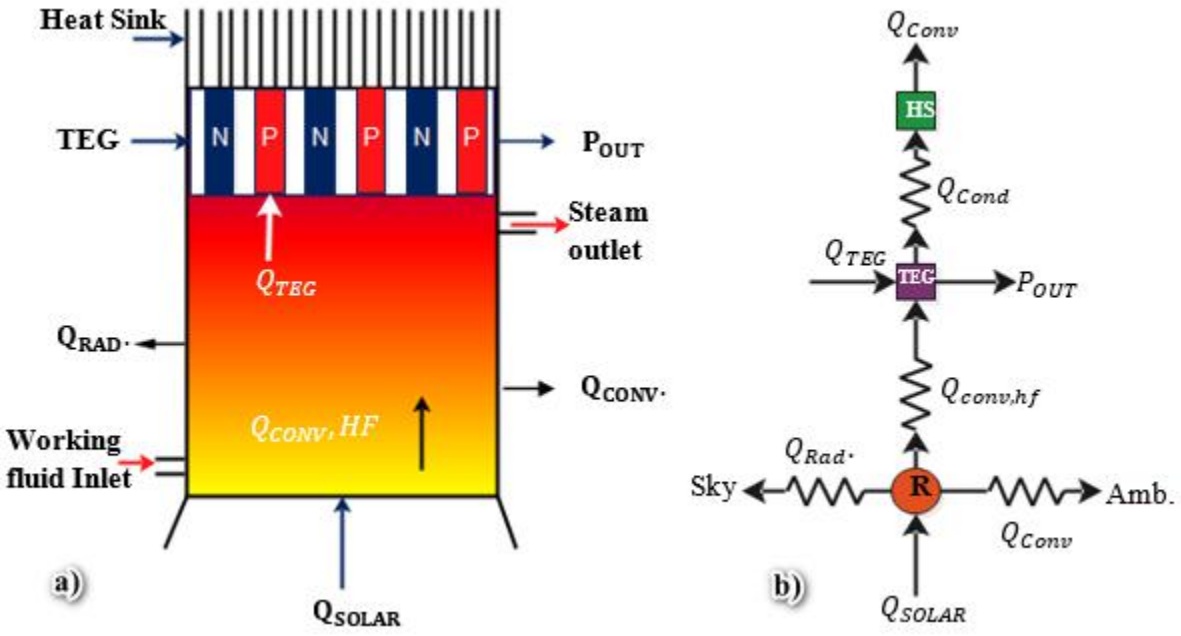

Figure 4.3: Schematic Diagram of CSP Receiver a) Energy Balance and b) Thermal Resistance Network Model of a Receiver dish Concentrator

Heat loss from the system to the surrounding

- **Convection loss**

Convection heat losses occur due to the presence of air at the wall of the receiver and the temperature level within it. The presence of head-on-wind and side-on-wind velocity over the surface of the absorber increases the convection loss.

The convective thermal losses from the receiver to the surroundings are proportional to the aperture surface of the absorber and the temperatures gradient between the absorber and the ambient air. It is given in the following equation [33];

$$Q_{CONV.} = h * A * (T_R - T_a) \tag{4.11}$$

Where ***h*** is the heat transfer coefficient and computed as;

$$h = h_{forced} + h_{natural}$$

To incorporate effects of wind velocity in heat loss calculation through forced convection, the heat transfer coefficient between the outer surface of receiver and ambient considering inclination of a receiver is computed using the relation stated in [42];

$$h_{forced} = 0.1967 * v_w^{1.849} \tag{4.12}$$

Natural convection occurs due to the density difference of working fluid inside the receiver and ambient air. The natural convective heat transfer coefficient is expressed in terms of Nusselt number (Nu_L), Grashof number (Gr), an inclination angle of a receiver (θ), characteristic length (L), and thermal conductivity of the air as shown in Equation (4.13).

$$h_{natural} = \frac{Nu_L k_{air}}{L} \tag{4.13}$$

The natural convective Nusselt number given as [35];

$$Nu_L = 0.106 * G_r^{\frac{1}{3}} * \left(\frac{T_R}{T_a}\right)^{0.18} * \left(4.256 * \frac{A_c}{A_w}\right)^{s} * h(\varphi) \tag{414}$$

Where; $s = 0.56 - 1.01 * \left(\frac{A_c}{A_w}\right)^{\frac{1}{2}}$

Gr is Grashof number, and it measures the relative magnitudes of the buoyancy force and the opposing viscous force acting on the fluid.

$$Gr = \frac{g\beta(T_R - T_a)L^3}{v^2} \tag{4.15}$$

Where; β is coefficient of volume expansion (1/K), v is the kinematic viscosity (m^2/s), g is the gravitational acceleration (m/s^2), φ is the inclination angle of a receiver from horizontal and k is a thermal conductivity of air (W/m.K). β, $v\ and\ k$ are properties of air and found by using film temperature ($T_f = 0.5(T_R + T_a)$).

An expression for convective heat coefficient as a function of the tilt angle was given by

$$h(\varphi) = 1.1677 - 1.0762 * sin(\varphi)^{0.8324} \tag{4.16}$$

- **Radiation loss**

Radiation heat loss from the receiver of CSP is proportional to the surface emissivity and the difference in temperature to the fourth power. The radiative heat losses from the hot and cold side tube of the receiver system to the surroundings are calculated using the following Equations;

$$Q_{RAD.} = \varepsilon * A * \sigma * \left(T_R^4 - T_a^4\right) \quad (4.17)$$

Where; σ is Stefan Boltzmann's constant and ϵ is the emissivity of the absorber material. If the absorber material is coated with the black surface, the emissivity value will be equal to one. In the present work, the outer surface of the receiver is assumed to be a black surface.

- **Total heat loss from the system**

The total heat loss from the system is the summation of the convection and radiation heat losses. Mathematically it is expressed as follows;

$$Q_{LT} = Q_{CONV.} + Q_{RAD.} \quad (4.18)$$

The energy absorbed by the receiver of the concentrator is expressed as;

$$Q_R = I * A_a * \eta_{opt} \quad (4.19)$$

Where; **I** is the direct normal irradiation falling on the concentrator, $\boldsymbol{A_a}$ is the aperture area of the concentrator and $\eta_{\boldsymbol{opt}}$ is the optical efficiency of the solar parabolic dish concentrator. It is the product of the coefficient of absorptivity, emissivity, and transmissivity of the concentrator.

The optical efficiency of the dish concentrator can be given as;

$$\eta_{\text{opt}} = \lambda\rho\tau\alpha\gamma\cos(\theta) \quad (4.20)$$

Where;

- λ is a shading factor which is dependent on the concentration ratio. The shading losses should be minimized as the concentration ratio increased and generally less than 1 % [41].
- ρ is the reflectivity of a dish material (for an aluminium reflector, it is 0.92) [44].

- γ is an intercept factor which is defined as the ratio of energy intercepted by a receiver to the energy that it receives from reflection coming from the parabolic dish. It can be from 97 to 99%.
- τα is the product of transmissivity and absorptivity of the material. The air gap between the concentrator and receiver causes a loss of transmissivity and absorptivity. It ranges from 2 to 4 % [41, 42].
- θ is an Incident angle

As the solar parabolic dish concentrator maintains its optical axis, always pointing directly towards the sun to reflect the beam, which means the incidence angle of the solar beam into the dish is zero degrees, and the cosine loss equals zero [42].

$$\eta_{opt} = \lambda\rho\tau\alpha\gamma \tag{2.21}$$

Considering the above analysis, optical efficiency is reduced to Equation (2.21), and the estimated value for this study should be **0.8374**, which is in the range of 0.83-0.85 as reported by [33, 42-43].

Useful thermal energy

The useful heat is the difference between total heat that reaches the focal plane and total heat losses from the absorber.

$$Q_U = Q_R - Q_{LT} \tag{4.22}$$

Where; Q_U useful thermal energy absorbed by the working fluid, Q_R heat supplied to the receiver and Q_L total heat losses from the receiver.

In another case, the rate of useful heat supplied to the working fluid given as;

$$Q_U = m * cp * \Delta T$$

Where; m is the mass flow rate of the working fluid, cp is specific heat capacity, and ΔT is the change of temperature between the operating fluid and ambient.

Performance of the receiver

The receiver's efficiency is a ratio of thermal heat collected by working fluid to the total energy supplied within the aperture of the concentrator.

$$\eta_R = \frac{Q_U}{Q_R} = \frac{Q_R - Q_{LT}}{Q_R} = 1 - \frac{Q_{LT}}{Q_R} \quad (4.23)$$

Concentrator efficiency

The efficiency of the dish concentrator can be defined as the ratio between useful outputs of energy to the input energy as given in Equation (4.24);

$$\eta_C = \frac{Q_U}{I * A_a} = \left(\frac{Q_U}{QS}\right) * \left(\frac{Q_R}{Q_R}\right) = \eta_R * \eta_{opt} = \eta_{opt} * \left(1 - \frac{Q_{LT}}{Q_R}\right) \quad (4.24)$$

4.1.4 Analyze of Solar Radiation Flux Distribution at a Receiver of a dish concentrator

SolTrace is a Monte-Carlo-based ray-tracing software which is developed by National Renewable Energy Laboratory (NREL). It is used in the solar energy field to model and analyze the optical performance of CSP. SolTrace is used to predict the ray intersection and flux distribution on the concentrator's absorber [45]. The first step to analyze ray tracing in SolTrace is to define the sun's shape and direction. The sun shape consists of three parameters, i.e., Gaussian, pillbox, and user-defined option. The sun direction is also defined in global coordinate or based on latitude, day, and hour. The next step is setting the optical properties of the concentrator. As shown in figure (4.4), optical properties include reflectivity, transmissivity, and optical errors. The optical error that occurs during ray analysis is specularity, slope, shape, and tracking system errors. Specularity error is defined relative to the reflected vector [46]. It is a factor 4 in Equation (4.25). Slope and shape errors are occurred by topographical deviations of the mirror surface. Slope error is related to material production, processing, and finishing of the mirror surface. The shape error refers to the deviation or deformation of a portion of the mirror caused by an external force, like wind or gravity [47]. Tracking error occurred due to an imperfect tracking system [44].

$$\sigma_{optical} = \sqrt{\left(4\sigma_{slope}^2 + \sigma_{specularity}^2\right)} \quad (4.25)$$

After defining the optical properties, the system geometry is created by setting stage properties and element definition with those stages. In this work, two-stage is created for the analysis. The first stage is preparing the concentrator's geometry, and the last stage is the absorber of the concentrator. A stage is clearly defined as a section of the geometry sequentially hit by rays propagating from the sun to the final receiver. The input parameter used for the analysis of ray tracing using SolTrace is summarized in table (4.4).

Finally, filling the parameter of ray tracing and extraction of the result is required to complete the analysis. In the tracing option, the desired number of ray intersection and the maximum number of rays to be generated on the concentrator will be set until the simulation converged. SolTrace generates the ray intersection between the concentrator and its absorber. SolTrace also analyzed the flux distribution in the form of contour and surface plot at the concentrator's receiver.

Table 4.4: Input parameter to the SolTrace software

Parameter	**Value/ type**	**Unit**
Sun shape: Pillbox	4.6	mrad
The reflectivity of the concentrator [44]	92	%
Transmissivity [44]	8	%
Slope error	2.5	mrad
Specularity error	0.2	mrad
Error type	Gaussian	-
Desired number of ray intersection	10000	-
Maximum number of sun rays generated	1000000	-

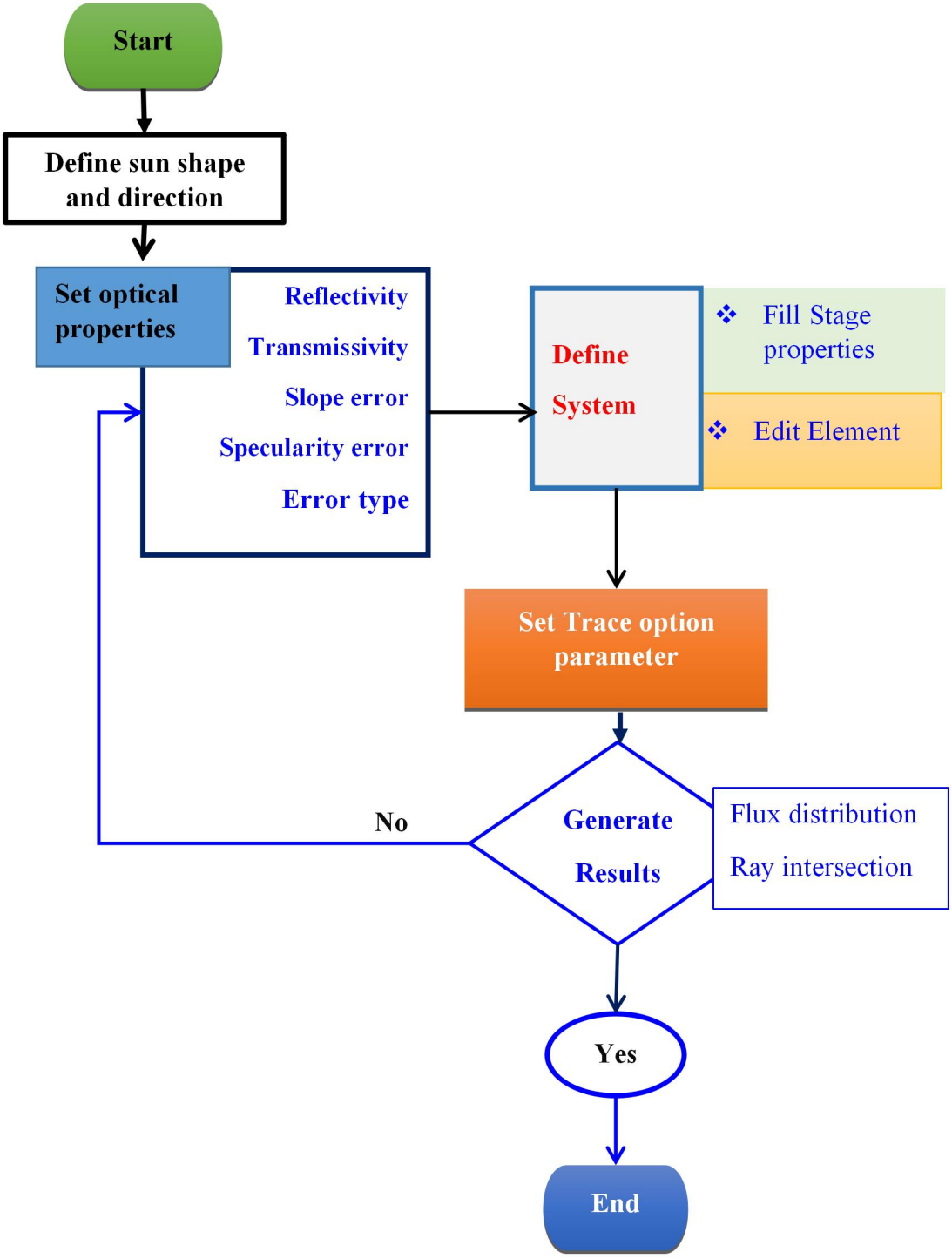

Figure 4.4: Flow chart of flux distribution analysis using SolTrace software

4.1.5 Energy required by a tracking system

In order to harness maximum solar energy, the dish concentrator must follow the path of the sun. In this study, a full tracking system or zero incidence angle is considered for during the calculation. Solar dish concentrators require a two-axis tracking system to track the sun path. The energy consumed by the servomotor during tracking depends on the weight of the system and aerodynamic forces [19].

The system's weight involves a mass of the dish, receiver, supports, and control system. By assuming the total mass of the system as 65 kg, the weight could be 637.65 N.

The aerodynamic force acting on the concentrator depends on the direction of wind flowing over the concentrator, and it is calculated as follows;

$$F_a = \frac{1}{2} * \rho * A_C * C_D * V_w^2$$

Where; ρ is the density of air, A_C is the concentrator area, C_D is an aerodynamic coefficient of the dish concentrator, and V_w is a wind velocity.

By considering the density of air 1.15 kg/m^3, area of the concentrator 6.158m^2, aerodynamic coefficient of 0.95, and an average wind velocity of the selected site 3.2m/s, the aerodynamic force could be 34.44 N.

So, the energy required by the tracking system is estimated as;

$$P_T = \frac{F * d * \cos(\theta)}{t}$$

Where; F is the total force (summation of weight and aerodynamic force), d is the distance covered during tracking, and “t” is the time.

By considering full tracking system over a given day and a rotation distance of 2.8 m, the power needed by servomotor during the tracking system could be equal to 6.27 W.

4.2 Thermoelectric Generator (TEG)

A thermoelectric device is an environmentally friendly and promising solid-state technology for converting thermal energy into electrical energy and vice versa as the temperature gradient occurs between the junctions of the material.

Thermoelectric is a phenomenon in which the temperature difference between two dissimilar materials creates the flux of electric charge due to the electromotive force existing in the circuit established by the two joints of the module. The thermoelectric module has a pair of (N) and (P) type semiconductors which allows the flow of electrons in the module. The electron flow from hot to cold side in (N) type, during the electron-hole flow in (P) type semiconductor.

The phenomenon of Seebeck was discovered by a German physicist Thomas J. See-beck in 1821 [20]. Thomas found that a circuit made of two dissimilar metals would deflect a compass needle if their junction were kept at two different temperatures. See-beck effect describes that if two different conductive materials subjected to a thermal gradient, the charge carrier migrates along the slope from the hot side to cold side to produce the induction of voltage [49]. The magnitude of the Seebeck effect increases with increasing the Seebeck coefficients of the conducting material and the thermal gradient between the hot and cold side junction of the TEG [21].

The induction voltage ratio to the temperature gradient is related to an intrinsic property of the thermoelectric material called the See-beck coefficient (thermopower). It is a measure of the entropy transported by the moving charge carrier divided by the carrier's charge. The temperature gradient between the two junctions of TEG is directly proportional to the voltage induced and inversely proportional to the Seebeck coefficient, as given in Equation (4.26). As shown, raising the temperature difference could increase the voltage developed in the circuit.

$$\alpha = -\frac{\Delta V}{\Delta T} = \frac{V_c - V_h}{T_h - T_c} \tag{4.26}$$

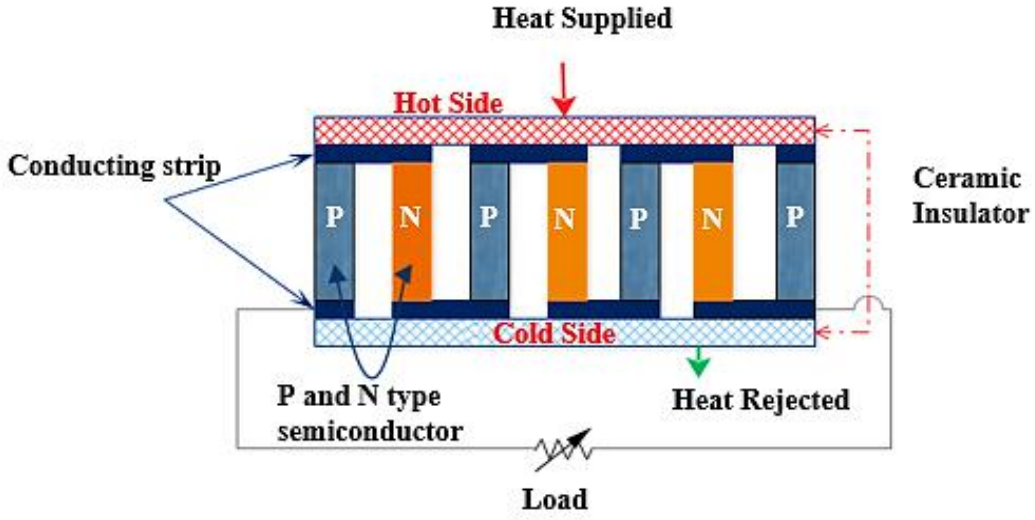

Figure 4.5: Working principle and construction of Thermoelectric Material

Figure (4.6) illustrates the schematic diagram of the working principle and construction of TEG material. As can be shown, the device consists of two ceramic insulators that are connected by a conductor to the pair legs of TEG (P and N-type) semiconductor, which is often called a thermoelectric couple. The conducting strip allows the material to connect electrically in series and thermally in parallel, and the ceramic insulator protects the module from the heat sink. As heat is supplied to the hot side of the module, the electron migrates from the hot to the cold side due to the temperature gradient between the module, and the potential voltage in the module generates an electric flux.

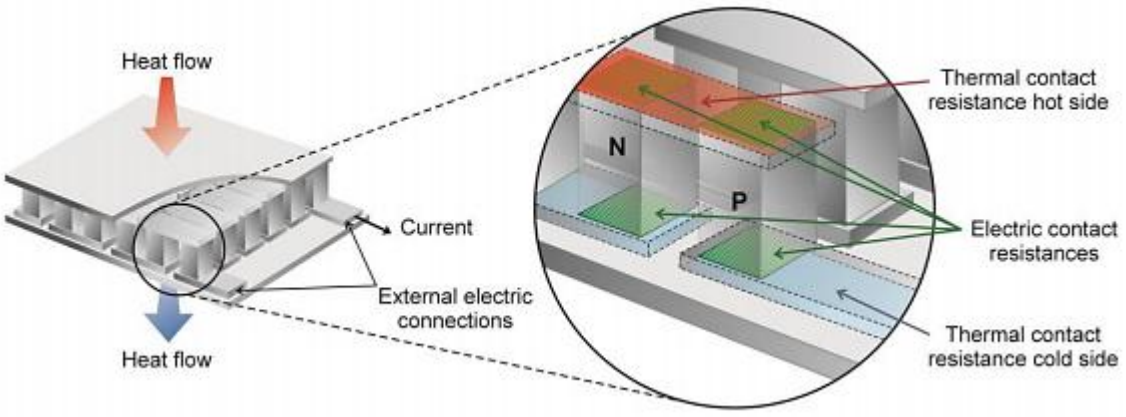

Figure 4.6: Contact Resistance within the TEG Module [50]

Four commercial bismuth telluride is used for the Multiphysics analysis of thermoelectric generator. A single module has 35*35*4.3 mm dimension.The material properties is summarized in table 4.5.

Table 4.5: Specification of a commercial thermoelectric module used for simulation [51]

TEHP1-12635-1.2 (Bi_2Te_3)	
Hot side temperature (^oC)	300
Cold side temperature (^oC)	30
Open circuit voltage (V)	8.3
Matched load resistance	2.2
Matched load output voltage (V)	4.2
Matched load output current (A)	1.86
Matched load output power (W)	7.8
Heat flow across the module (W)	132
Heat flow density (W/cm^{-2})	10.8
AC resistance measure under 27 ^oC at 1000 Hz	1.1-1.5

4.2.1 Design of Heat Sink for Thermoelectric Generator

A heat sink is a heat exchanger device that dissipates heat from the surface of a hot component while operating. The heat sink is integrated with TEG to maintain the temperature of the cold side of the module. A conduction heat is transferred from the TEG module to fins, and heat is removed from heat sink to ambient through natural convection. According to buoyancy effects, the heat dissipates from the module as airflow through the heat sink [49].

The natural convection heat transfer on the surface of the heat sink depends on the fins' geometry, the orientation of the heat sink, a variation of temperature, and thermophysical properties of the working fluid [52]. Heat sinks are made up of aluminum, and design of heat sink depends on the significant heat transfer coefficient. Aluminum is selected as heat sink material due to high thermal conductivity, ease of forming, corrosion resistance capability and lower cost.

Table 4.6: Material properties of the heat sink system

Properties of heat sink material	Parameters	Value	Unit
Coolant (air) @film temperature of 308.15 K	Thermal conductivity	0.02625	W/m*K
	Prandtl number	0.728	-
	Kinematic viscosity	$1.655*10^{-5}$	m^2/s
	Coefficient of volume expansion	0.00324	1/K
Aluminium	Density	2700	Kg/m^3
	Specific heat at constant pressure	900	J/(k*kg)
	Thermal conductivity	238	W/m*K
	Electrical conductivity	$3.774*10^7$	S/m

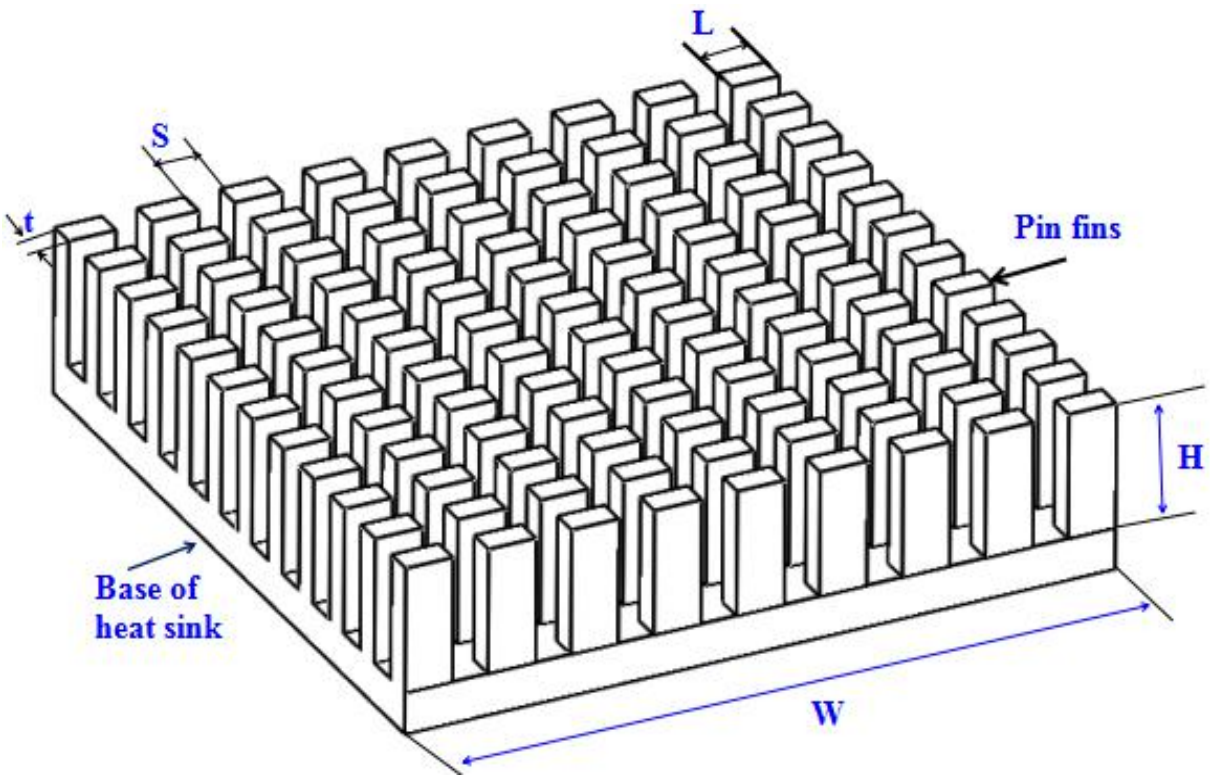

Figure 4.7: Geometric parameters of pin fin heat sink

The physical size of the base plate of a heat sink is 140 mm*140mm width with a thickness of 1 mm, the height of each pin is 12 mm. The size of the top surface of the pin fin is 5*3mm, and the optimal spacing between the fin of the heat sink is 3.2 mm with a total number of 529 fins as shown in figure (4.7).

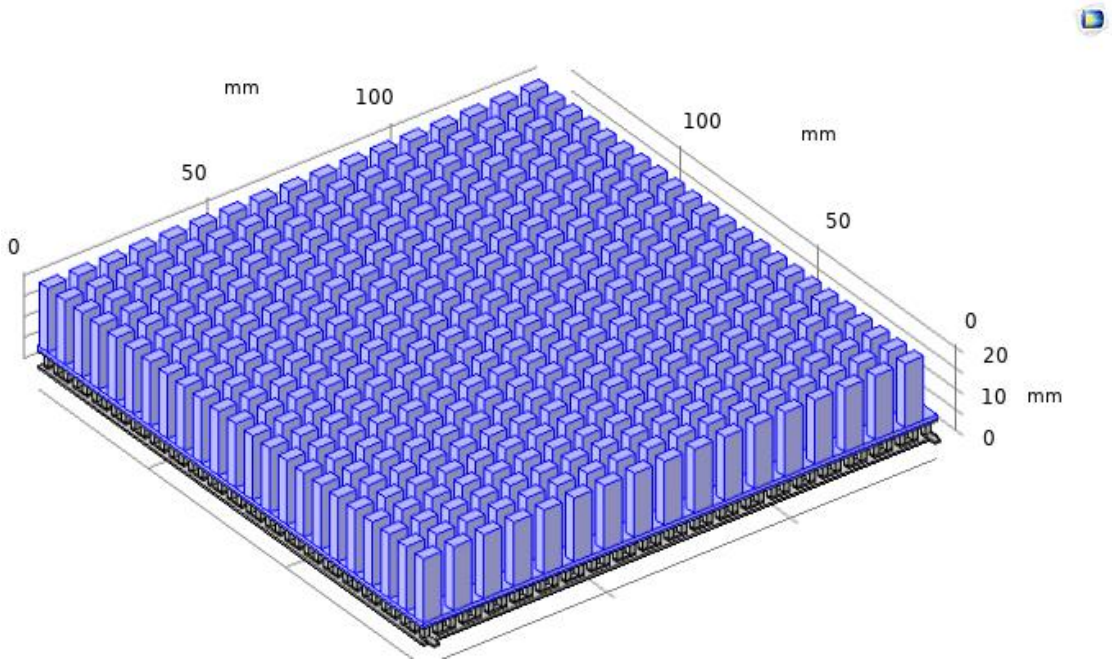

Figure 4.8: Geometry of heat sink coupled with TEG module

The calculation method used to design heat sink is according to the formula stated in [52].

The flow regime in natural convection is governed by a dimensionless number called the Grashof number, which represents the ratio of the buoyancy force to the viscous force acting on the fluid and is expressed as;

$$\mathrm{Gr_L} = \frac{\mathrm{g} * \beta * (\mathrm{T_s} - \mathrm{T_a}) * \mathrm{L}^3}{\mathrm{v}} \qquad (4.27)$$

$$Gr_L = \frac{9.81 * (0.0034) * (30) * (0.005)^3 * 0.728}{\left(1.655 * 10^{-5}\right)^2} = 435.15$$

Where; Lc is the characteristic length, which is the height L for a vertical plate

The natural convection heat transfer correlation is expressed in terms of the Rayleigh number. It can be estimated as follows;

$$\mathrm{Ra_L} = \mathrm{Gr_L} * \mathrm{P_r} = 435.15 * 0.728 = 316.79$$

The average Nusselt number for vertical isothermal parallel plates of spacing S and height L is given as

$$\mathrm{Nu} = \frac{\mathrm{h} * \mathrm{S}}{\mathrm{k}} = \left[\left(\frac{576}{\left(\frac{\mathrm{Ra_s} * \mathrm{S}}{\mathrm{L}}\right)^2}\right) + \left(\frac{2.873}{\left(\frac{\mathrm{Ra_s} * \mathrm{S}}{\mathrm{L}}\right)^{0.25}}\right)\right]^{-0.5} \quad (4.28)$$

The optimum fin spacing for a vertical heat sink and Nusselt number for optimally spaced fins is;

$$\mathrm{S_{opt}} = 2.174 * \left(\frac{\mathrm{S}^3 * \mathrm{L}}{\mathrm{Ra_s}}\right)^{0.25} = 2.714 \frac{\mathrm{L}}{\mathrm{Ra_s^{0.25}}} \quad (4.29)$$

$$\mathrm{Nu_{opt}} = 1.307$$

Substituting the value of Rayleigh number into Equation (4.29), the optimum spacing of the fin is 0.00316 m, and the number of fins on the heat sink calculated as;

$$\mathrm{n} = \frac{\mathrm{w}}{\mathrm{s_{opt}} + \mathrm{t}} = 0.\frac{14}{0.003216 + 0.003} = 22.52 \approx 23$$

The heat transfer coefficient is obtained from;

$$\mathrm{h} = \mathrm{Nu_{opt}} * \frac{\mathrm{k}}{\mathrm{s_{opt}}} \quad (4.30)$$

$$h = \frac{1.307 * 002625}{0.00324} = 10.58 \frac{W}{m * K}$$

The rate of heat transfer by natural convection from fins;

$$\mathrm{Q} = \mathrm{hA_s} * (\mathrm{T_s} - \mathrm{T_a}) \quad (4.31)$$

$$\mathrm{Q} = \mathrm{h} * (2\mathrm{nL}) * (\mathrm{T_s} - \mathrm{T_a})$$

Substituting the values into equation (4.31), the amount of heat dissipated from the cold side of the module is;

$$Q = 10.58 * (2 * 23 * 23 * 0.005 * 0.012) * 30 = 20.148\, W$$

4.2.2 Performance Analysis of Thermoelectric Generator (TEG)

TEG's performance primarily depends on the types of material used for construction and the physical properties of the material. TEG's electrical efficiency conversion relies on the figure of merit (which is determined by three main material parameters like see-beck coefficient, electrical conductivity, and thermal conductivity) and the temperature gradient between the hot and cold side of the module [53]. Despite material properties, the construction and geometry of the device and the macroscopic heat and electronic transport is an important parameter that has been taken into account in the real conversion efficiency of TEG [20].

The maximum energy conversion efficiency of ideal TEG operating under optimal condition can be estimated using Equation (4.32);

$$\eta_{TEG,max} = \left(\frac{T_h - T_c}{T_h}\right) * \frac{\sqrt{1+ZT}-1}{\sqrt{1+ZT}+\left(\frac{T_c}{T_h}\right)} = \eta_c * \frac{\sqrt{1+ZT}-1}{\sqrt{1+ZT}+\left(\frac{T_c}{T_h}\right)} \qquad (4.32)$$

Where; $\boldsymbol{T_h}$ is the hot-side temperature of the module, $\boldsymbol{T_c}$ is the cold side temperature, η_c is Carnot efficiency and **ZT** is a figure of merit or goodness factor of the material, which is a parameter used to characterize the performance of TEG or measure the amount of thermal energy converted to electrical energy due to temperature gradient [20]. It is given as;

$$ZT = \frac{\alpha^2 T}{\rho k} = \alpha^2 \delta \frac{T}{k} \qquad (4.33)$$

Where; $\boldsymbol{\alpha}$ is a see-beck coefficient, $\boldsymbol{\rho}$ is electrical resistance, $\boldsymbol{k}$ is thermal conductivity which describes the material ability to conduct heat through the material, $\boldsymbol{\delta}$ is electrical conductivity that measures the ability of the material to move charge carrier through material and $\boldsymbol{T}$ is an absolute temperature which is an average of hot side and cold side temperature. The physical properties of the TEG module like electrical resistance, Seebeck coefficient, and thermal conductivity are dependent on the absolute temperature of the module and expressed as [54].

$$\alpha = (22224 + 930.6T - 0.9905T^2) * 10^{-9}$$
$$\rho = (5112 + 163.4T + 0.6279T^2) * 10^{-10}$$
$$k = (62605 - 277.7T + 0.4131T^2) * 10^{-4}$$

The Seebeck coefficient of the TEG is increasing as the absolute temperature of the module increases. The figure shows the impact of the temperature on Seebeck or the goodness factor of the material. The higher the Seebeck coefficient, the higher figure of merit. So, the conversion efficiency is increasing.

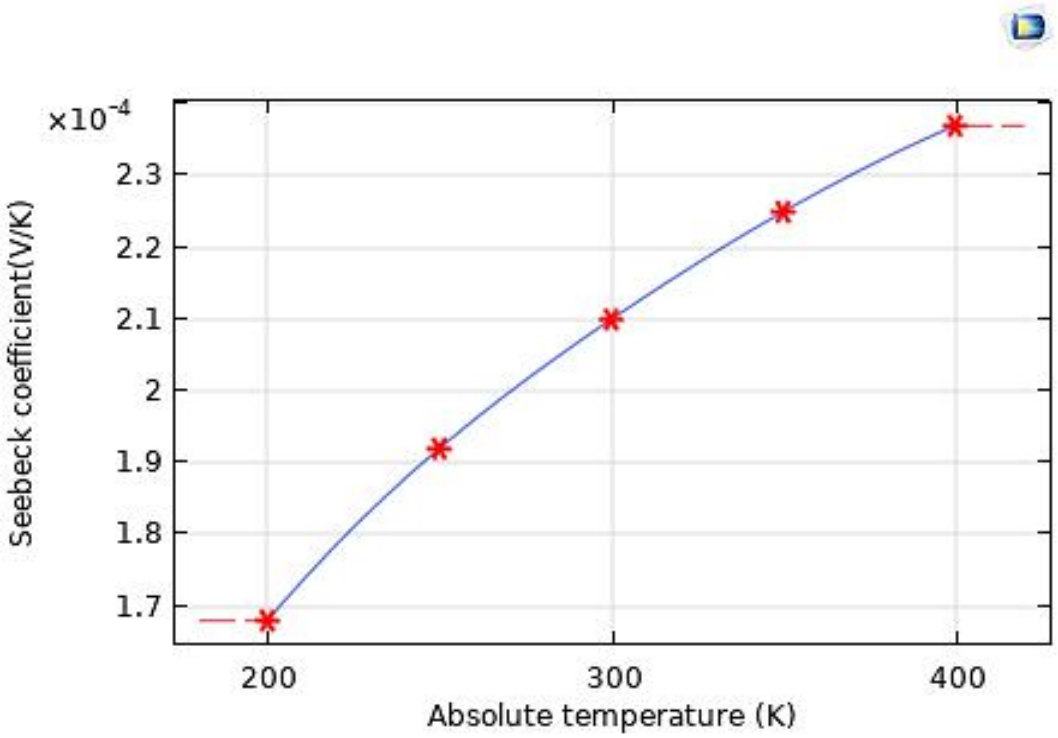

Figure 4.9: Effect of temperature on the Seebeck coefficient of a thermoelectric module

Figure (4.10) and (4.11) shows the variation of electrical resistivity and thermal conductivity of the TEG material with an average temperature of the module. As can be seen, the electrical resistivity increases with increasing the temperature. In contrast, the thermal conductivity can vary depending on the temperature value.

The material with a high Seebeck coefficient, good electrical conductivity, and small thermal conductivity can provide better thermal and chemical stability toward improving TEG performance.

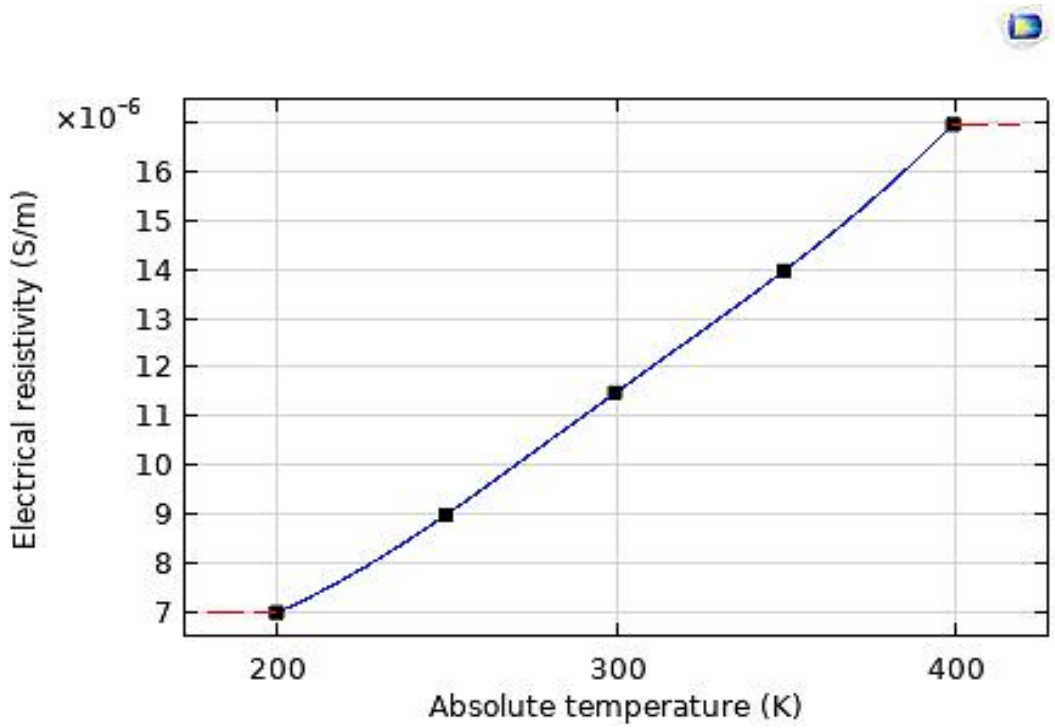

Figure 4.10: Variation of electrical resistivity of TEG with temperature

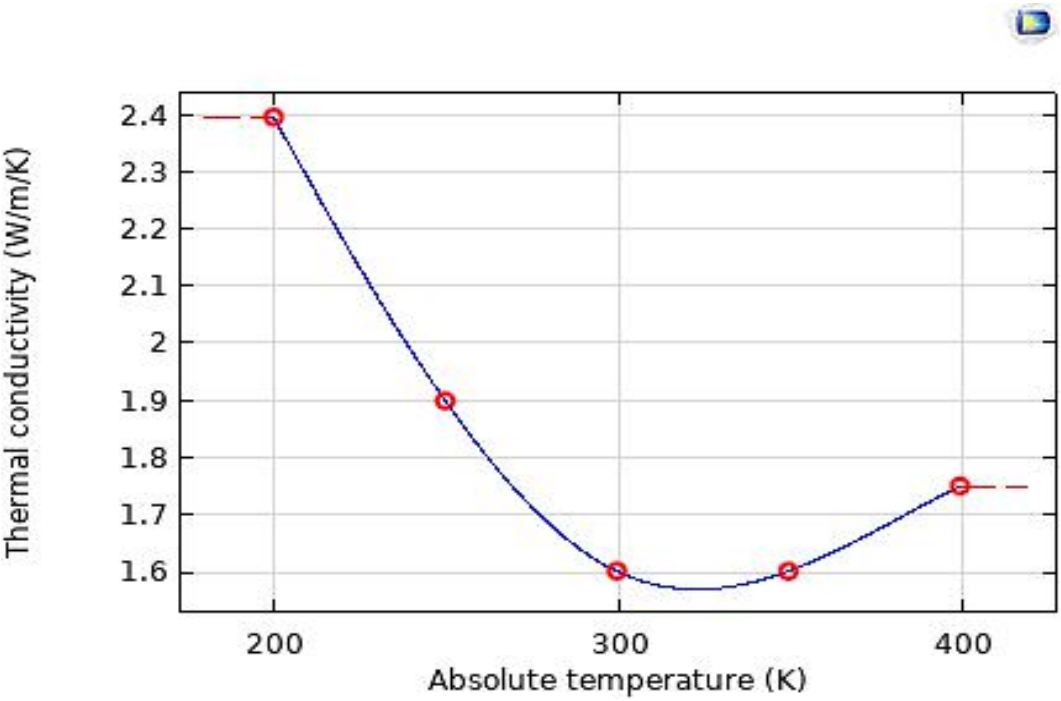

Figure 4.11: Variation of thermal conductivity of TEG with temperature

Energy generated by TEG module

The heat flux supplied to the hot side and released from the cold side of TEG semiconductors due to the Seebeck effect is given as;

$$Q_{TEG} = (\alpha * I * T) \tag{4.34}$$

Where; $\alpha = \alpha_p - \alpha_n$

The Joulian heat flux of one pair of TEG semiconductor is

$$Q = I^2 R \tag{4.35}$$

The heat flux developed due to the temperature difference between the two ends of TEG according to Fourier law of heat conduction is given as;

$$Q = k * (T_h - T_c) \tag{4.36}$$

Balancing the total heat flux generated by the TEG module, the rate of heat flow into the hot side and heat rejected from the cold side of the module can be estimated as follows [55,60].

$$Q_{TEG,h} = (\alpha * I * T_h) + (k * \Delta T) - \left(\frac{I^2 * R}{2}\right) \tag{4.37}$$

$$Q_{TEG,c} = (\alpha * I * T_c) + (k * \Delta T) + \left(\frac{I^2 * R}{2}\right) \tag{4.38}$$

Where, $Q_{TEG,h}$,$Q_{TEG,c}$, T_h , T_c, k, I and R are the heat rate input in the hot side, heat rejected from the cold side, the temperature of a hot side, the temperature of the cold side, thermal conductivity, electric current of the module, and resistance of the module respectively.

The power produced by the module can be estimated by applying energy balance in the TEG module

$$P_{TEG} = Q_{TEG,h} - Q_{TEG,c} = (\alpha * I * \Delta T) - (I^2 * R) \tag{4.39}$$

The output current and voltage induced by the TEG module are given as;

$$I = \frac{\alpha \Delta T}{R_{int} + R_L} \tag{4.40}$$

$$V = IR_L = R_L * \left(\frac{\alpha \Delta T}{R_{int} + R_L}\right) \tag{4.41}$$

Where; R_L is external resistance load and R_{int} is the internal resistance of TEG

The output electrical power induced by TEG expressed as

$$P = N * I^2 * R_L \tag{4.42}$$

The maximum output power of the TEG module is achieved when the load resistance is equal to internal resistance ($R_L = R_{int}$) and given as;

$$P_{max} = \frac{(\alpha * \Delta T)^2}{R_{int} + R_L} \tag{4.43}$$

The thermal -to- electrical energy conversion efficiency of TEG can be calculated as;

$$\eta_{elect} = \frac{P}{Q_h} \tag{4.44}$$

4.3 Design Thermal Stirling Pump

Stirling engine is an external combustion engine that works on a closed thermodynamic cycle with an external heat source via hot end and cold end. It converts heat energy into useful mechanical energy using a compressible working fluid like air, hydrogen, helium, and nitrogen. Considering ideal regeneration with Isothermal expansion and compression process Stirling engine can theoretically achieve the Carnot engine's performance. The heat source used for the Stirling engine operation is solar energy, biomass, and combustible materials. Stirling engines have plenty of advantages like environmentally friendly, free emission, and silent operation [63].

4.3.1 Stirling Engine Cycle

Stirling engine has an idealized thermodynamic process of two Isothermal and two isochoric processes [64].

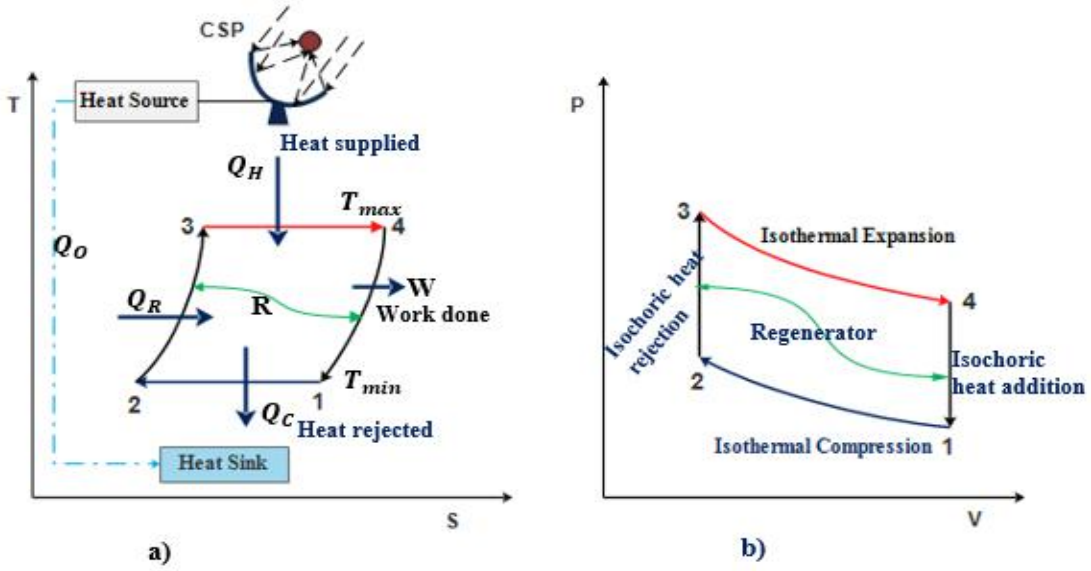

Figure 4.12: Diagram of Stirling Engine Cycle; a) T-S (Temperature- Entropy) diagram and b) P-V (Pressure-Volume) diagram

- **Isothermal compression process (1-2)**

In this process, the working fluid is compressed at a constant low temperature in compression space, and heat is rejected to the cold sink to maintain the gas's temperature as much as possible. The volume of the working gas decreases while the pressure of the gas increase during this process.

- **Isochoric cooling process (2-3)**

Regenerators absorb heat from working fluid at constant volume during the process from expansion to compression space. Heat is transferred from the working gas to the regenerator, causing the pressure, temperature, internal energy, and the working fluid's entropy to decrease. In this process, less work needs to be done by the piston to compress the gas on the return stroke, giving a net gain in power available on the shaft.

- **Isothermal expansion process (3-4)**

During this process, the engine's expansion space is maintained at a constant high temperature, and the working fluid expands as the heat absorbed from an external heat source. As the expansion piston moves away from the regenerator toward the outer dead piston, the working fluid is expanded in an enclosed cylinder, and a piston does the useful work. In this process, the gas-causing decrease in pressure increases while an increase in volume and entropy.

- **Isochoric heating process (4-1)**

The working gas passes through the regenerator at constant volume, and the heat is dissipating from regenerative to the working fluid. The working fluid transferred from compression space to expansion space through regenerative causes an increase in pressure, temperature, internal energy, and gas entropy. In this process, the expansion piston moves away from regenerative, and the compression piston moves toward regenerative simultaneously.

4.3.2 Stirling Engine Configuration

Depending on cylinder arrangement, a Stirling engine is classified into alpha, beta, and gamma type [64, 66].

Alpha Type

An Alpha Stirling engine contains two power pistons (expansion and compression piston) and two cylinders connected via regenerator. The cylinders have hot and cold sides connected to the flywheel and are usually aligned perpendicular to each other, as shown in figure (4.13 a). The hot cylinder is situated in a high-temperature heat exchanger, while the cold cylinder locates near a low-temperature heat exchanger. Alpha Stirling engines have a high power-to-volume ratio, i.e., at a given volume, the highest power is developed by the machine.

Beta Type

A beta Stirling engine is a displacer type Stirling engine that consists of one power piston with a coaxial displacer in the same cylinder. Both power piston and displacer are connected to a single flywheel at different points with a 90^{o} phase angle.

Beta Stirling engine has a high compression ratio so that it can give higher power capability. The beta configuration provides an advantage in better sealing, compactness, lower dead space, and overlapping.

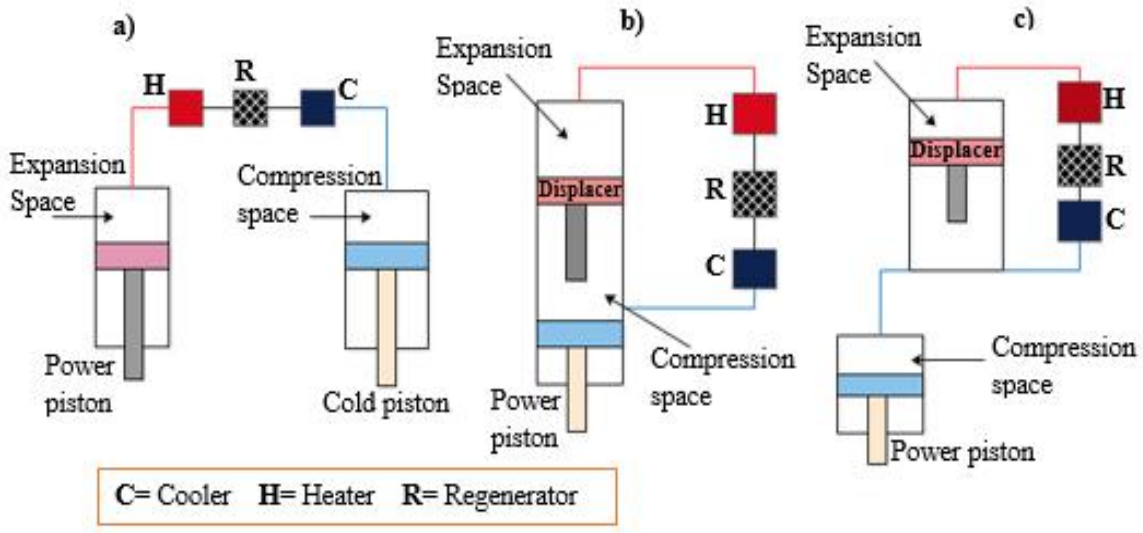

Figure 4.13: Configuration of Stirling Engine a) Alpha Type, b) Beta Type and c) Gamma Type of Stirling Engine

Gamma Type

Like a beta Stirling engine, a gamma Stirling engine is a displacer type that has power piston and displacer separately. The displacer allows a complete separation between the heat exchangers associated with the power piston and displacer cylinder. One piston of the engine converts the gas pressure into useful work, and the other one is used to move the gas between the hot and cold space heat exchanger. Gamma Stirling engine can achieve excellent theoretical performance by using a simple method and adiabatic condition.

Depending on the ease of sealing, design simplicity, compression ratio, the power to volume ratio, and maintenance, a beta Stirling engine was chosen in this work.

4.3.3 Selection of Working Fluid

Proper selection of working fluid for the Stirling engine has an essential benefit for its performance, output power, and safety. Helium, hydrogen, and air are the most used working fluid in a Stirling engine. The selection of the working fluid depends on thermodynamic, heat transfer, and gas dynamic properties.

Also, ease of availability, cost, and safety operation must have to be in the account. The parameter used for selecting working fluid for the Stirling pump depends on the fluid's thermophysical properties like Low heat capacity, low viscosity, high thermal conductivity, low rate of diffusion, and non-flammability [75].

Thermal conductivity controls the process of heat transfer to the fluid and from the fluid in expansion space, regenerative, and compression space. Density and viscosity are related to the flow friction losses, which control the pump work necessary to move the engine's fluid to perform the desired heat transfer from the heater or to the cooler.

Table 4.7: Selection Criteria of Stirling engine Working Fluid [75-77]

Criteria	Helium	Hydrogen	Air
Heat capacity	Very low	Low	High
Viscosity	Low	Low	High
Diffusivity	High	High	Low
Thermal conductivity	High	Very high	Low
Flammability	No	Yes	No
Availability	Rare	Less	Easily available
Cost	Very expensive	Expensive	Cheap

By considering the thermophysical properties, the air is selected as a working fluid in this work. Regarding the problem associate with contamination and supply, the air is the most preferable working fluid in a Stirling engine. Even most of the Stirling engines working with air usually operate at pressures close to the atmospheric pressure.

4.3.4 Analysis of Stirling Engine

The Stirling engine analysis was carried out depending upon the technique performed by Martini [65]. It consists of zeroth order, first-order, second-order, and third-order analysis, as shown in figure (4.14). Zeroth Order Analysis depends on the William Beale correlation obtained from various experimental data. The correlation helps to predict the performance of the Stirling engine using the Beale formula [65]. First Order Analysis (Schmidt Analysis) is based on the assumption of ideal isothermal. Gustav Schmidt introduces this analysis using a closed-form solution for sinusoidal volume variation and isothermal hot and cold space. His theory focuses on harmonic pistons and device node movements, ideal isothermal expansion and compression, and ideal regeneration [65-66].

A second-order analysis is depending on an adiabatic analysis and the modified Schmidt analysis. The analysis considers losses caused by heat transfer and flow of power and requires non-linear time integration of the model equation [65, 67]. It is the most realistic way of analysis to predict the performance of the engine. Third Order Analysis depends on control volume or nodes to solve a directly homogeneous equation or one-dimensional governing equation [65, 67].

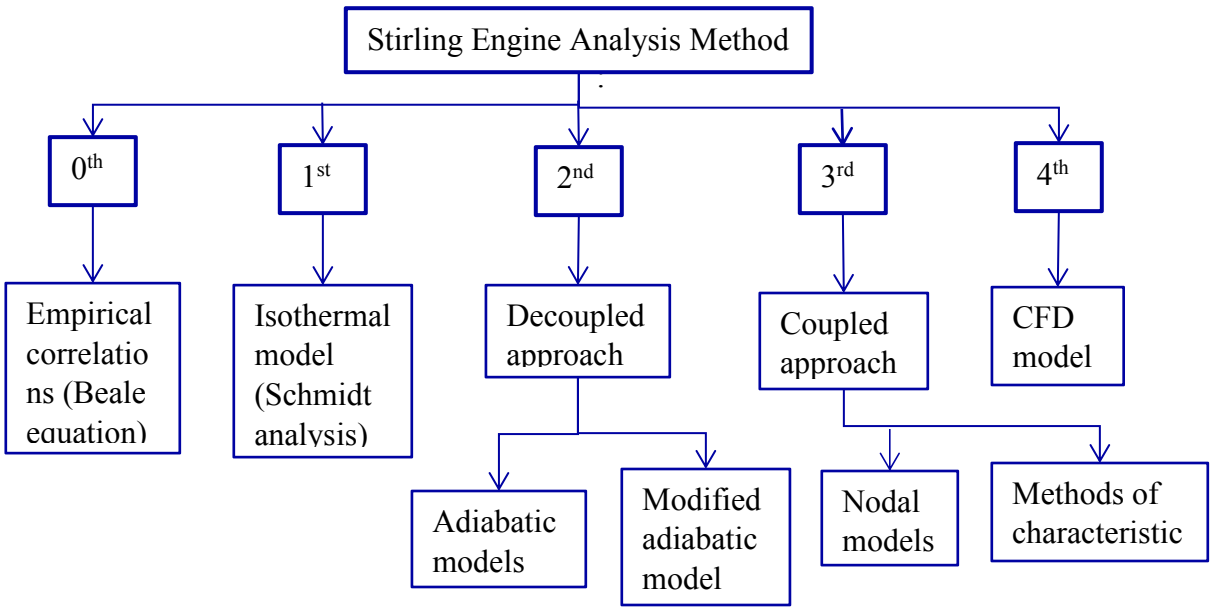

Figure 4.14: Stirling engine analysis method [73]

Second-Order Analysis of Stirling Engine

Uriel and Berchowitz developed an ideal adiabatic analysis of the second-order Stirling engine model [69].

An assumption made by the ideal adiabatic model [68-70]

- The working fluid of the engine obeys the ideal gas
- Perfect/ideal regenerator
- The temperature of working fluid inside the heater and cooler heat exchanger is assumed to be constant and equal with external wall temperatures
- The gas inside expansion and compression space is taken as adiabatic
- There is no gas leakage, thermal and friction losses in any part of the engine

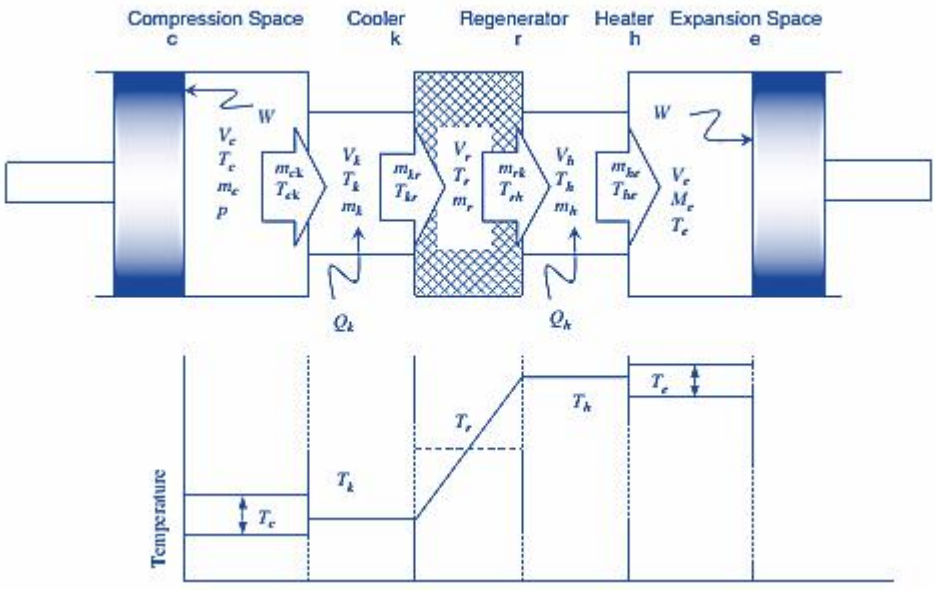

Figure 4.15: Diagram of Control Volume and Temperature Profile of Second-Order Stirling Engine Analysis [69]

The ideal adiabatic analysis of the Stirling engine is performed through Matlab. The flow chart of the analysis is given below in figure(4.16)

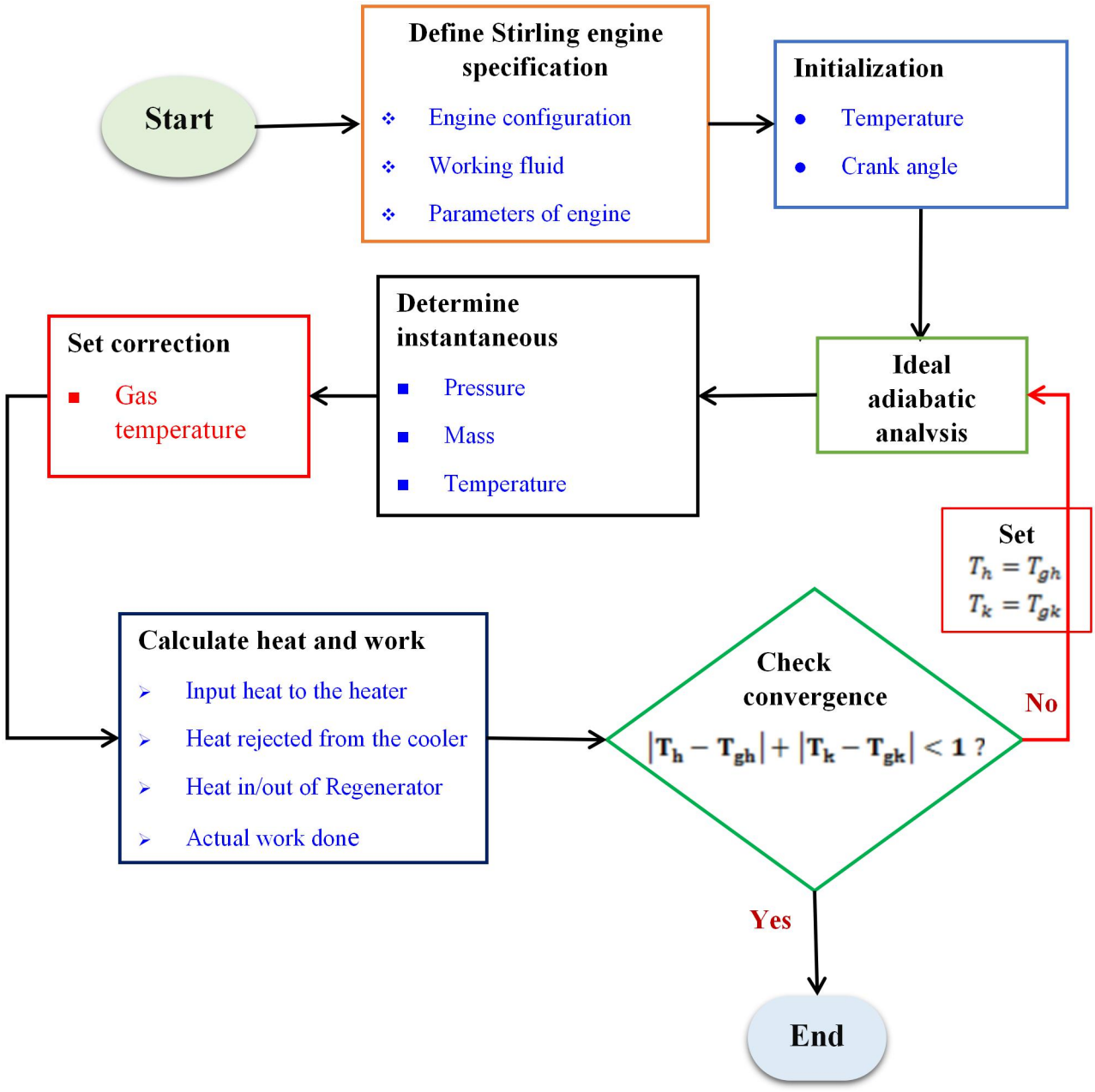

Figure 4.16: Flow chart of Second-Order Ideal Adiabatic Analysis

Expansion space volume

$$V_E = \frac{V_{SD}}{2}(1 + cos(\phi)) + V_{DE} \tag{4.45}$$

$$V_{SD} = L_d * A_{de}$$

Where; V_E is the expansion space volume, V_{SD} is swept volume of the displacer, V_{DE} is a dead volume in expansion space, and ϕ is the crank angle.

Compression space volume

$$V_C = \frac{V_{SD}}{2}(1 - cos(\phi) + \frac{V_{SP}}{2}(1 + cos(\phi - \alpha)) + V_{DC} \tag{4.46}$$

$$V_{SP} = L_p * A_p$$

Where; V_C is the compression space volume, V_{SP} is swept volume of the piston, V_{DC} is a dead volume in compression space, α is the phase angle and V_N is an overlap volume and it is formed due to overlap of piston and displacer stroke in the cylinder.

The total volume of an engine at any instant value of rotational speed

$$V = V_E + V_R + V_C \tag{4.47}$$

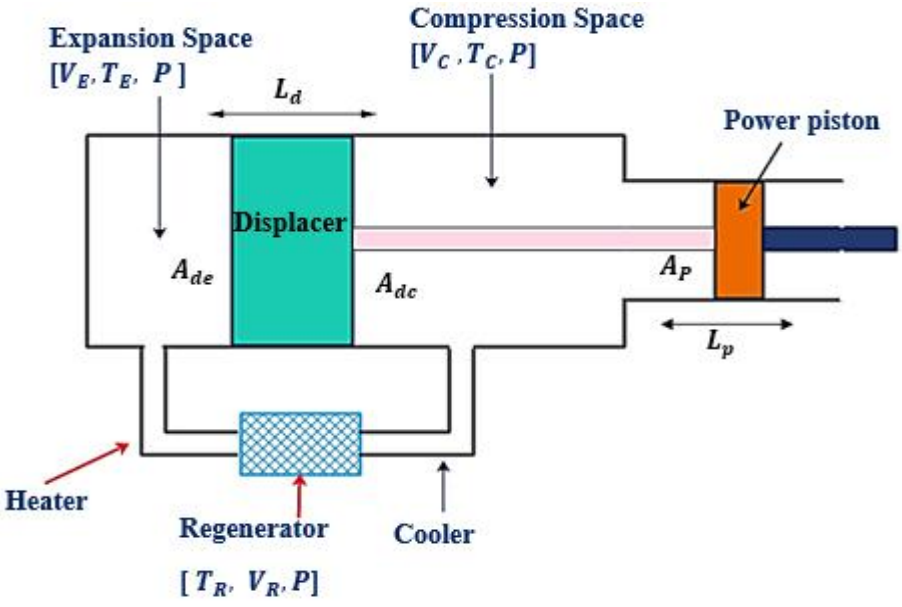

Figure 4.17: Graphical illustration of Beta type Stirling engine

Energy balance applied to a generalized control volume

By considering the first law of thermodynamics, the energy balance in the engine is computed as;

$$\begin{aligned}&\text{Rate of heat transfer into cell} + \text{Net enthalpy converted in cell}\\&= \text{Rate of work done on surrounding}\\&+ \text{Rate of increase of internal energy in the cell}\end{aligned}$$

$$dQ + \left(C_p T_i m_i - C_p T_o m_o\right) = dW_d + C_v d(mT) \tag{4.48}$$

Where; Cp and Cv are the gas's specific heat capacity at constant pressure and constant volume, respectively.

By considering the conversation law of mass, the total mass of the working fluid is defined as;

$$M = m_c + m_k + m_r + m_e + m_h \tag{4.49}$$

By differentiating the above equation

$$dm_c + dm_k + dm_r + dm_e + dm_h = 0$$

The behaviour of the gas is also considered as an ideal gas

$$PV = mRT \tag{4.50}$$

By taking the logarithm and differentiating, the equation is reduced to;

$$\frac{dP}{P} + \frac{dV}{V} = \frac{dm}{m} + \frac{dT}{T}$$

For all heat exchanger cells, the respective volume and temperature are constant

$$\frac{dP}{P} = \frac{dm}{m}$$

$$dm_c + dm_e + dP\left(\frac{m_k}{P} + \frac{m_r}{P} + \frac{m_h}{P}\right) = 0$$

$$dm_c + dm_e + \frac{dP}{R} * \left(\frac{V_k}{T_k} + \frac{V_r}{T_r} + \frac{V_h}{T_h}\right) = 0$$

Applying the energy balance to the compression cylinder and cooler heat exchanger

$$dQ_c - C_p T_{ck} m_{ck} = dW_c + C_v d(m_c T_c) \quad (4.51)$$

Since the compression space is in adiabatic condition $dQ_c = 0$ and the work-done by compression space is given as, $dW_c = PdV_c$ and differential dm_c is equal to the mass flow through the interface ck, m_{ck} reducing the equation to;

$$C_p T_{ck} dm_c = PdV_c + C_v d(m_c T_c)$$

By substituting the equation of state and ideal gas relations, the mass accumulation in compression and expansion space is given as;

$$dm_c = \frac{PdV_c + V_c * \left(\frac{dP}{\gamma}\right)}{RT_{ck}} \quad (4.52)$$

$$dm_e = \frac{PdV_e + V_e * \left(\frac{dP}{\gamma}\right)}{RT_{he}} \quad (4.53)$$

The differential pressure for each instant of the cycle

$$dP = \frac{-\gamma P\left(\frac{dV_c}{T_{ck}} + \frac{dV_e}{T_{he}}\right)}{\frac{V_c}{T_{ck}} + \gamma\left(\frac{V_k}{T_k} + \frac{V_r}{T_r} + \frac{V_h}{T_h}\right) + \frac{V_e}{T_e}}$$

Instantaneous pressure in all compartment of the engine

$$P = \frac{MR}{\frac{V_c}{T_c} + \frac{V_k}{T_k} + \frac{V_r}{T_r} + \frac{V_h}{T_h} + \frac{V_e}{T_e}} \quad (4.54)$$

Regenerator temperature

$$T_r = \frac{T_h - T_c}{log\left(\frac{T_h}{T_c}\right)} \quad (4.55)$$

The differential equation of the temperature in the work-spaces are derived from the ideal gas equation

$$dT_c = T_c\left(\frac{dP}{P} + \frac{dV_c}{V_c} - \frac{dm_c}{m_c}\right)$$

$$dT_e = T_e\left(\frac{dP}{P} + \frac{dV_e}{V_e} - \frac{dm_e}{m_e}\right)$$

Mass accumulation in each heat exchanger

$$m_i = \frac{PV_i}{RT_i}\ , i = k,r,h \tag{4.56}$$

$$m_e = M - (\ m_c + m_k + m_r + m_h)$$

$$dm_i = \frac{m_i dP}{P}, i = k,r,h$$

By considering the continuity equation, the mass flow over cell interface is given as;

$$m_{ck} = -\ dm_c$$

$$m_{kr} = m_{ck} - dm_k$$

$$m_{rh} = m_{kr} - d_{mr}$$

$$m_{he} = m_{rh} - dm_h$$

Conditional temperature based on the direction of flow

$$if\ m_{ck} > 0\ \ them\ T_{ck} = T_c, else\ T_{ck} = T_k$$

$$if\ m_{he} > 0\ \ them\ T_{he} = T_h, else\ T_{he} = T_e$$

Substituting the value of (m*T) and (dW) into equation (), an adequate form of that equation is obtained, which applies to each component;

$$dQ + \left(C_p T_i m_i - C_p T_o m_o\right) = \frac{C_p P dV + C_v V dP}{R}$$

In the heat exchanger space, no work is done since the respective volume is constant. The equation of heat flux in each heat exchanger is reduced to;

Heat input to the heater, regenerator, and heat rejected from the cooler heat exchanger is given in Equation (4.57 to 4.59).

$$dQ_h = \frac{V_h dPC_v}{R} - C_p(T_{rh}m_{rh} - T_{he}m_{he}) \quad (4.57)$$

$$dQ_r = \frac{V_r dPC_v}{R} - C_p(T_{kr}m_{kr} - T_{rh}m_{rh}) \quad (4.58)$$

$$dQ_k = \frac{V_k dPC_v}{R} - C_p(T_{ck}m_{ck} - T_{kr}m_{kr}) \quad (4.59)$$

The total work done by the engine is the algebraic sum of the work done by expansion and compression space

$$dW = dW_e + dW_c = P(dV_e + dV_c) \quad (4.60)$$

For non-ideal regenerator, the network-done by the Stirling engine is given as;

$$W_{NET} = Q_{hi} + Q_{ki} + 2 * Q_{ri} * (1 - e) \quad (4.61)$$

Where; Q_{hi} is the heat supplied, Q_{ri} is heat rejected from cooler, Q_{ki} is regenerator heat during an ideal case and e is the effectiveness of the regenerator.

The ideal adiabatic thermal efficiency of the Stirling engine

$$\eta_{ideal-stirling} = \frac{W}{Q_h} \quad (4.62)$$

For non-ideal regenerator, the thermal efficiency of the Stirling engine is given as;

$$\eta_{non-ideal} = \frac{\eta_{ideal}}{1 + \frac{Q_{ri}}{Q_{hi}} * (1 - e)} \quad (4.63)$$

4.3.5 Sizing of The Pump

The pump's sizing depends on the flow rate (Q) of the water in which the pump is required to deliver at a specific location and the total dynamic head (H_T) of a system that the pump must generate to provide the required flow rate.

The power consumed by the pump is estimated as;

$$P_H = \frac{P_{shaft}}{\eta_P} \tag{4.64}$$

Where; P_{shaft} is the shaft power from the engine and η_P is the pump efficiency

The amount of flow rate required will be estimated from the hydraulic power at a given total dynamic head as follows;

$$P_H = \frac{\rho g Q H_T}{3600} \tag{4.67}$$

Where; ρ is the density of water (kg/m^3), g is the gravitational acceleration (m/s^2), Q is the flow rate of water (m^3/hr.), and H_T is the total dynamic head (m)

$$Q = \frac{3600 * P_H}{\rho * g * H_T}$$

The daily water pumped by the system is;

$$Q = \frac{V}{t_S} = \frac{Daily\ water\ pumped\left(\frac{m^3}{day}\right)}{Average\ number\ of\ sunny\ hours\ per\ day} \tag{4.68}$$

The system capacity or flow rate required to meet the demand of the irrigation field is estimated according to the following equation [72].

$$Q = \frac{(Net_{app} * A)}{(H * D * E)} \tag{4.69}$$

Where: Q_S is total flow rate required to operate irrigation system ($\frac{m^3}{hr}$), Net_{app} is net irrigation depth needed per week (mm), A is a total area to be irrigated (hectare), H is total hours available to operate the system per day, D is a total day to operate each week, and E is the efficiency of the irrigation system.

CHAPTER FIVE

5. RESULT AND DISCUSSION

5.1 Estimation of Solar Radiation Data

Sunshine hour is an important parameter that helps to estimate the solar radiation at a given location. Newloc-Clim estimator can provide a sunshine hour based on an input of latitude and longitude for a given site. As shown in figure (5.1), the study area's sunshine duration is increasing from October to May and slightly decrease in the wet season. The result indicates a maximum of 9.53 sunshine hours in November and a minimum of 4.13 sunshine hours in July.

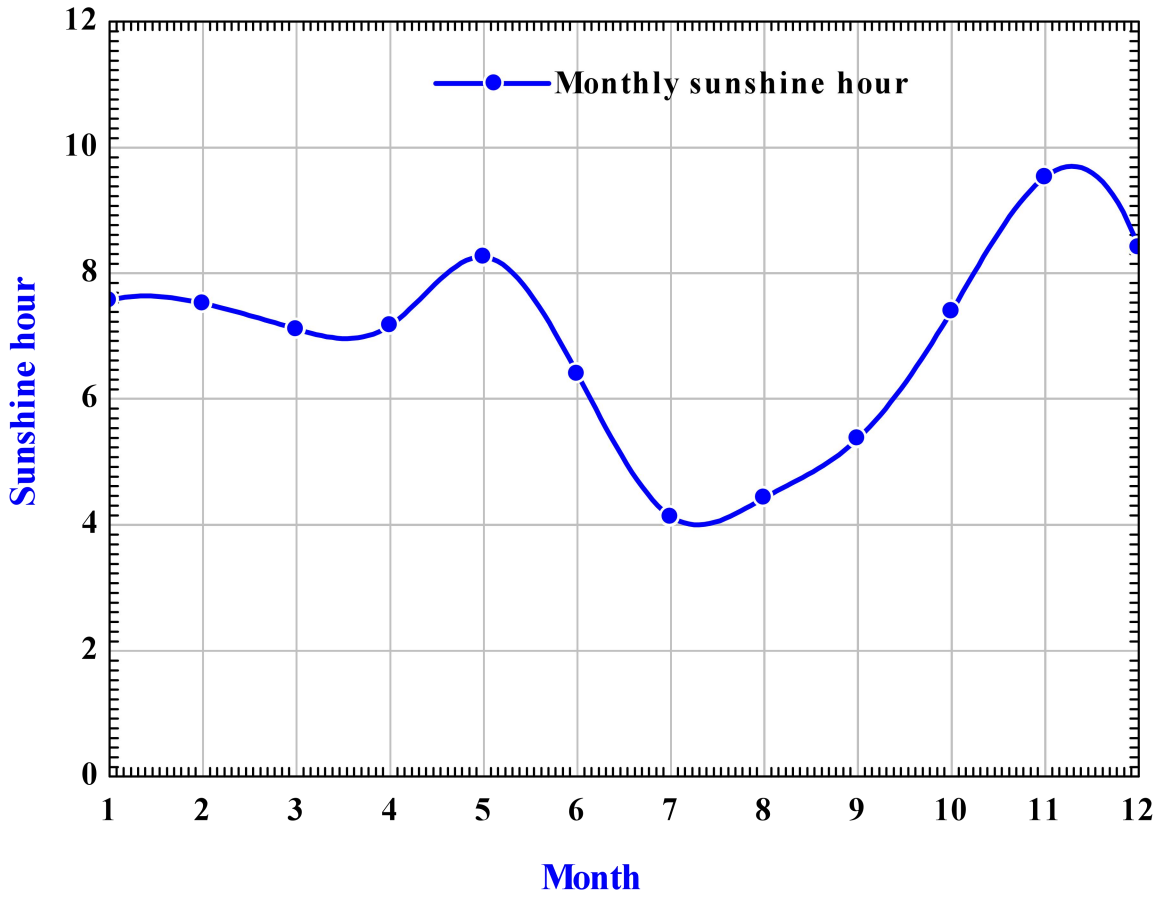

Figure 5.1: Monthly Average Daily Sunshine Duration

The monthly average daily global, beam and diffuse solar radiation from the site's horizontal surface were performed according to the sunshine hour model and the empirical correlation stated in equation (4.4). As presented in figure (5.2), the global solar radiation increases slightly from October to May, where the maximum of 24.99 MJ/m^2 is in May.

The solar radiation received by the solar dish concentrator is the direct solar radiation "DNI," and it is obtained from the difference between global and diffused solar radiation. The estimated result shows that a site has a remarkable beam solar radiation capacity in the selected months for the irrigation system.

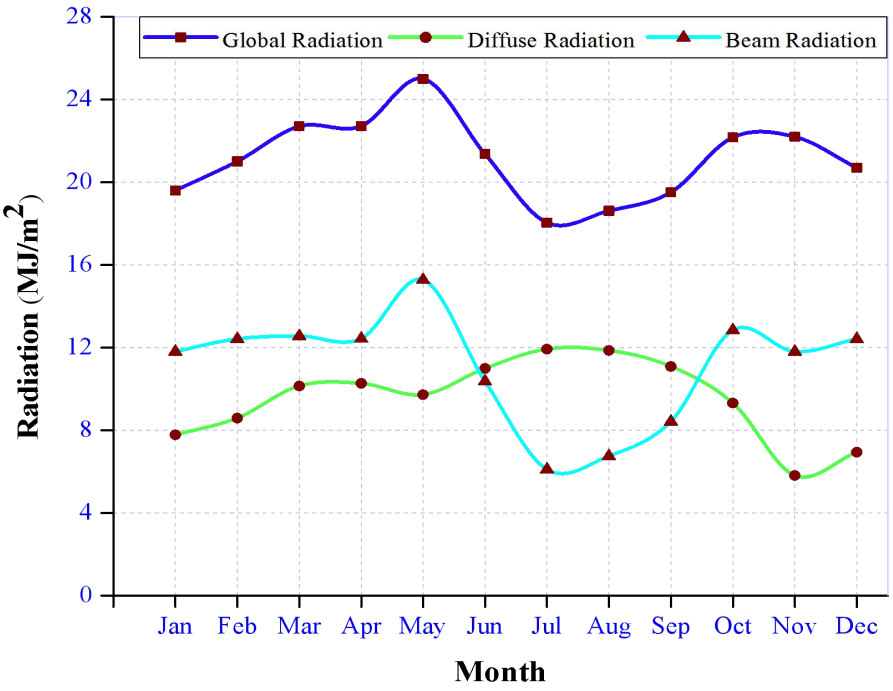

Figure 5.2: Monthly Averages of Daily Mean Global, Beam and Diffuse Radiation on the Horizontal Surface

Beam radiation is solar radiation on a surface that has passed through the atmosphere without being appreciably scattered. It has been estimated from the knowledge of monthly average daily solar radiation.

The figure illustrates the beam solar radiation versus time of the day for the selected irrigation season (December to May). As shown, the monthly average hourly beam solar radiation increases from sunrise to a maximum at midday solar before decreasing again until sunset. At noontime, the maximum beam solar radiation reaches 605.34 W/m^2 in May and a minimum of 502.23 W/m^2 in January. In May, the system provides maximum power that allows the Stirling pump to supply the high demand for water for the irrigation system than other months.

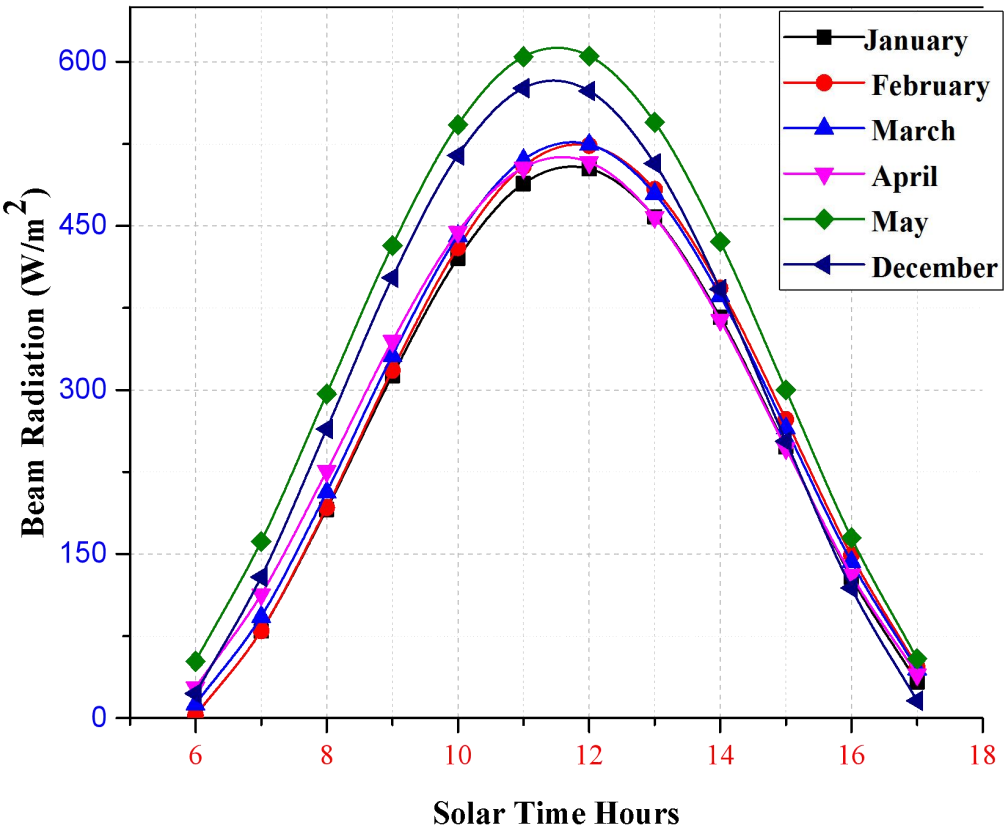

Figure 5.3: Estimated Monthly Average Hourly Beam Solar Radiation on a Horizontal Surface for the Irrigation Season

The concentrator should have to follow the sun's path to capture the available solar radiation falling. The incident angle is one of the vital parameters that affect the concentrator's tracking system and solar energy reaching on the concentrator.

It is an angle between the sun rays and the normal on the surface. Figure (5.4) shows the variation of beam solar radiation's incidence angle with solar time during a sunny day.

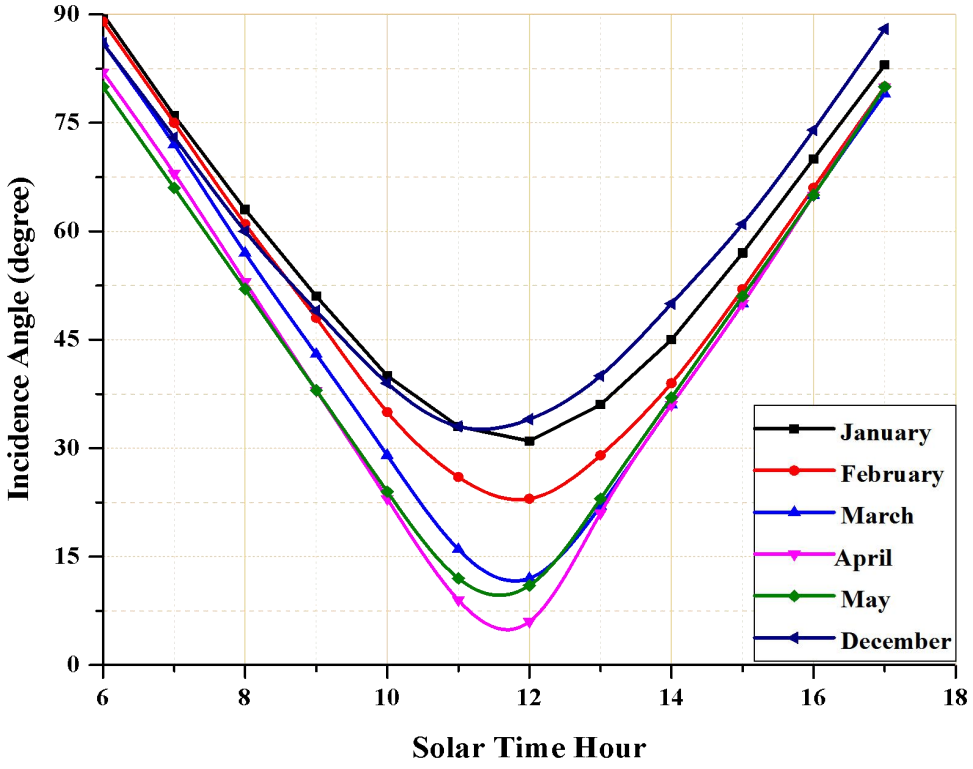

Figure 5.4: Variation of Incidence Angle of beam solar radiation with Solar Time from 6 AM to 6 PM during Irrigation Season (From December to May)

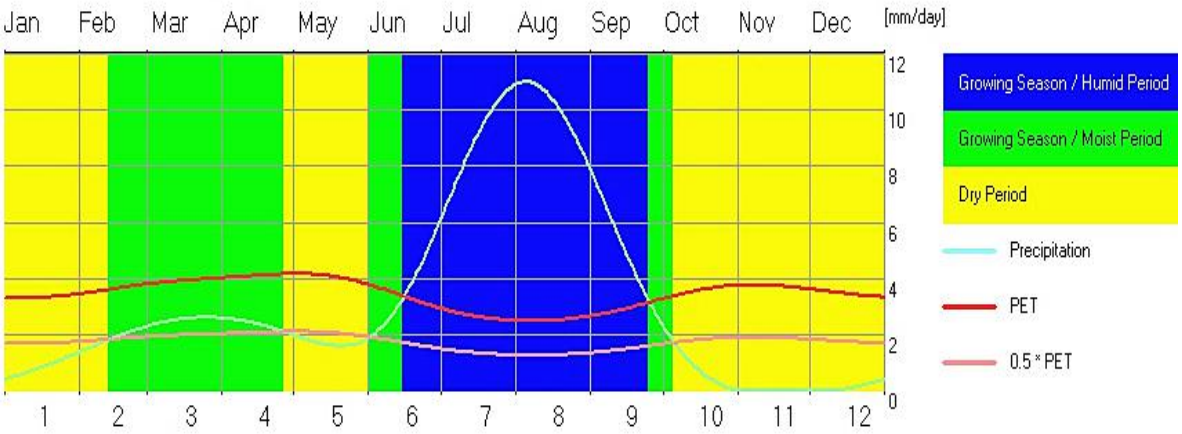

Figure 5.5: Local Growing Season Relative to Actual Precipitation and Potential Evapotranspiration

The bar chart given below illustrates the comparison of precipitation and PET of the site throughout a year. As can be seen apparently from the bar chart, there is a difference in both rainfall and PET statistic among twelve months. Specifically, in the dry season and wet season during irrigation, there are low precipitations and high evapotranspiration, as illustrated in figure (5.5) and (5.6). The higher evapotranspiration means the crop water requirement is more. However, there is a significant increase in rainfall level from 81 mm from June to a record high of about 332 mm in August. The bar chart also mentions that the region has suitable for irrigation systems in October, November, December, January, and May. As shown, the actual precipitation is less than the potential evapotranspiration.

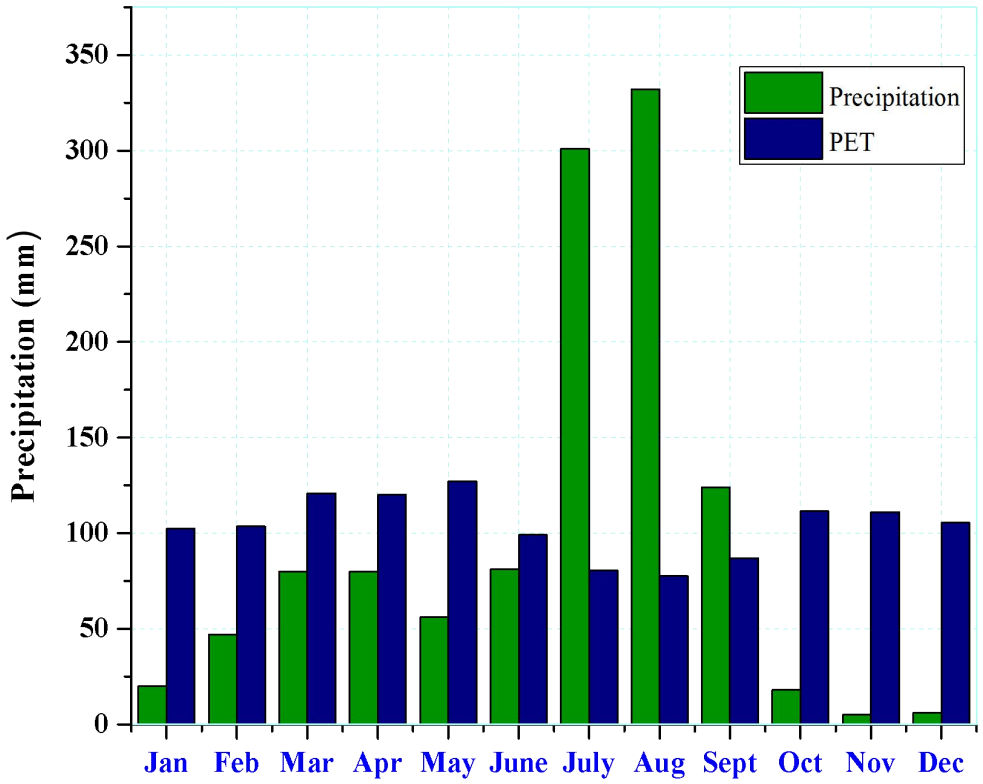

Figure 5.6: Variation of Average Monthly Precipitation and Potential Evapotranspiration (PET) Throughout a Year

The figure presents the comparison between solar radiation analyzing software and the estimated solar data using Newloc-Clim software. The estimated average beam solar radiation of the selected site using Newloc-Clim is found to be 5.86 KWh/m^2/day. The average minimum and maximum solar radiations are found to be 5.11 and 6.08 KWh/m^2/day for SWERA and RETScreen, respectively. In another case, for NASA surface-based and Meteonorm, it is found to be 5.58 and 5.46 KWh/m^2/day, respectively. The estimated direct solar irradiance by sunshine hour model is 3.6% lower than that of RETScreen, but 4.77% higher than PDA (NASA). The result shows a good agreement with those data reported in RETScreen and Potential data access software (NASA).

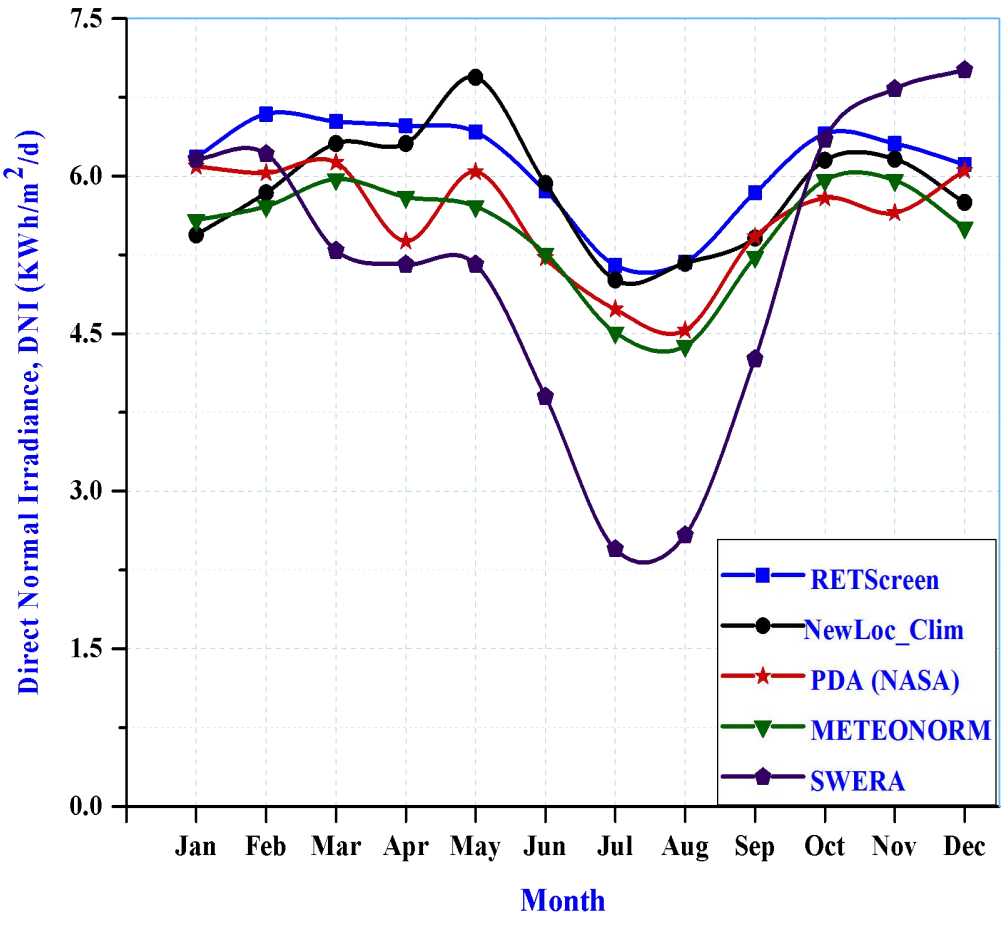

Figure 5.7: Comparison of Monthly Solar Radiation from Horizontal Surface, DNI with Solar Data Analysis Software

5.2 Performance Analysis of Dish Concentrator

Beam solar radiation is considered as a significant parameter to affect the performance of concentrated solar power. The amount of energy transferred to the working fluid in a receiver of the concentrator produces steam. Figure (5.8) illustrates the variation of beam solar radiation and outlet working fluid temperature with time of a day on May 15th. As can be shown, the beam solar radiation increases from sunrise to a maximum at noontime before decreasing again until sunset. Moreover, the curve shape is similar, proving the working fluid's outlet temperature increase linearly with the direct solar irradiance.

For the maximum beam solar radiation of 605.3 W/m^2, the maximum outlet fluid temperature reaches 410.7 K. Higher solar beam radiation results in higher outlet fluid temperature. As the thermal heat increases, TEG's power and the pump capacity to deliver water increases proportionally.

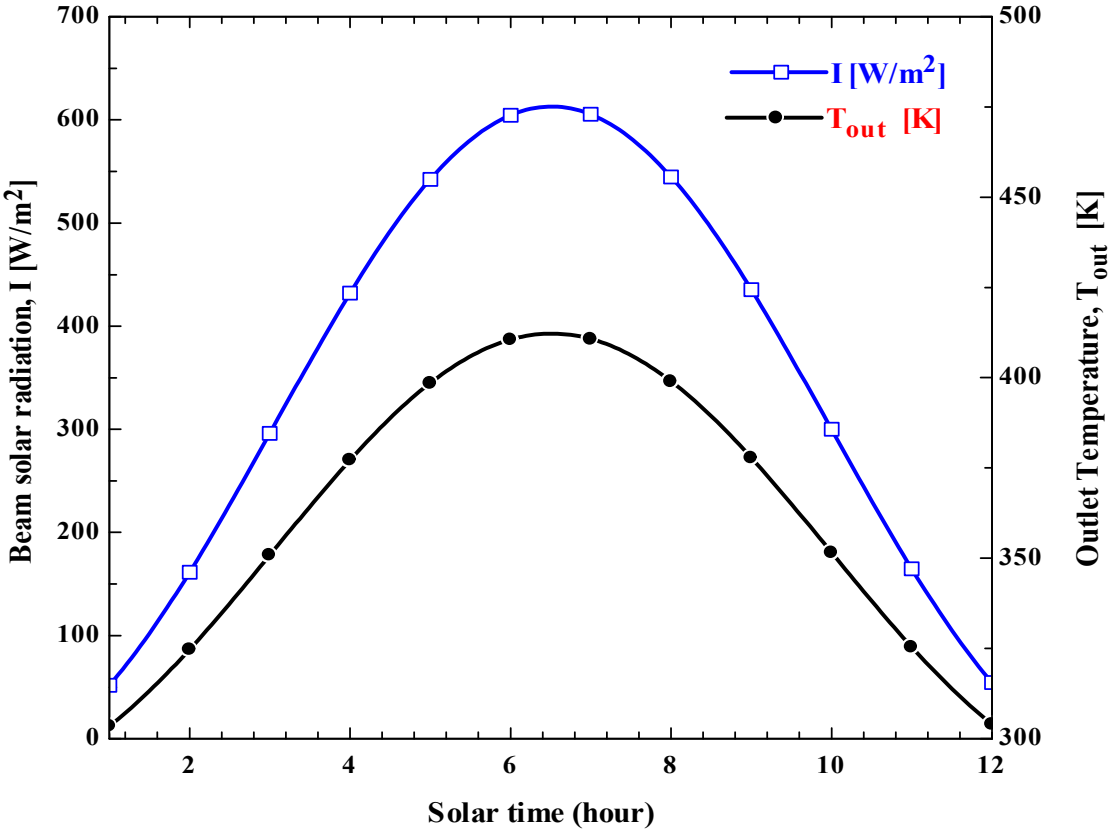

Figure 5.8: Variation of Beam Solar Radiation and Outlet Temperature of Working Fluid with Time on May 15th

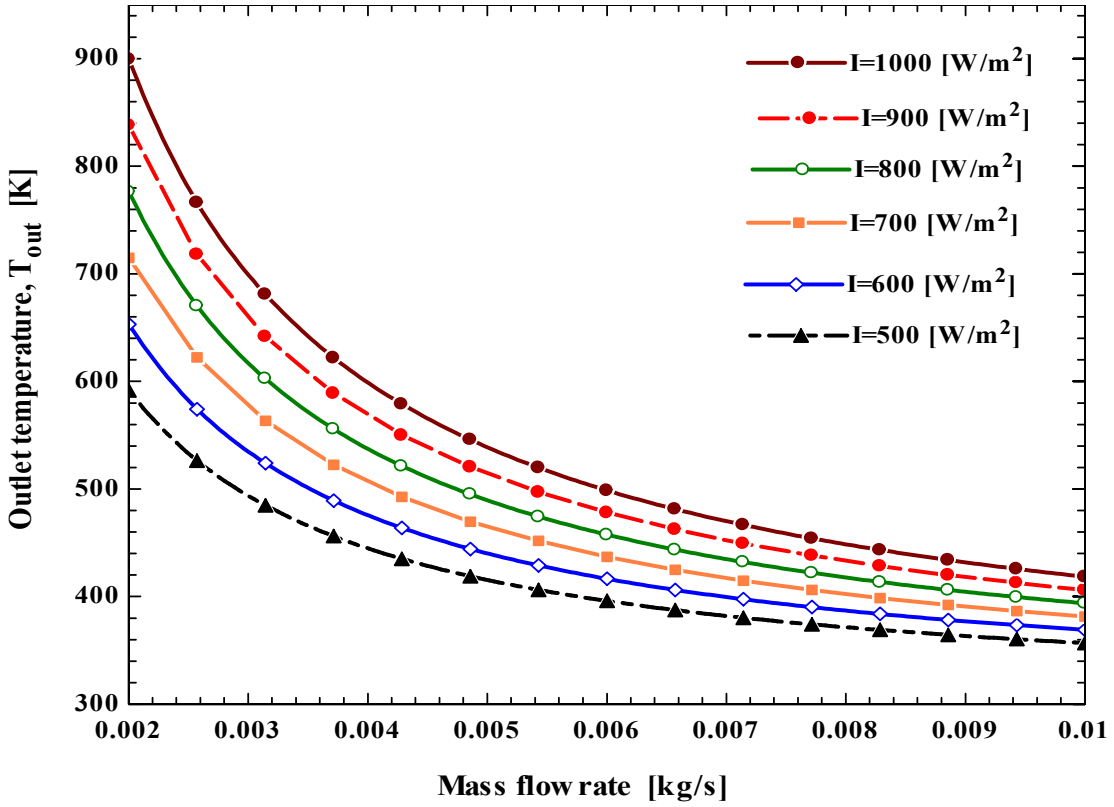

Figure 5.9: Effect of Working Fluid Mass Flow Rate on Temperature under Different Beam Solar Radiation

Figure (5.9) depicts the impact of mass flow rate on working fluid outlet temperature at different DNI and a constant ambient temperature of 288K. As shown, the outlet temperature is high for a given beam of solar radiation at the low mass flow rate. The outlet temperature slightly decreases as the mass flow rate of the fluid increases. For DNI of 1000 W/m^2 and 0.0065 kg/s mass flow rate, the outlet fluid temperature is 481.2 K.

The variation of working fluid outlet temperature during the sunny day for the given irrigation season is given in figure (5.10). As can be shown, the outlet fluid temperature increase from sunrise to mid-day and slightly decrease until sunset due to the variation of beam solar radiation. The temperature also varies for the selected irrigation period, and the maximum and minimum temperature achieved in May and January with 413.8 K and 394.2 K, respectively, at noontime.

The maximum outlet working fluid temperature estimated during February, March, April, and December is 398.2 K, 399.3 K, 395.3 K, and 408.1 K, respectively.

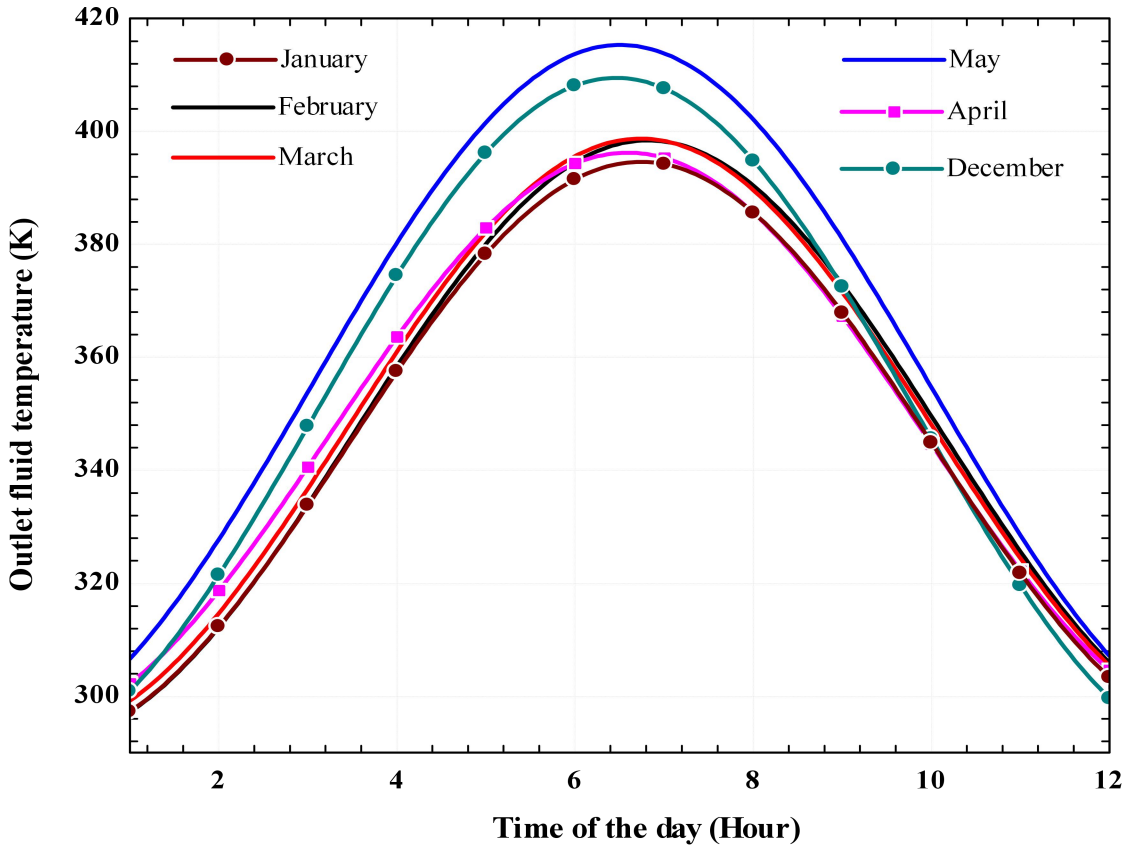

Figure 5.10: Variation of outlet fluid temperature with a time during the day for the selected irrigation season

Table 5.1: Analytical result of a dish concentrator

Parameters	Result	Unit
The outlet temperature of working fluid	488.2	K
Amount of heat received by a receiver of the concentrator	5156	W
Total heat loss	124.6	W
Useful heat	5032	W
The thermal efficiency of the concentrator	81.74	%

The table summarizes an analytical result of a parabolic dish solar concentrator for 1000 W/m^2 of solar beam radiation. The amount of heat absorbed by the receiver of the concentrator is 5156 W, and the outlet temperature of the working fluid reaches 488.2 K.

It can be seen from the table that the useful heat and thermal performance of the concentrator are 5032 W and 81.74%, respectively.

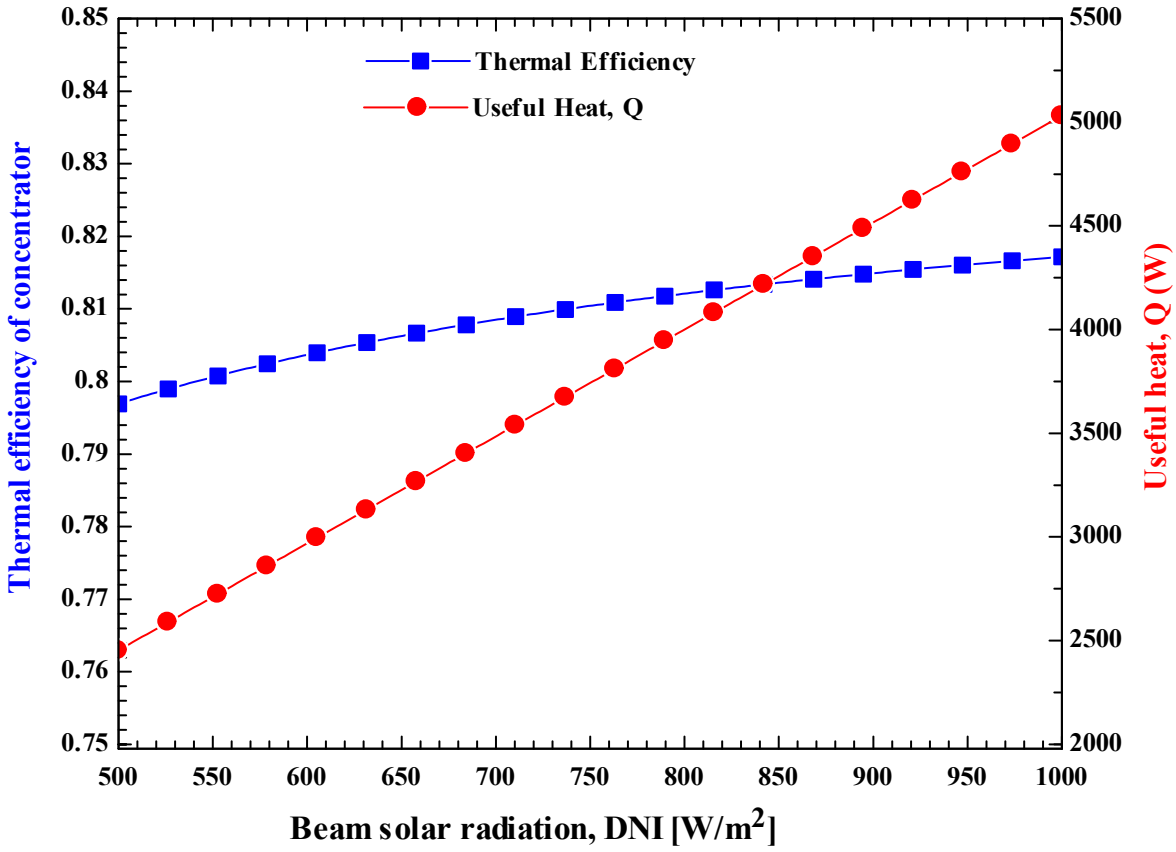

Figure 5.11: Effect of Beam Solar Radiation (DNI) on the useful heat and instantaneous thermal efficiency of the concentrator

The dish solar concentrator's performance depends on solar radiation's intensity, the working fluid's mass flow rate, ambient temperature, and receiver geometry.

Figure (5.11) depicts the variation of the concentrator's useful thermal heat and thermal efficiency with beam solar radiation. Useful thermal heat is the difference between the receiver's absorbed energy and heat losses from the receiver's surface. It depends on receiver surface temperature, solar irradiation, and wind velocity. As shown, the useful heat in the receiver of the concentrator increase with increasing solar irradiation. By varying solar irradiation from 500 to 1000 W/m^2, the useful thermal heat increase from 2454 to 5032 W. In another case, the figure exhibits the impact of solar irradiation on thermal performance. Higher DNI leads to higher thermal performance. It is noticed that the concentrator's thermal efficiency increases by 2.03 % as the solar beam radiation varies from 500 to1000 W/m^2.

5.2.1 Effect solar radiation on flux intensity at the absorber of the concentrator

The solar flux distribution at the receiver's focal plane was simulated using the SolTrace, based on the Monte Carlo ray-tracing method. Figure (5.12) indicates the ray intersection of a hundred beam solar with the concentrator's absorber. The optical analysis is performed for 10,000 rays. Based on simulation results from all emitted rays, 9165 reach the receiver surface, which is 91.65 % of the beam emitted. The amount of ray goes to the absorber depends upon the concentrator's optical properties like reflectivity and optical errors. The power per ray is 0.613 W, and the total power of the plot ray is 5612 W.

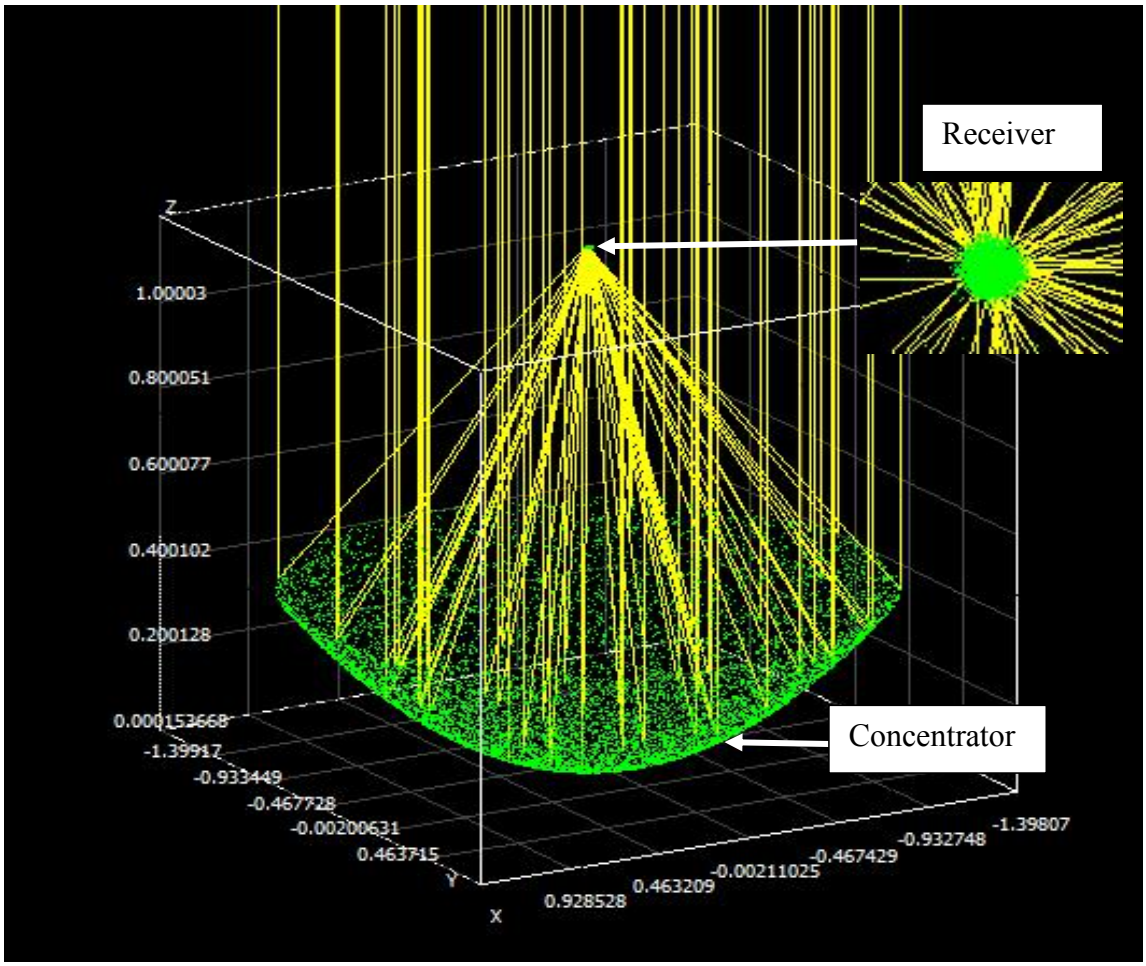

Figure 5.12: Ray intersection (scatter) plot on the concentrator and absorber

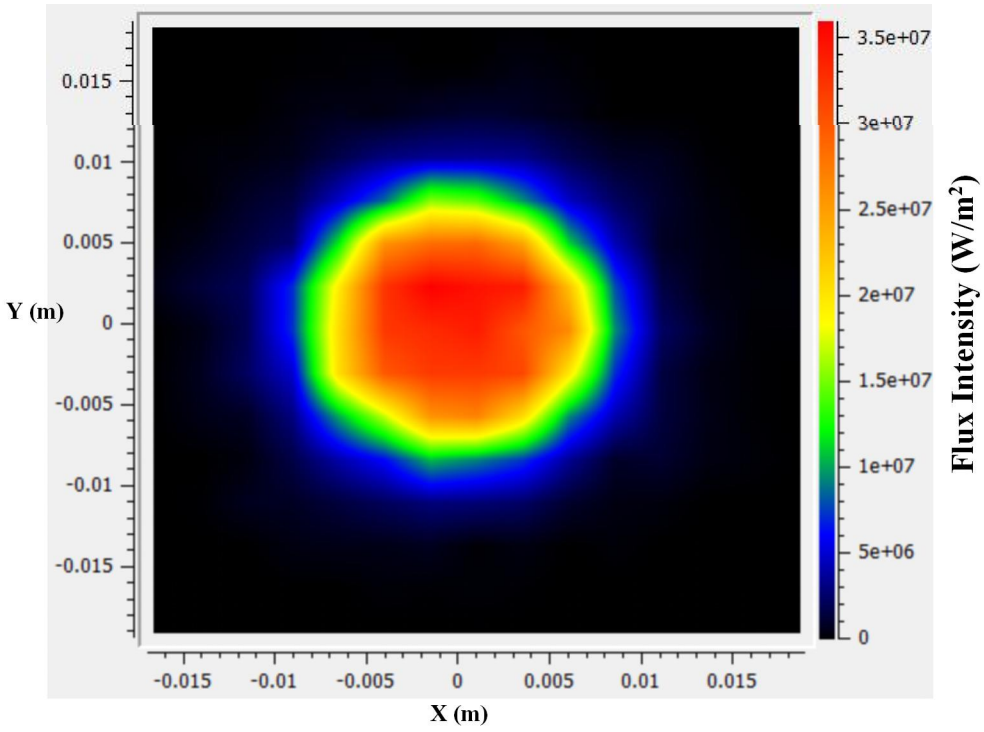

Figure 5.13: Contour plot (Two dimensional view) of flux distribution at the focal plane

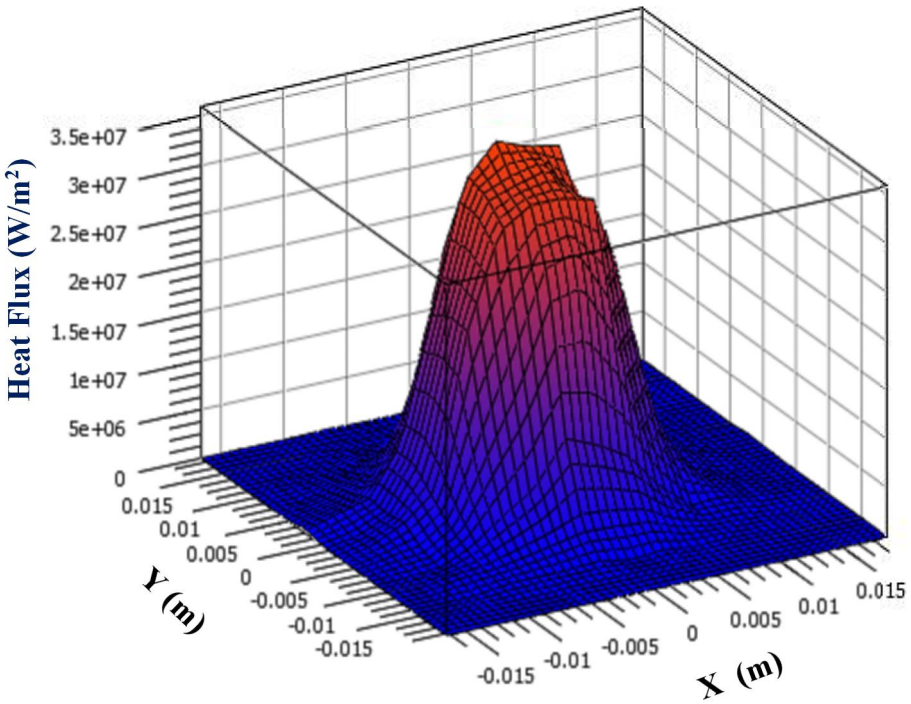

Figure 5.14: Surface plot or 3- dimensional view of flux distribution on the receiver

Figure (5.13) and (5.14) shows the contour and surface plot flux intensity at the focal plane of the concentrator for the DNI of 1000 W/m^2. The flux profile is generated using SolTrace software at the receiver of the concentrator by setting the optical and stage properties. The peak flux predicted at receiver is found to be 3514 KW/m^2 with an uncertainty of +/- 5.76 % or 202.4 KW/m^2 deviation. Furthermore, the average heat flux intensity at the concentrator's absorber reaches around 4750 KW/m^2.

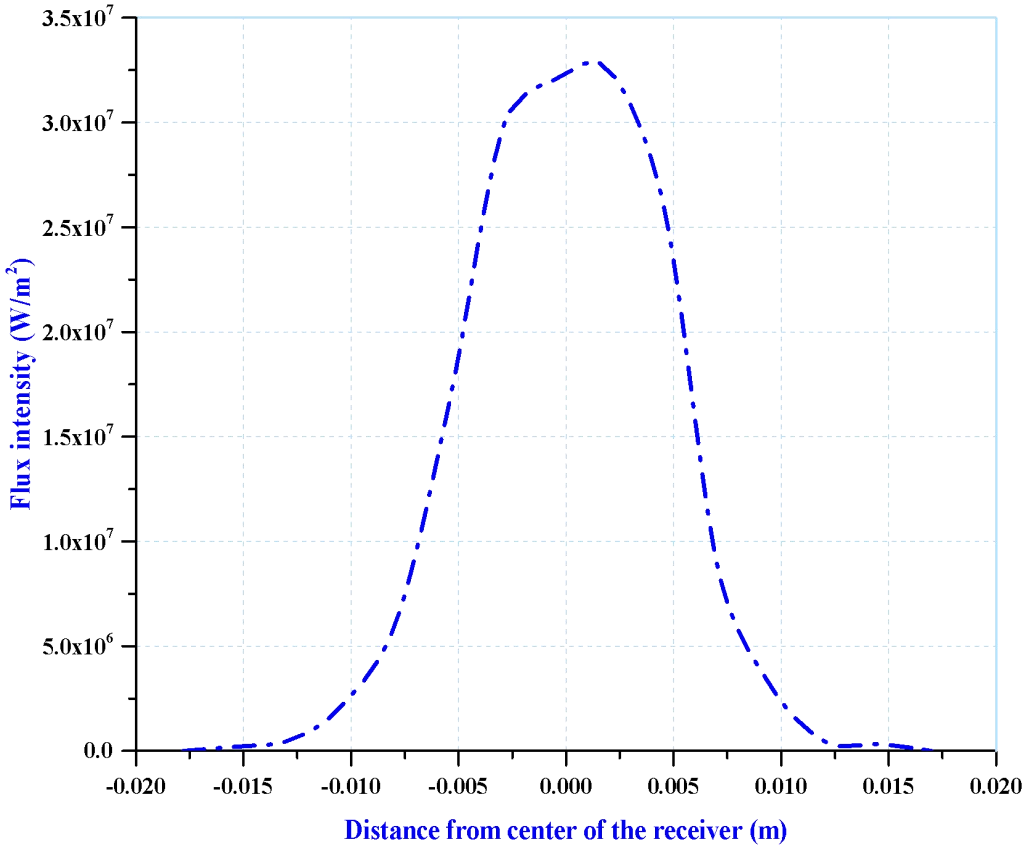

Figure 5.15: Variation of Heat Flux Distribution at Absorber

Figure (5.15) illustrates the variation of flux intensity distribution at the absorber of the concentrator. Since dish concentrator is point focus, all the incoming sun rays are reflected on the absorber. It is visible that the heat flux is high at the absorber center and slightly decreases to the absorber's outside direction.

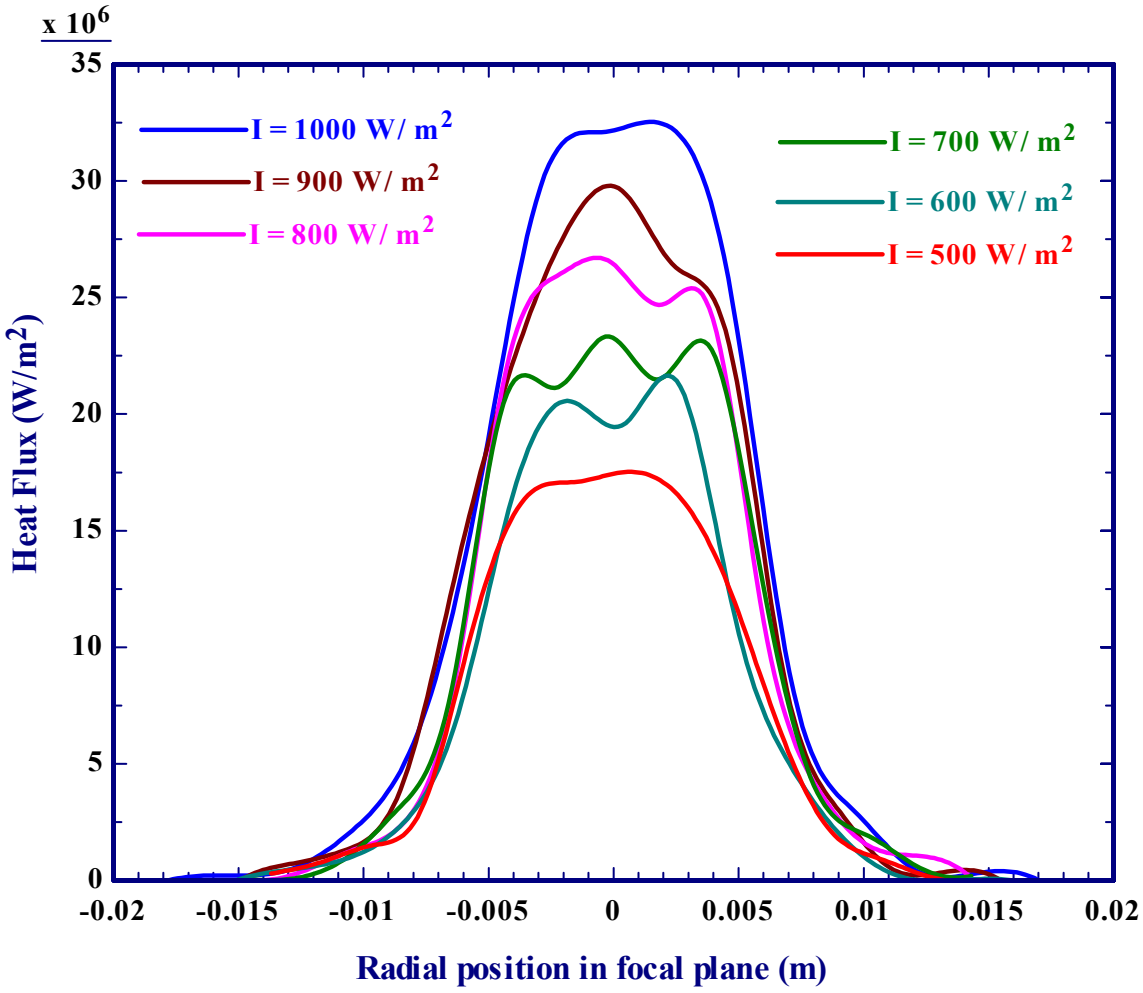

Figure 5.16: Effect of beam solar radiation on flux intensity

Figure (5.16) depicts solar beam radiation's impact on the heat flux distribution at the concentrator's absorber. As shown, the flux distribution at the absorber's focal plane increases toward the center with increasing solar irradiation. For the same optical properties of the concentrator and varying DNI from 500 to 1000 W/m^2 with an increment of 100 W/m^2, flux intensity rises from 17.5 to 32.4 MW/m^2.

5.2.2 Effect of solar heat flux on temperature distribution at the focal plane

The temperature distribution analysis at the concentrator receiver was done through COMSOL Multiphysics V5.5 [48]. The simulation is performed using the heat transfer module package in the software. The heat flux and ambient temperature are used as a boundary condition. According to the simulation results, for the average heat flux of 4.75*106 W/m^2, a maximum temperature of 923K reaches the absorber center. As shown in figure the temperature distribution is slightly decreased along with the radial position from the center to the absorber's edge.

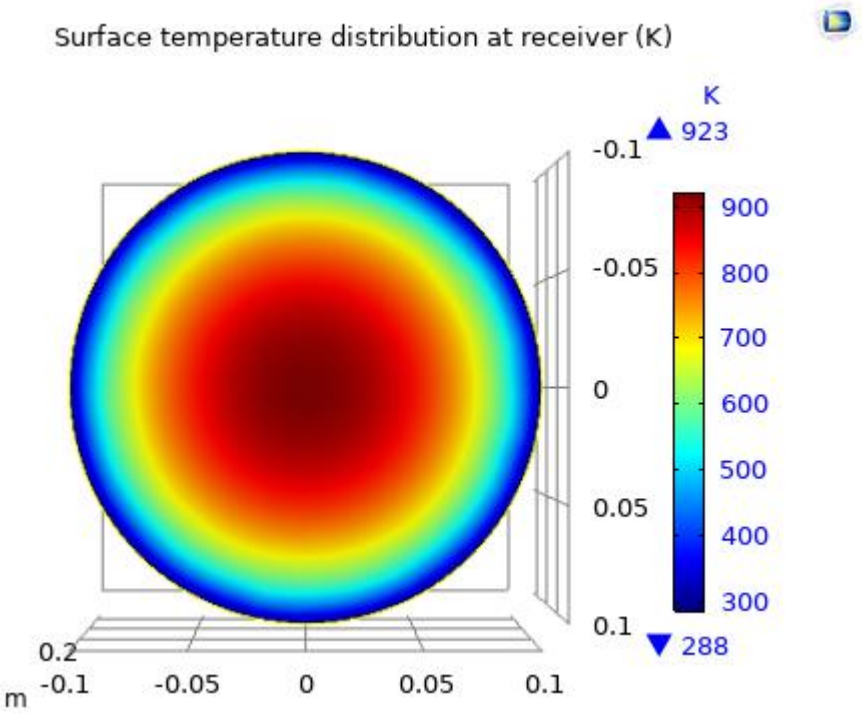

Figure 5.17: Temperature distribution at the receiver of the concentrator

Figure (5.17) illustrates the variation of temperature distribution at the focal plane of the absorber. It is visible that the heat flux is high at the absorber center and slightly decreases toward the absorber edge. For 1000 W/m^2 of beam solar radiation, the temperature at the center of the receiver reaches 923 K and 288.9 K at the absorber edge. Figure (5.19) shows the impact of solar irradiation on the absorber focal plane's temperature distribution. Higher solar irradiation means higher temperature distribution at the receiver focal plane. By varying the beam solar radiation from 500 to 1000 W/m^2, the receiver's center's temperature increases from 606 to 923 K.

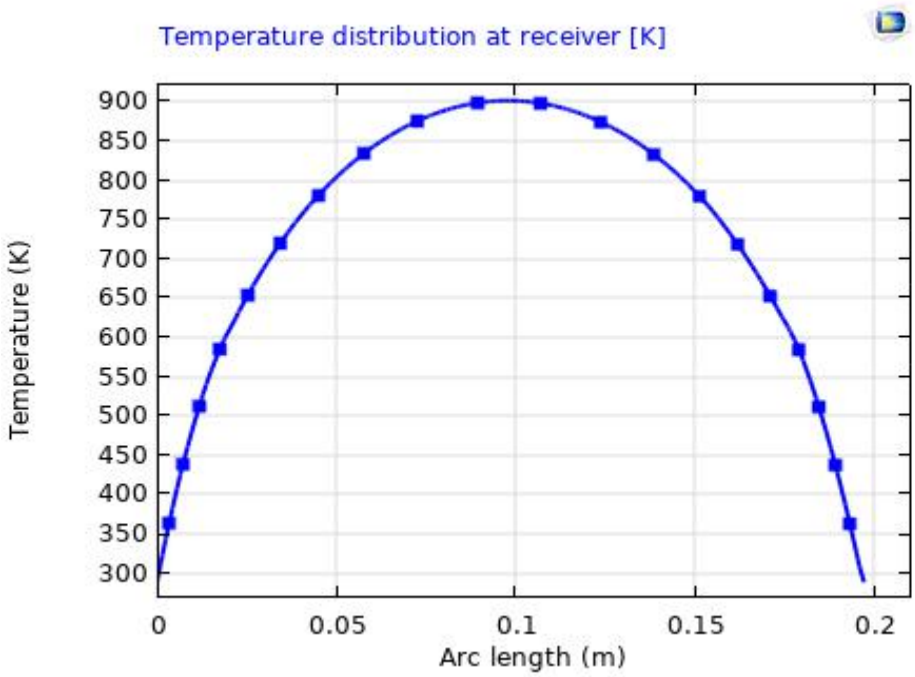

Figure 5.18: Variation of temperature distribution with arch length focal plane

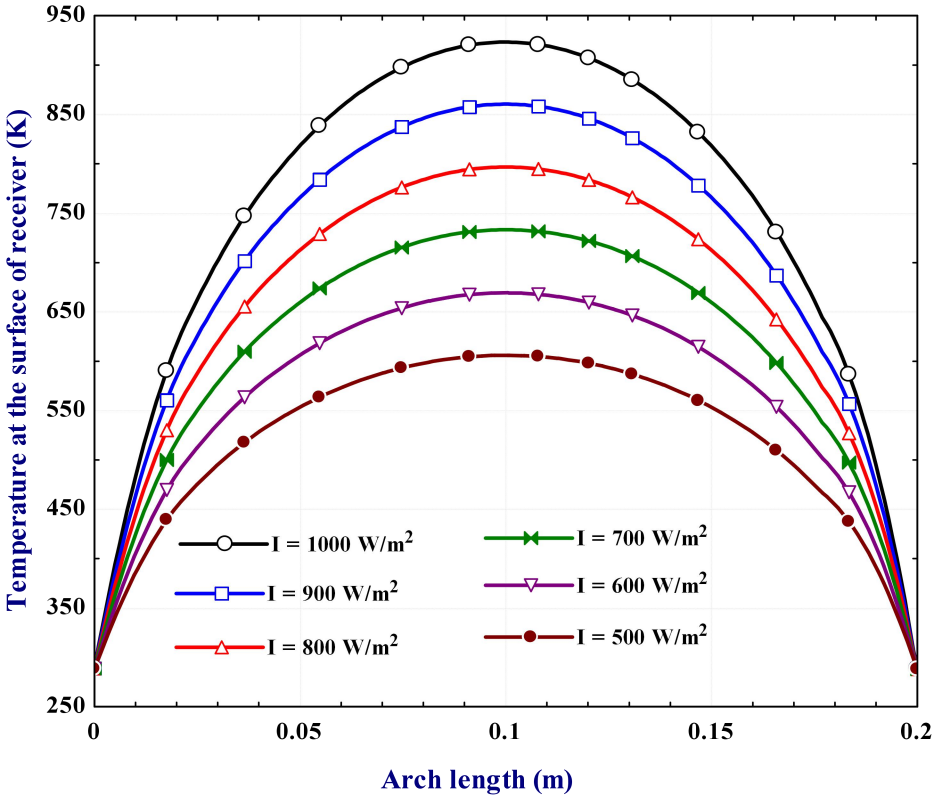

Figure 5.19: Effect of incoming solar radiation (beam solar radiation) variation on temperature distribution at the surface of the receiver

5.3 Multiphysics simulation of Thermoelectric Generator

Multiphysics analysis of a Thermoelectric Generator is performed using COMSOL 5.5 [48]. The numerical problem is solved by physics interface using a combination of heat transfer with thermoelectric effect at temperature gradients of 165 K. COMSOL already defines the governing equations used for TEG simulation. Steady-state is considered in a physics interface by combining the Fourier law of heat conduction, ohms law, and Peltier- Seebeck-Thomson effects.

5.3.1 Boundary Condition

- P-N thermocouple is connected electrically in series and thermally in parallel
- The bottom side substrate is defined as a TEG heat source with a temperature of 488.15 K, while the top side substrate is kept as a cold surface and heat sink temperature of 298.15 K.
- The electrode in one side of the thermocouple leg is set as ground, while the other side is maintained as terminal.
- Natural convection air cooling system is used in the heat sink to dissipate heat from TEG cold side.
- All material properties are taken from the COMSOL Multiphysics library.

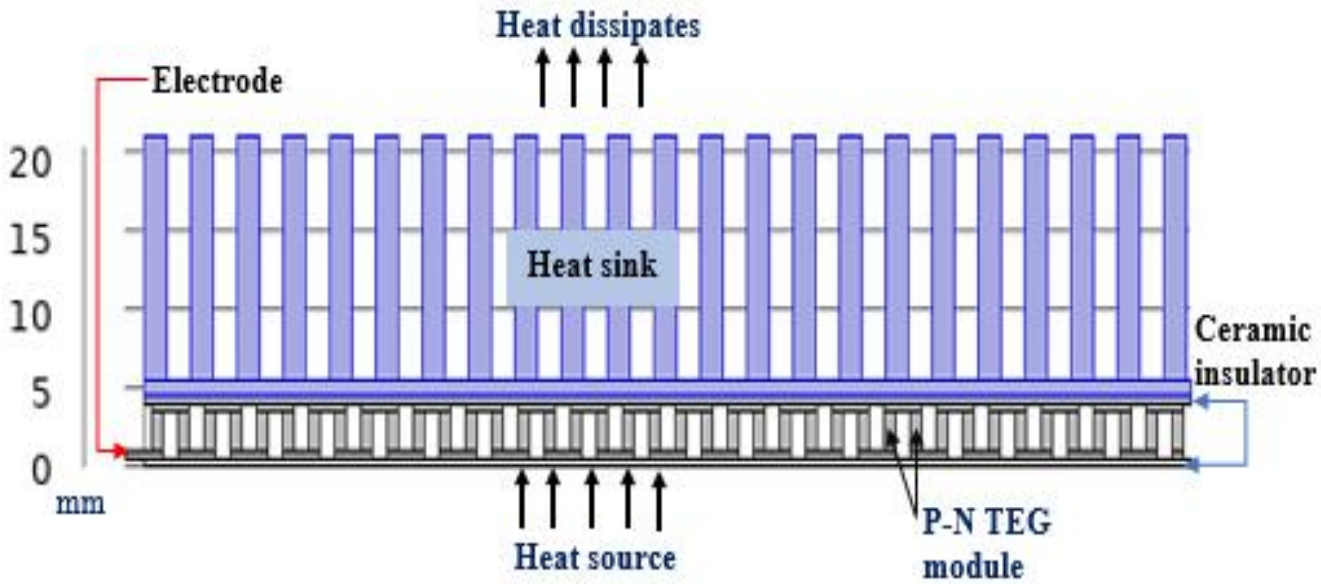

Figure 5.20: Schematic diagram of boundary condition for TEG simulation

5.3.2 Define Material Properties

Thermoelectric material is defined by three properties like the Seebeck coefficient, electrical resistance, and thermal conductivity. Thermoelectric properties TEG, copper electrode, and alumina substrate are available in the COMSOL Multiphysics materials library and user-defined. Four commercials Bi_2Te_3 TEG module is considered for the simulation, and the material properties are summarized below in table (5.3).

Table 5.2: Thermoelectric properties of Bi_2Te_3 module, copper electrode, and alumina substrate

Properties	**TEG material (Bi_2Te_3)**	**Electrode: Copper**	**Substrate: Alumina**	**Unit**
Density	7740	8920	3900	Kg/m^3
Thermal conductivity	1.793	400	27	W/ mK
Specific heat capacity @ constant pressure	154	385	900	J/kg.K
Seebeck coefficient	P:$2.367*10^{-4}$ N:$2.36*10^{-4}$	N/A	N/A	V/K
Electrical conductivity	$5.724*10^4$	$5.9*10^7$	-	S/m
Relative permeability	1	1	-	-

5.3.3 Simulation results

Seebeck coefficient is a temperature-dependent thermoelectric property that affects the goodness factor and conversion efficiency of a thermoelectric generator. Seebeck coefficient is positive for P-type and negative for N-type of thermoelectric legs. As shown in figure (5.21), the Seebeck coefficient is $2.37*10^{-4}$ V/K for P-type and $-2.37*10^{-4}$ V/K for N-type. The result was extracted from COMSOL for an absolute temperature of 405.6 K.

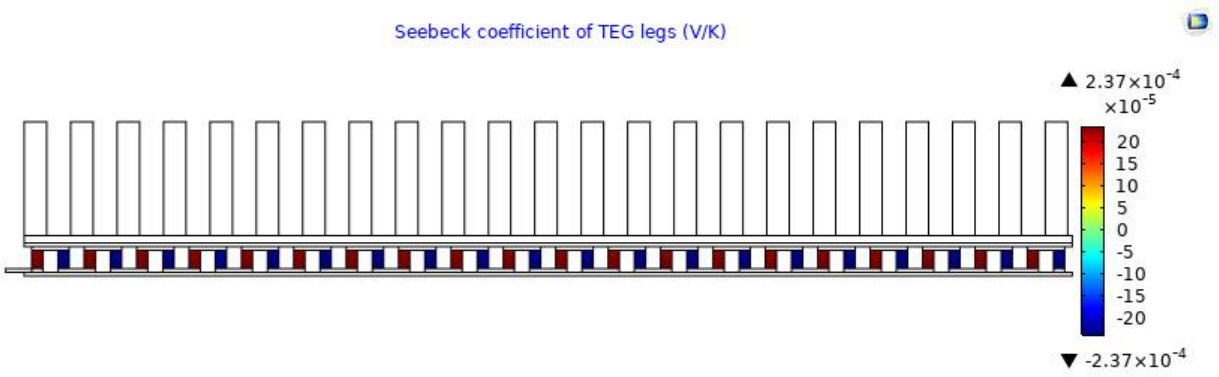

Figure 5.21: Seebeck coefficient of the TEG module

The Multiphysics simulation is performed using finite element methods for 400 legs of commercial TEG, connected electrically in series and thermally in parallel. The P-N legs and module dimensions were given in the appendix (III). The cross-sectional (2D) and 3D contour plots of temperature distribution are shown in Figures (5.21) and (5.22), respectively. The temperature gradient across the module reaches 165 K, and 20.148 W of heat is dissipated from the module's cold side through the heat sink.

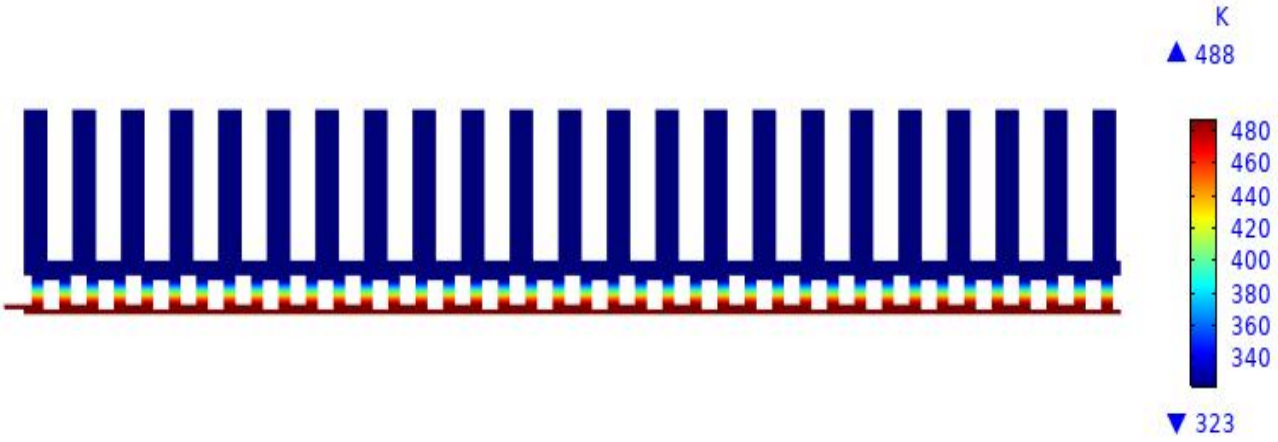

Figure 5.22: Schematic diagram for 2D surface temperature distribution in the thermoelectric module

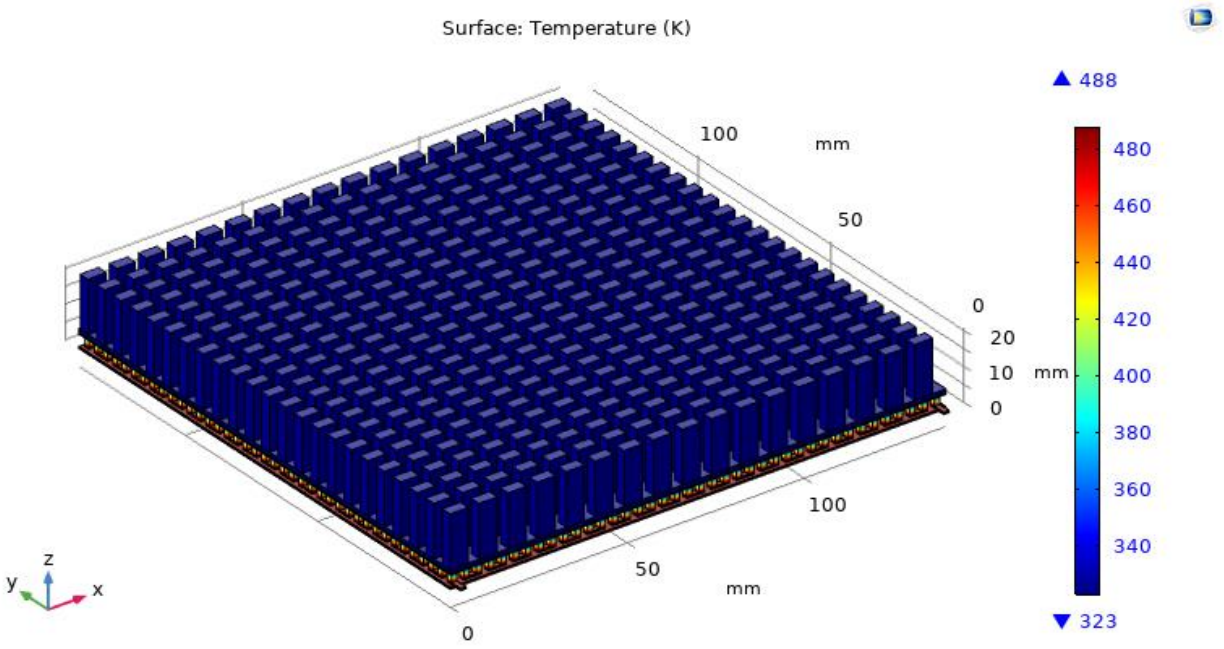

Figure 5.23: 3D surface temperature distribution across the TEG module

This figure demonstrates the contour plot of the average current density of the TEG module. The current density depends on the electrical conductivity of the material. Higher electrical conductivity shows a high current flow per unit area in the material. As can be seen, the current density increases from the thermoelectric leg's joint to the middle of the copper electrode. The maximum current density shows that more electron movies in the copper conductor's direction.

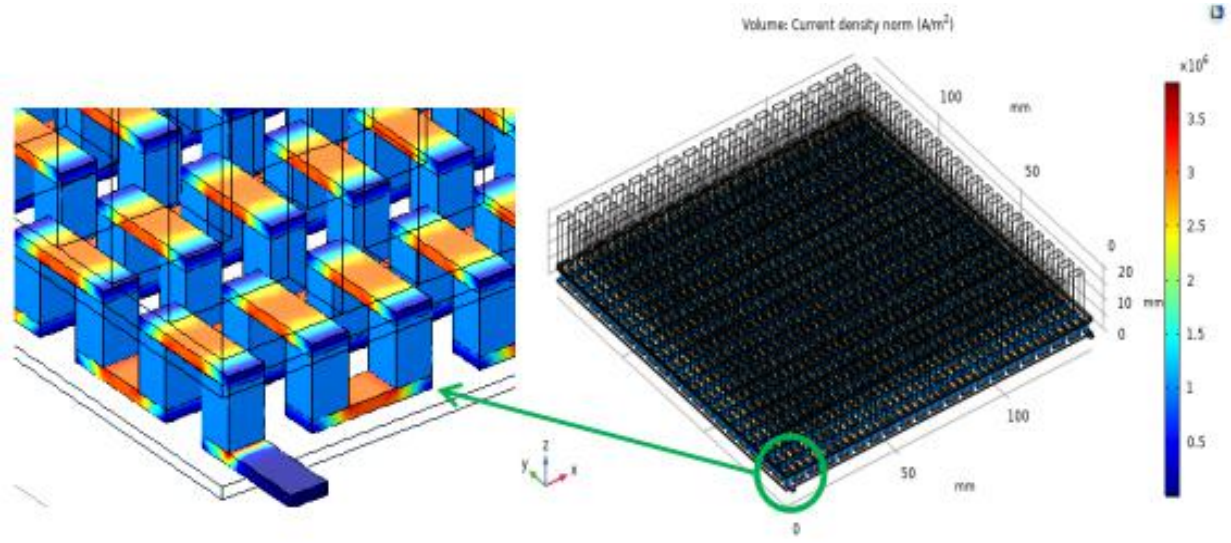

Figure 5.24: Variation of normal current density across the thermoelectric module

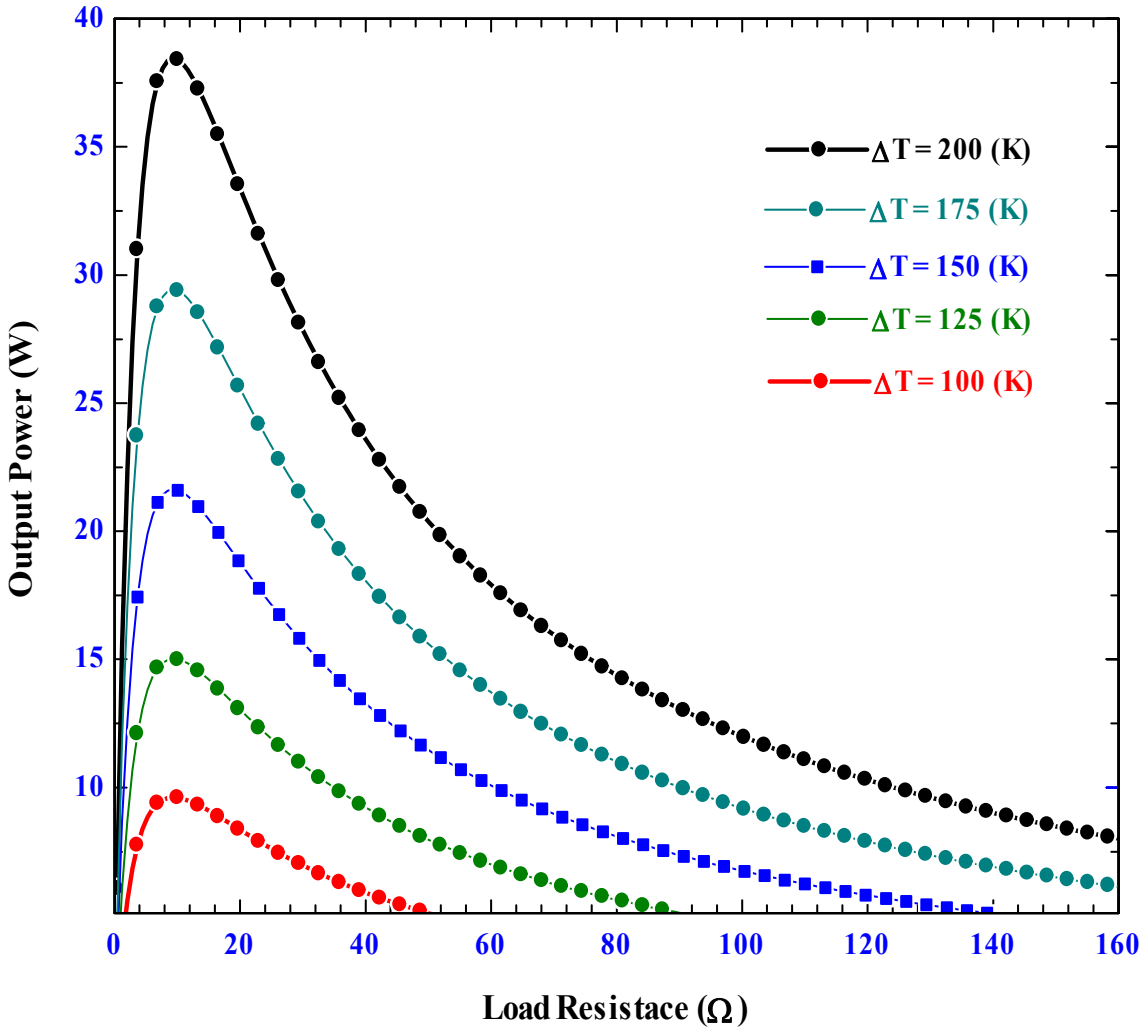

Figure 5.25: Effect of load resistance on the electrical power of TEG

Figure (5.25) shows the variation of output power as a function of external load resistance. By maintaining the cold side temperature and varying the temperature gradients, the output power is maximum when the external load resistance is equal to the internal load resistance. When the external load resistance is above the internal load resistance, the output power decreases, as shown above.

The voltage induced by TEG as a function of electric current is shown in figure (5.26). The matched load voltage decreases as the electric current increases and exhibits a linear relationship for each temperature gradient.

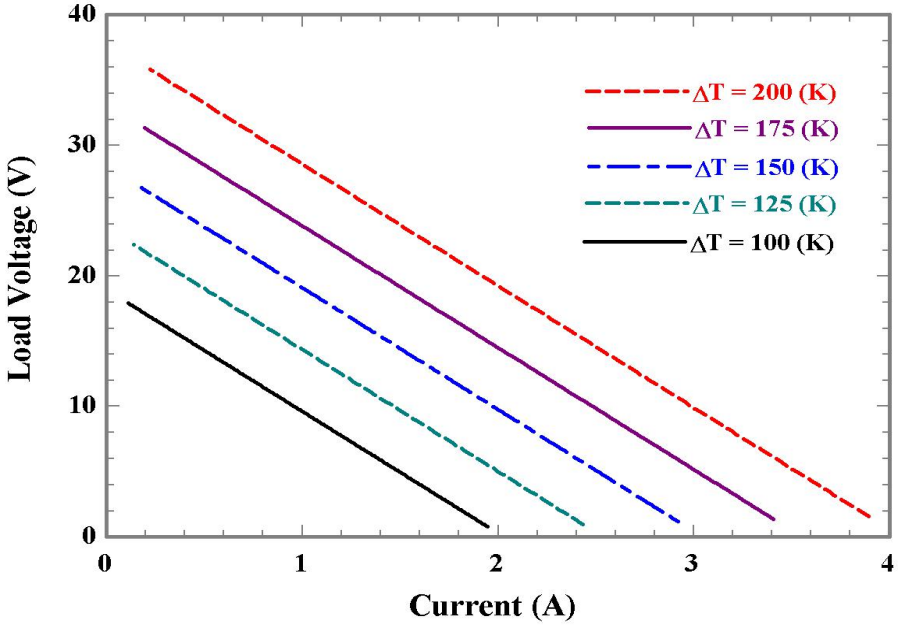

Figure 5.26: Variation of voltage with electric current for a given temperature gradient

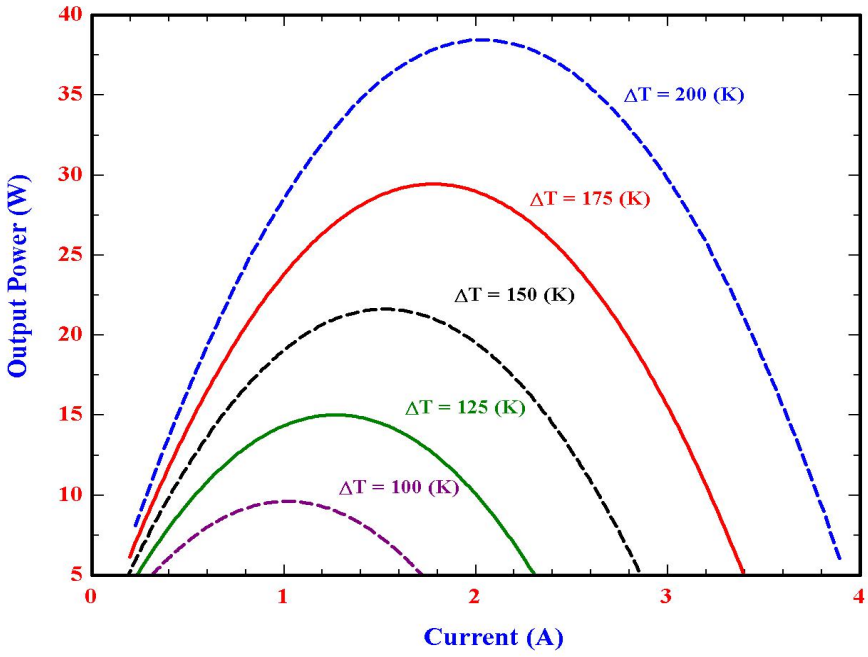

Figure 5.27: Influence of load current on the output power of TEG for a given temperature gradient

By fixing the cold side temperature at 323.15 K and varying the temperature gradient from 100 to 200 K with an increment of ΔT=25 K, TEG's output power as a function of electric current behaves like a parabola. It is visible that TEG's power is maximum at the optimum specific value of electric current. For the current below the optimum value, the power is increasing until it reaches optimum, while for the current above the optimum value, the output power generated by TEG decreases.

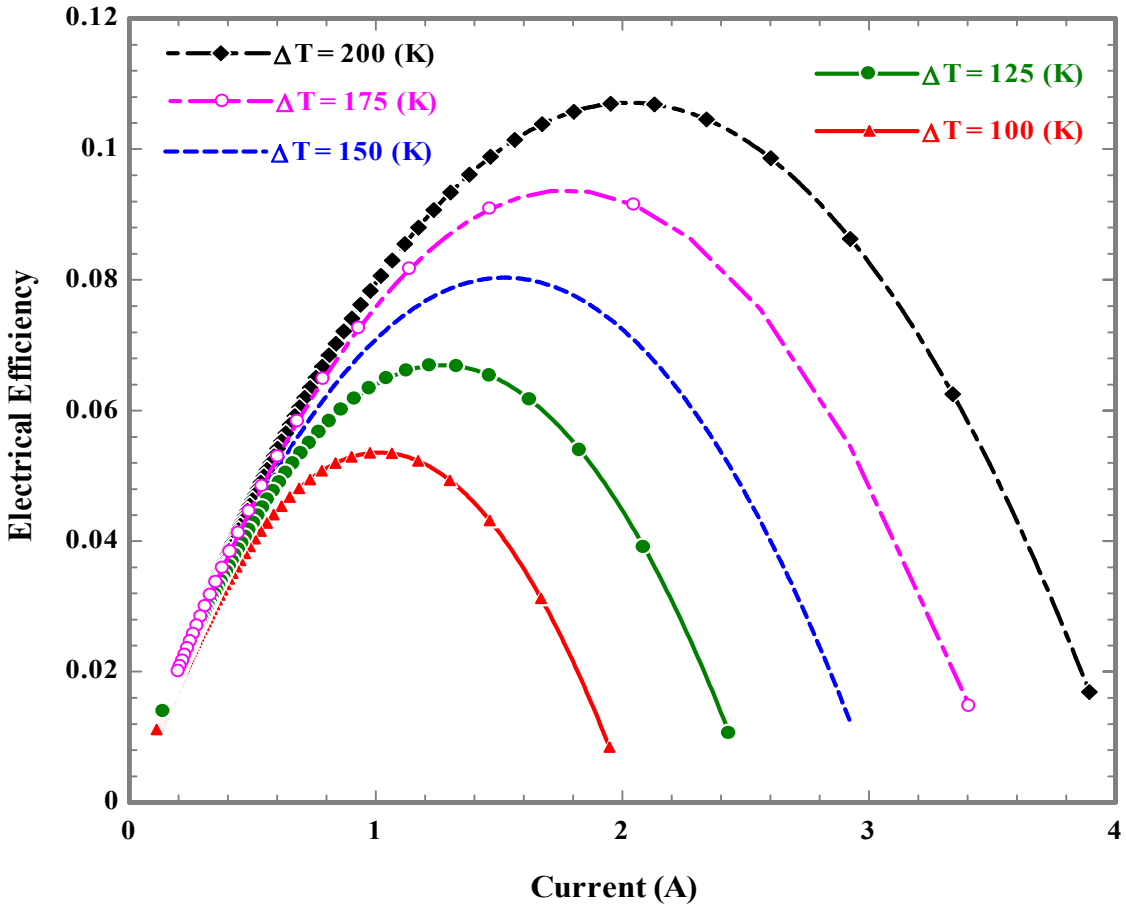

Figure 5.28: Electrical efficiency as a function of current at a different temperature gradient

Figure (5.28) shows the variation of electrical efficiency of TEG as a function of electric current. As can be seen, at constant cold side temperature of 323.15 K and varying the temperature gradient from 100 to 200 K with an increment of ΔT=25 K, TEG's electrical efficiency behaves as a parabola and it is optimum at a specific electric current. The electrical efficiency is maximum at the optimum current value for each temperature gradients.

Figure (5.29) also depicts the impact of heat source temperature on TEG's output power and electrical efficiency. As shown from the figure, the TEG module's power depends on the temperature difference between the module's hot and cold sides. By fixing the cold side temperature at 323.15 K, the TEG module's output power and electrical efficiency increase with increasing heat source temperature.

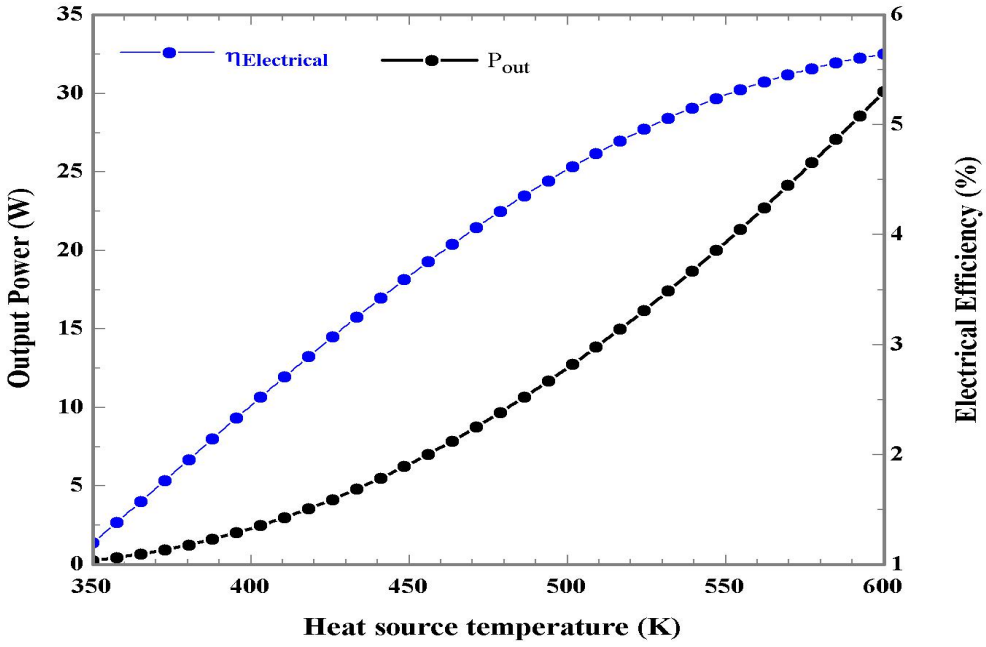

Figure 5.29: Effect of heat source temperature on output power and electrical efficiency of TEG at constant cold side temperature

Table 5.3: Electrical power and efficiency of TEG during the selected irrigation period

Months	Electrical efficiency(%)	Maximum Electrical power (W)	The cumulative power of TEG(W)
February	2.405	3.85	18.49
March	2.407	3.86	18.72
April	2.332	3.62	18.05
May	2.78	5.2	26.87
December	2.637	4.63	22.98
January	2.305	3.54	16.9

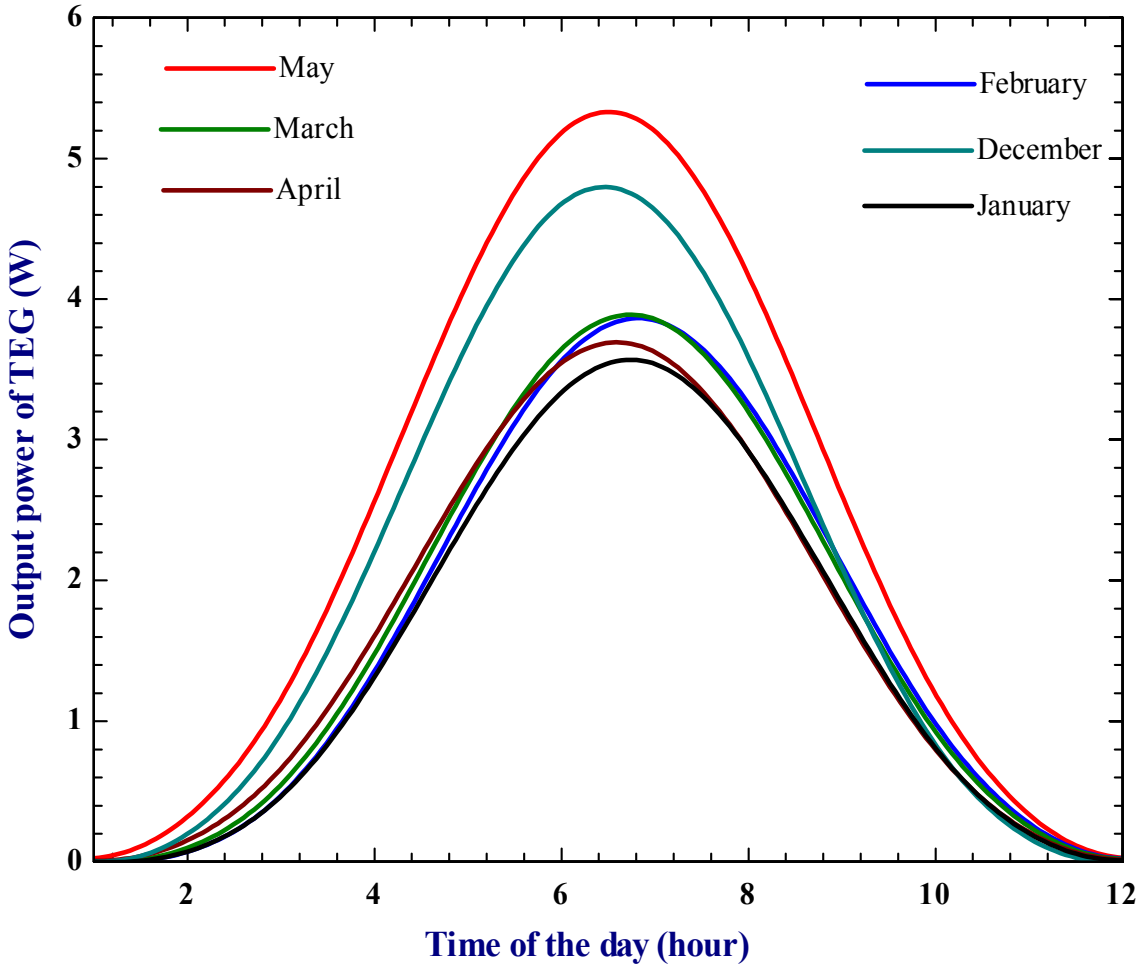

Figure 5.30: Change of TEG output power during the time of a day for the selected irrigation period

Heat source temperature mainly affects the output power and electrical efficiency of a thermoelectric generator. As shown in figure (5.30) and (5.31), both TEG output power and electrical efficiency are maximum at noontime and minimum during sunrise and sunsets. It is clearly seen that higher heat source temperature leads to higher electrical power and efficiency of TEG. In both cases, the output power and electrical efficiency are higher in May and minimum during January. The cumulative power generated by TEG during the sunny day is also given in table (5.4). The result shows that a maximum cumulative power of 26.87 W is generated in May with an electrical power of 5.2% during the day.

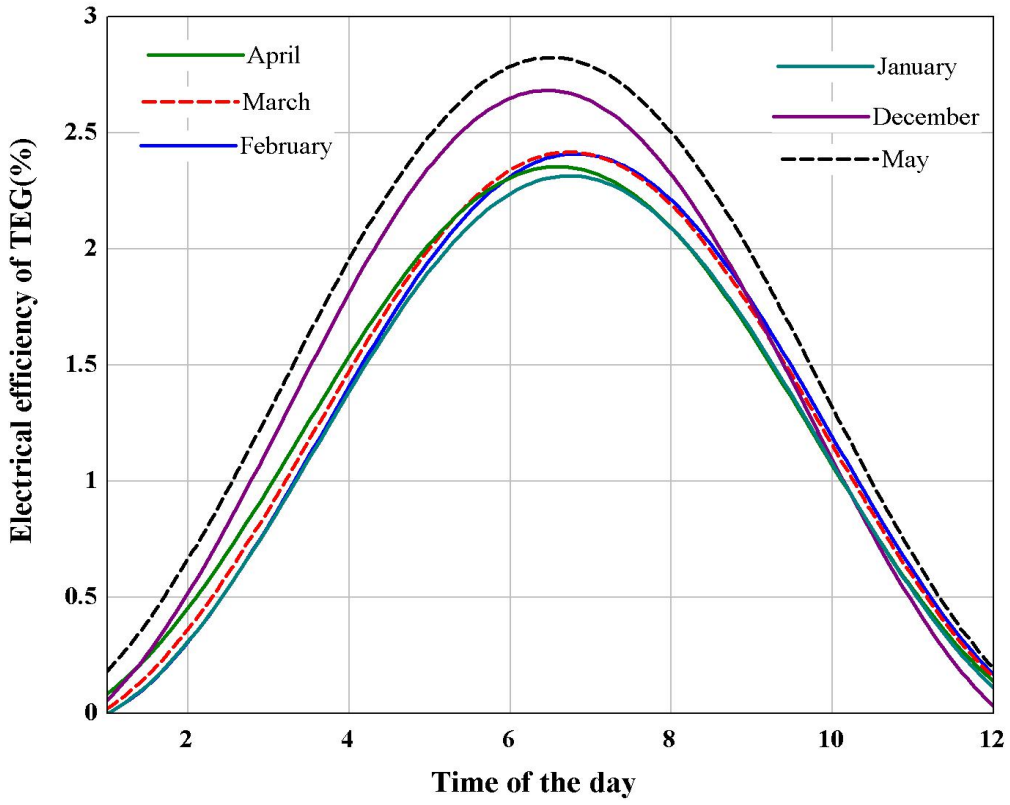

Figure 5.31: Change of TEG electrical efficiency during the time of the day for the selected irrigation period

TEG's maximum output power is 26.17W at the same value of the internal and external load resistance of 9.36. The maximum conversion efficiency depends on the temperature across the module and the ZT value of the material. It is found that the maximum possible conversion efficiency of the module is 5.366%. The power generated by TEG is stored in a battery for the usage of a dish tracking system, night–time pumping and micro-electrification.

5.4 Transient Performance Analysis of Beta Stirling Engine

5.4.1 Ideal adiabatic analysis

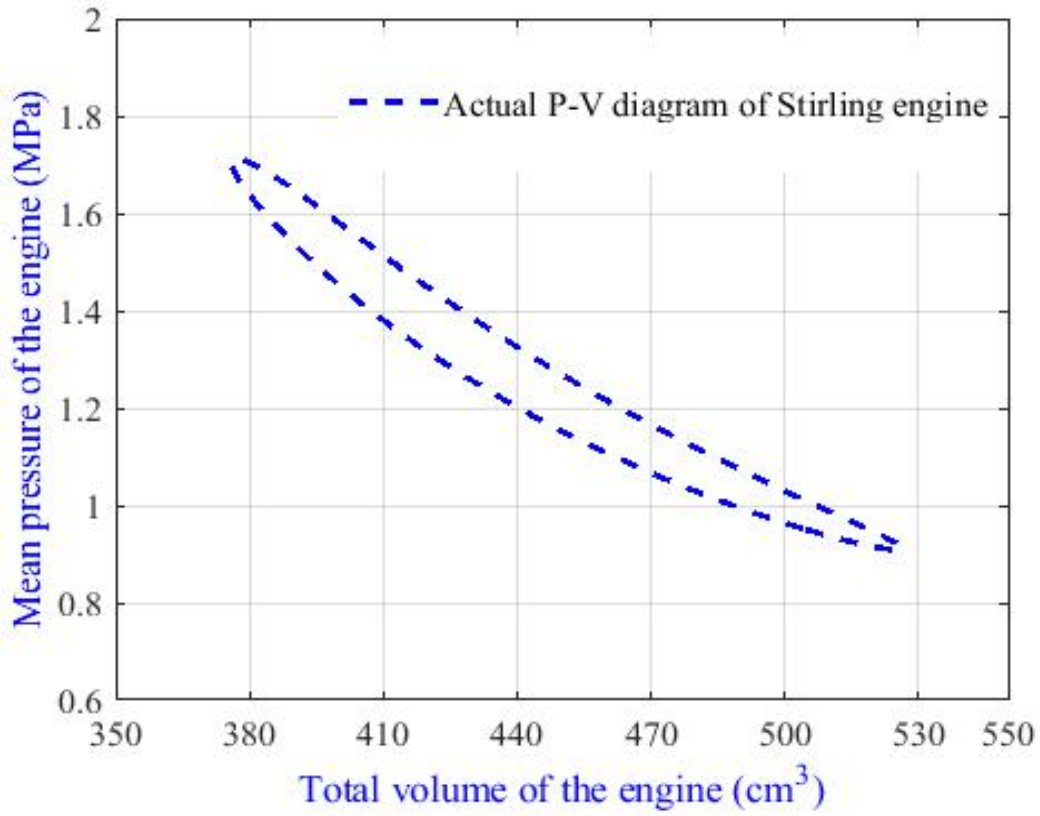

Figure 5.32: Simulated Actual P-V Diagram of ideal adiabatic analysis of Beta Stirling Engine

Figure (5.32) illustrates that the actual P-V diagram of the proposed Stirling pump model. The graph shows the relationship between the operating pressure and the working fluid volume of the working space as a crank angle function. The diagram's enclosed area represents the work done by an engine, where positive work-done is in expansion space and negative work done in compression space. The engine's maximum and minimum volume is 525 cm^3 and 375.16 cm^3, respectively, with a compression ratio of 1.4 and a pressure ratio of 1.71.

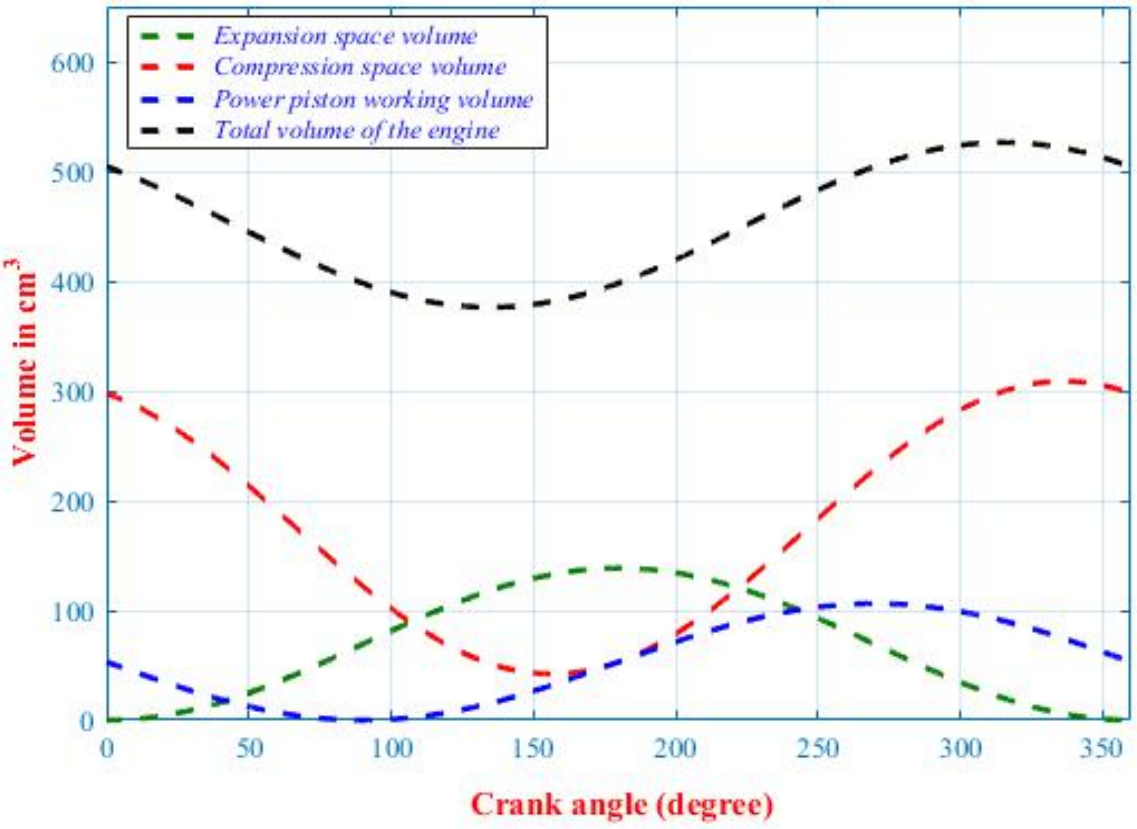

Figure 5.33: Variation of working space volume as a function of crank angle

Figure (5.33) shows how exactly working gas volume looks like inside the engine. The change of volume amplitude is increasing in expansion space and decreasing in compression space. In the engine's first cycle, the working gas volume is expanded due to rising gas temperature. In the second cycle, compression space volume increases while it decreases in expansion space.

Figure (5.34) represents the variation working fluid temperature in expansion and compression space as a function of crank angle. The temperature of the gas varies throughout the cycle of the engine. The cyclic temperature variation in expansion space is more considerable than that of compression space. The heat exchanger temperature is constant throughout the cycle. The average temperature of expansion space is less than that of the heater wall temperature, but it can be optimum for 150^0 crank angles. The temperature variation implies that the engine's ideal adiabatic performance is much less than that of theoretical efficiency, but it is approximately close to the realistic value of the experimental performance.

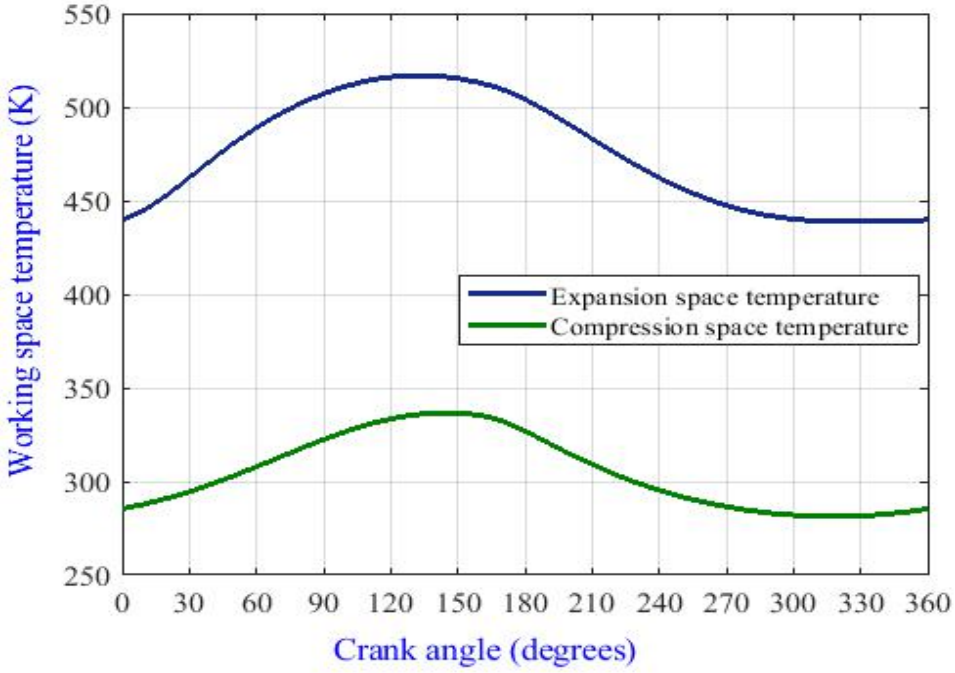

Figure 5.34: Impact of crank angle on expansion and compression space temperature

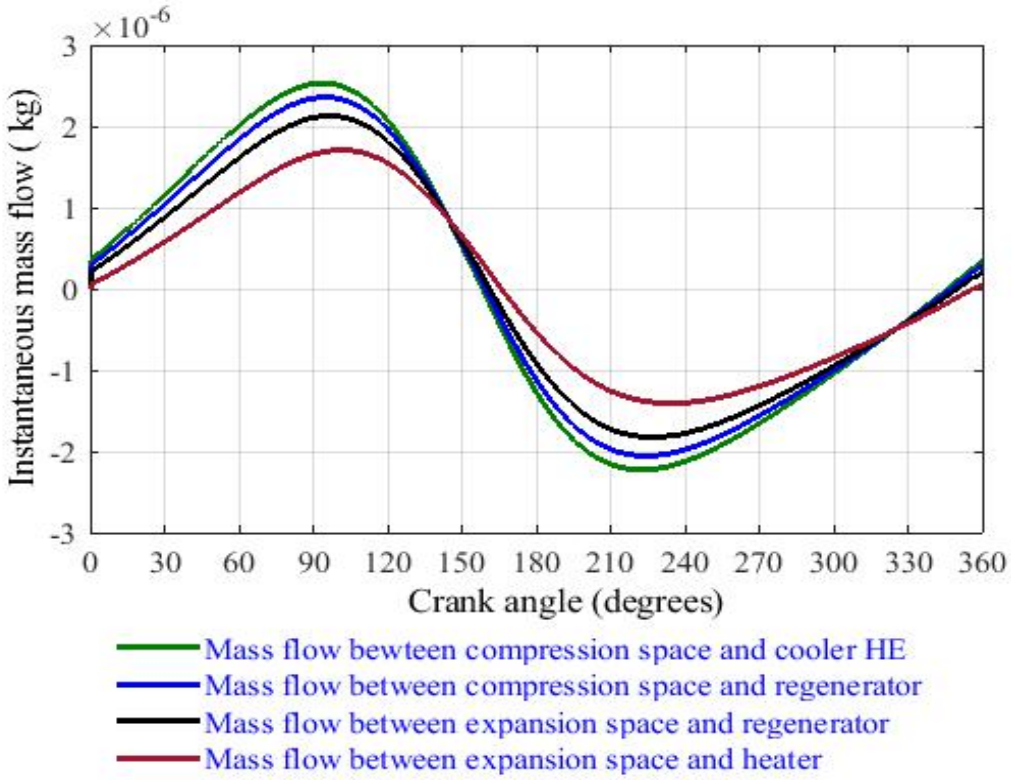

Figure 5.35: Instantaneous mass flow between heat each ex-changer and workspace

Figure (5.35) depicts the variation of working gas mass flow between the engine's control volumes as a crank angle function. As shown in the figure, the amplitude change is more during the mass flow between compression space and cooler heat exchanger and lower between expansion space and heater control volume.

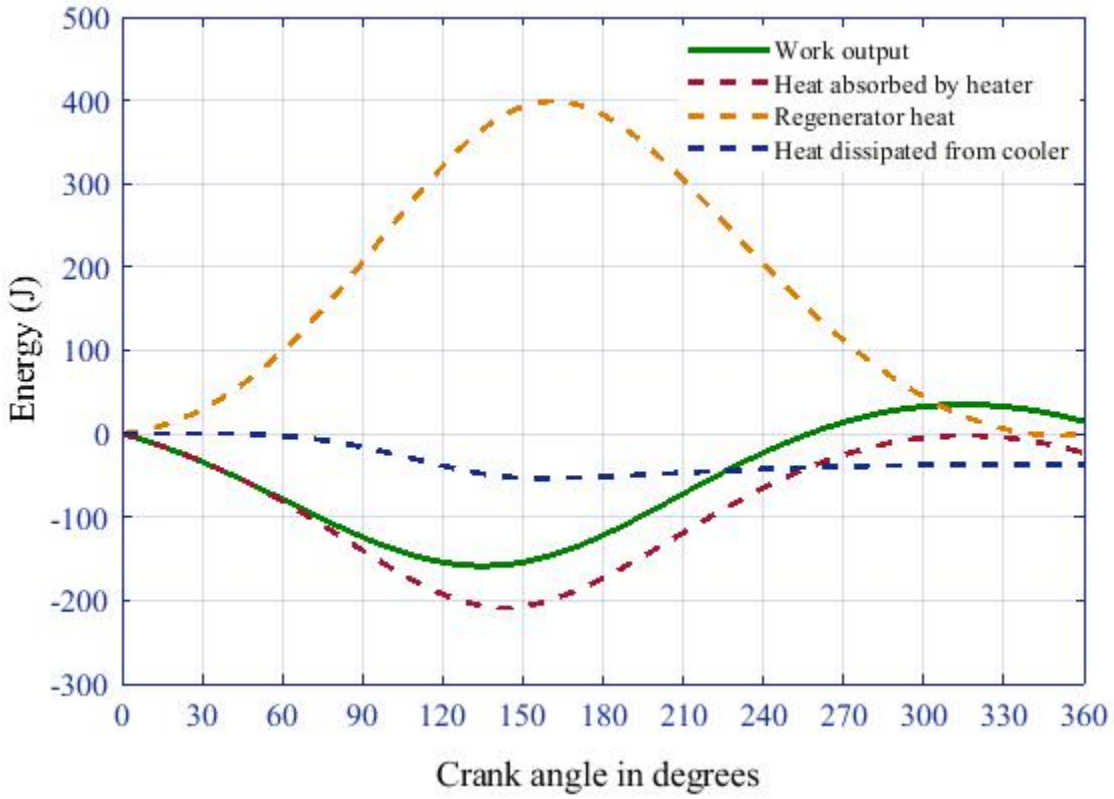

Figure 5.36: Heat and work-done (energy accumulation) as a function of crank angle

The variation of energy accumulation during the cycle of the engine with a crank angle is shown in figure (5.36). It can be seen that the amount of heat transferred to the regenerator is large during a cycle. This indicates more heat is stored in the first phase of the cycle and reuse back in the second phase of the cycle. The regenerator effectiveness also influences the output power and the performance of the engine. The net energy of the regenerator during the entire cycle is equal to zero. The heat absorbed by the heater heat exchanger and work-done by the engine decrease in the first half of the cycle and increases in the second half of the cycle.

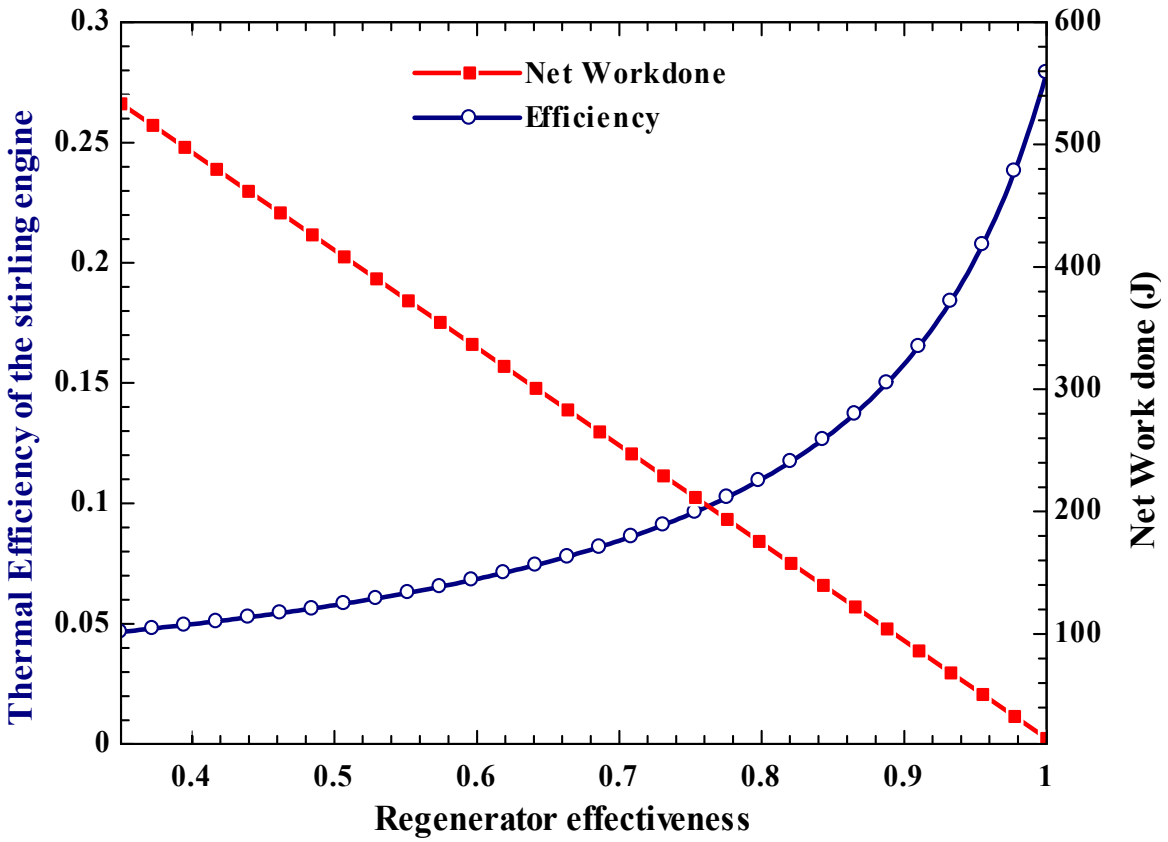

Figure 5.37: Effect of regenerator effectiveness on network-done and thermal efficiency of the engine

The figure depicts the impact of regenerator effectiveness on the Stirling engine's network done and thermal efficiency. The results show that the engine's network done is decreasing with increasing the effectiveness of the regenerator. In contrast, the ideal adiabatic thermal efficiency of the Stirling engine increases with increasing regenerator effectiveness. For a perfect regenerator, the thermal efficiency of Stirling becomes maximum. By varying the regenerator's effectiveness from 0.34 to 1, the Stirling efficiency is increased by 23.24%. In the ideal regenerator, the maximum thermal efficiency of the Stirling engine achieved is 27.96%.

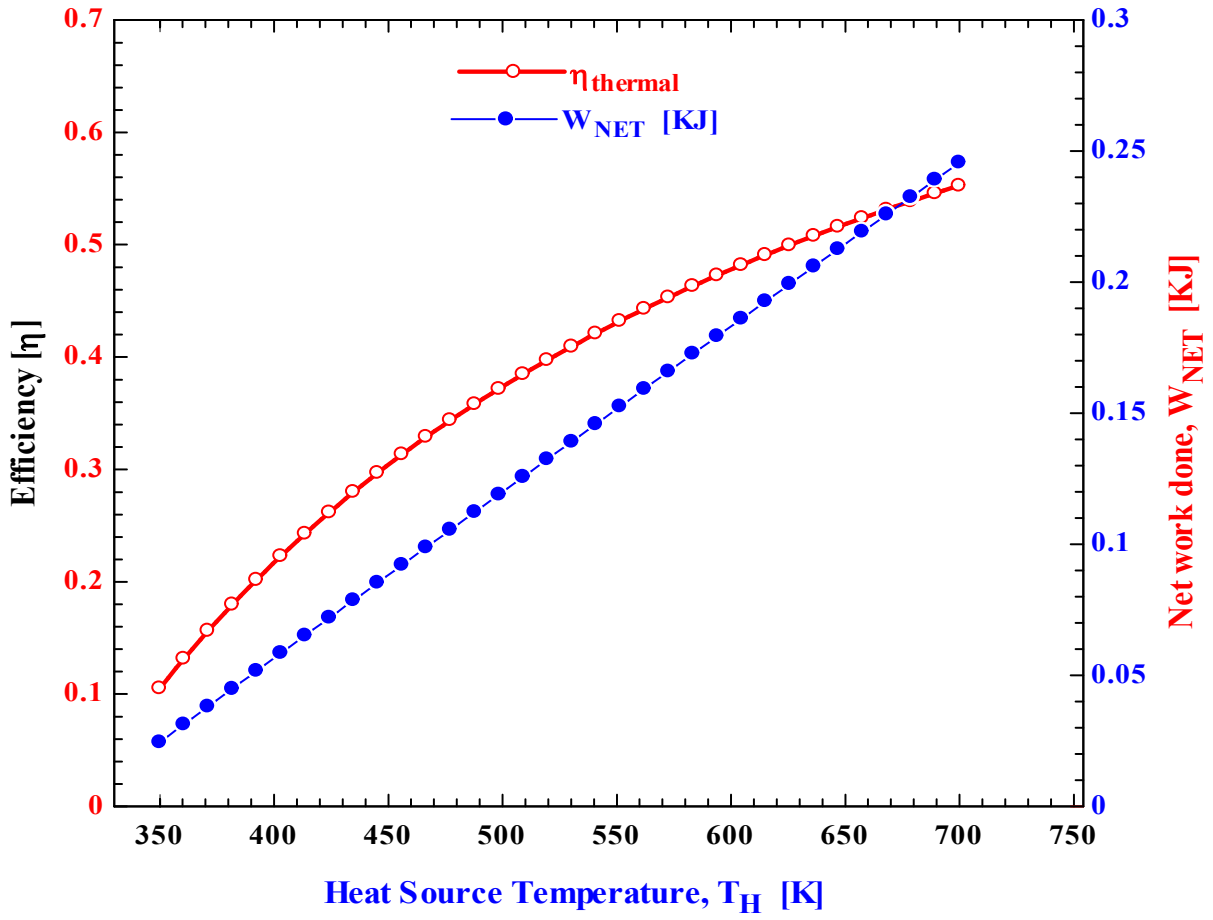

Figure 5.38: Effect of Heat Source Temperature on Efficiency and Net-Work done by The Engine

Figure (5.38) illustrates the effect of heat source temperature on the engine's network done and thermal efficiency. When the working fluid is maintained at a high temperature, the gas volume in expansion space expanded to increase the engine's expansion work. Since the work done by the engine is the sum of expansion work and compression work, increasing the hot side's temperature also raises the network done by the engine. On the other hand, increasing heat source temperature affects more the work done by the engine than that of heat supplied to the working gas, so that the engine's thermal efficiency increases.

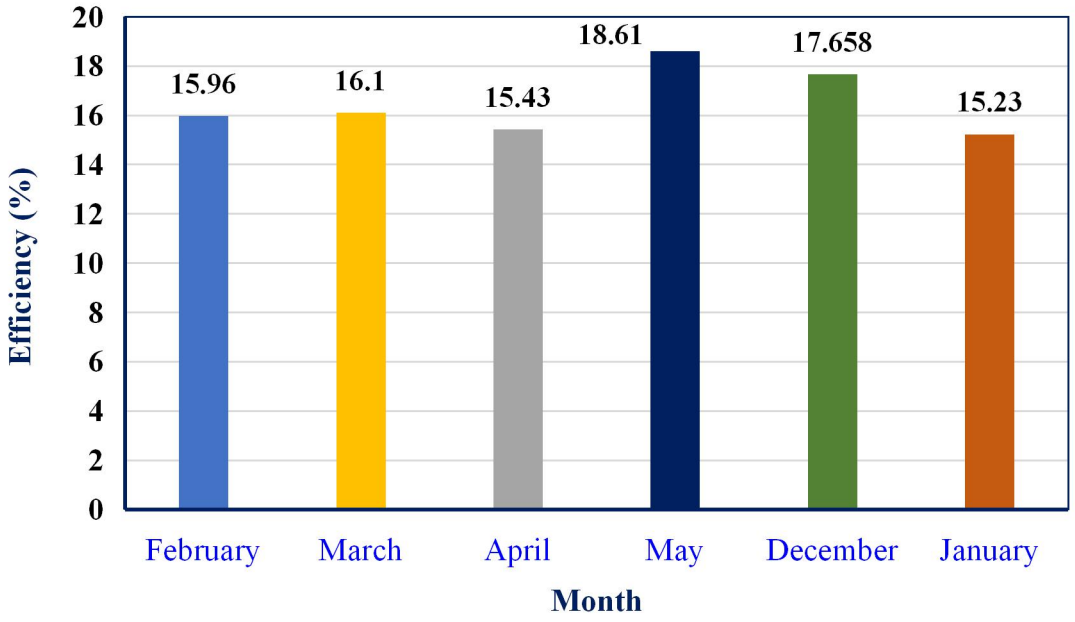

Figure 5.39: Ideal adiabatic thermal efficiency of the Stirling for selected irrigation period

The ideal adiabatic thermal efficiency of the Stirling varies for each month of the selected irrigation season. The thermal efficiency depends on the heat source temperature, and higher heat source temperature results in higher thermal efficiency. As shown in the above figure, the thermal efficiency is maximum in May with 18.61 % and minimum in January with 15.23 %. This indicates that the output power and the flow rate capacity required by the pump depending on the heat source temperature and available solar radiation. At high solar radiation, maximum thermal efficiency could be achieved due to the increasing heat source temperature for a given cooler heat exchanger temperature.

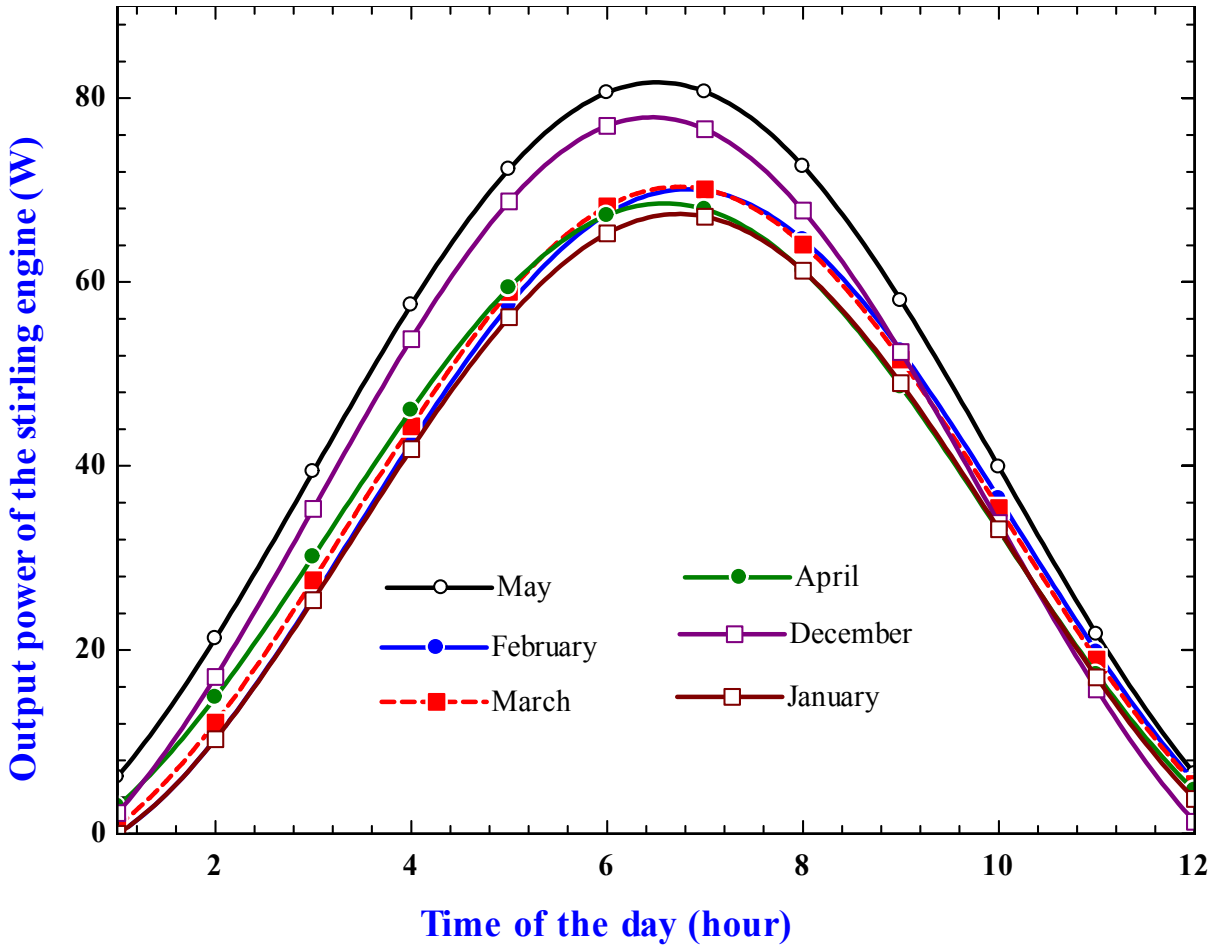

Figure 5.40: Variation of Stirling engine output power during a time of day for a given irrigation season

Figure (5.40) shows the variation of Stirling engine output power with a time of a day for a selected irrigation period. Since the heat source temperature varies with a beam of solar radiation during a sunny day, the Stirling engine's output power can be affected indirectly. As can be seen, the output power increases from sunrise to a maximum at mid-day before decreasing again until sunset. Higher beam solar radiation results in higher heat source temperature, so that higher output power of the Stirling engine. The result indicates that the output power is maximum at noontime with 80.68 W in May, 76.6 W in December, 70.6 W in March, 69.94 W in February, 67.9 W in April, and 67.1W in January as descending order.

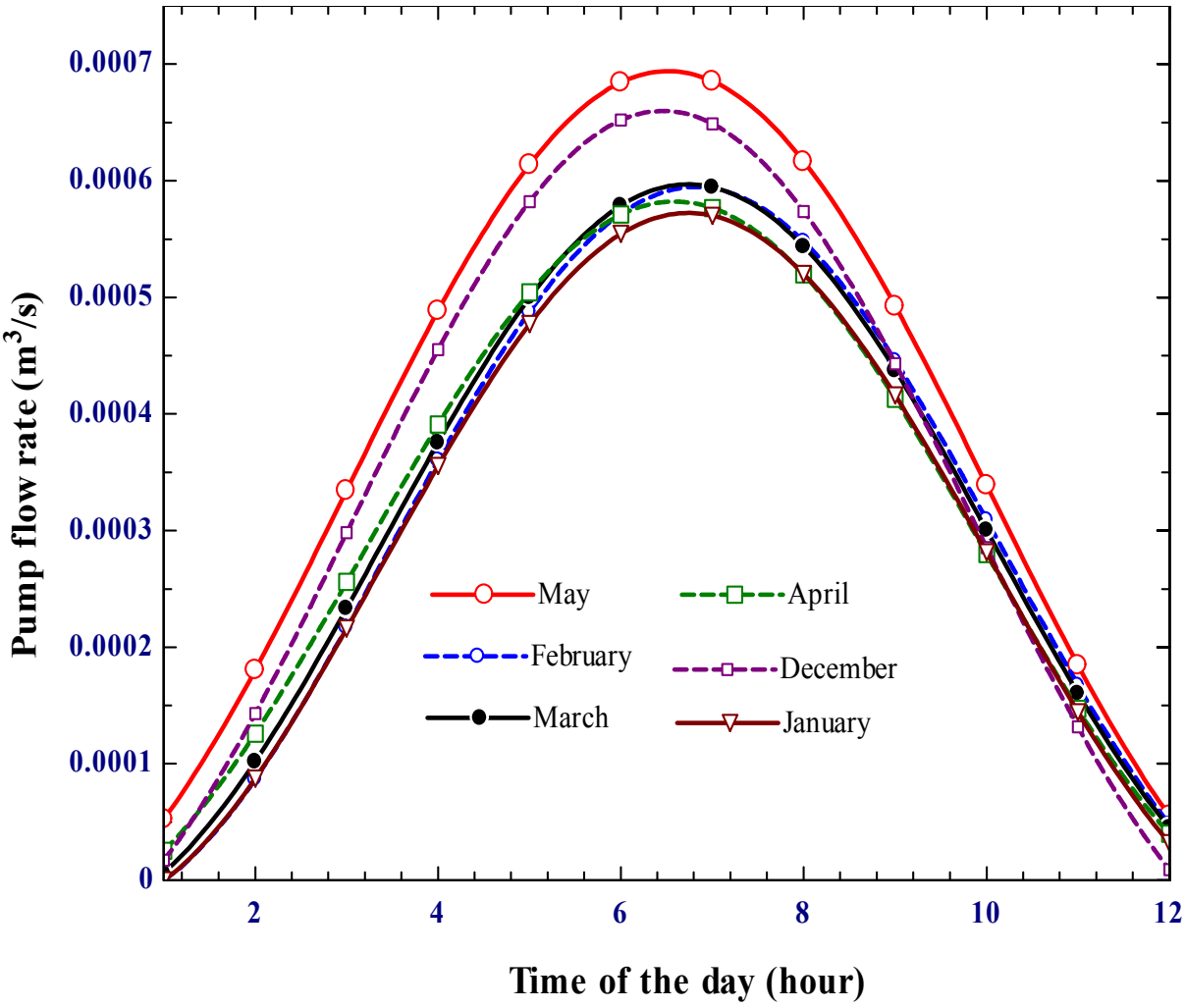

Figure 5.41: Variation of pump flow rate during a time of day for a given irrigation season

At a given total dynamic head, the pump's flow rate is influenced by the shaft power. As shown in figures (5.40) and (5.41), there is a linear relationship between the pump's output power and flow rate. Like power output, the pump's flow rate increases from sunrise to a maximum at noontime before decreasing again until sunset. The flow rate reaches a maximum in May, and during this time, the pump operates at maximum capacity to deliver the water to the irrigation field. By considering the engine's shaft power of 80.68 W and the centrifugal pump's efficiency of 85%, the hydraulic power required by the pump to deliver the water at the specific location should be 94.92 W. By taking into consideration the friction loss and suction head of the pump, for a dynamic head of 12 m, the pump flow rate found is 2.902 m^3/hrs.

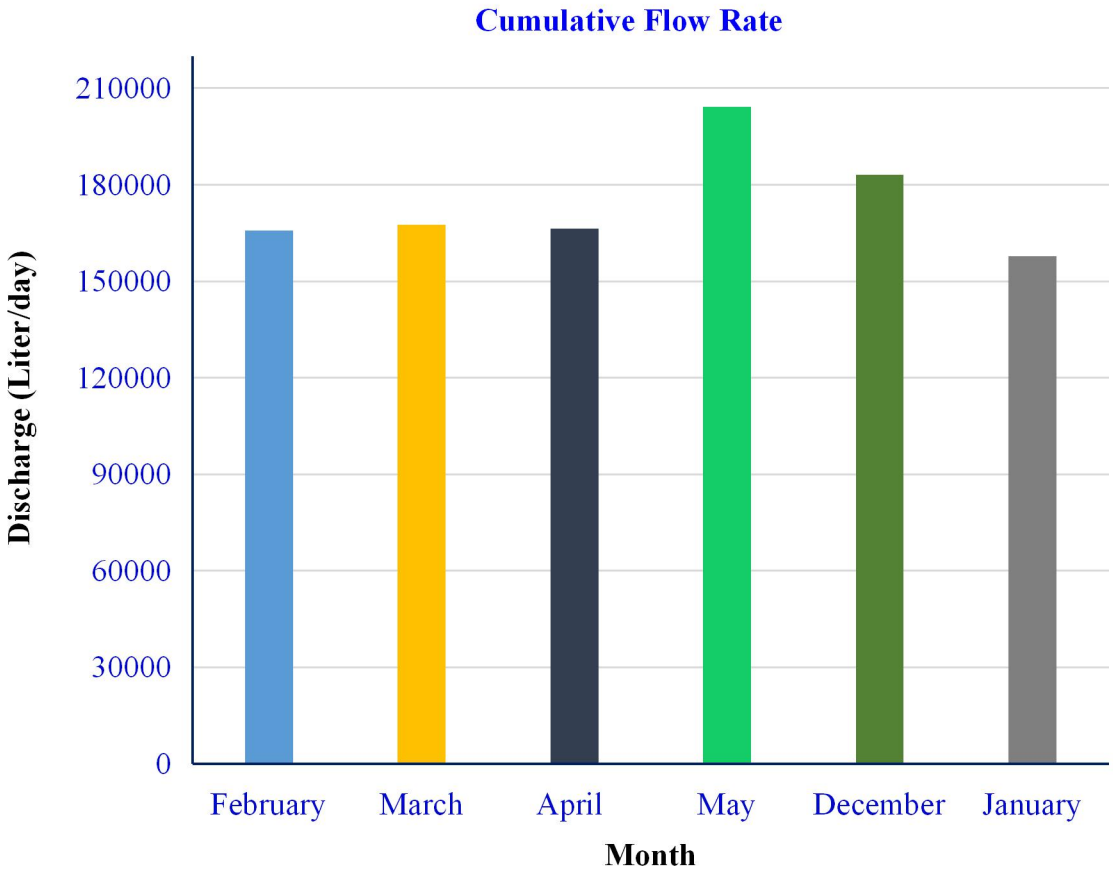

Figure 5.42: Cumulative flow rate of the pump for the selected irrigation period

For a given pump efficiency and static head, the pump flow rate depends on the output power generated by a Stirling engine. The pump capacity is varying in the selected irrigation period. Higher output power results in a higher flow rate at a given head. Figure (5.42) shows a cumulative flow rate of the pump for selected average days of each irrigation season. The result indicates that the pump has a minimum capacity in January with 157,839.8 liters per day and a higher capacity of 204,224.1 liters per day in May. The cumulative flow rate of the pump in February, March, and April are found to be 165,680.2 l/d, 167,505.9 l/d, and 166,272.04 l/d, respectively.

The performance curve of the pump represents the variation of the head as a function of discharge. The head and flow rate varies parabolically and usually represented by a quadratic equation. The figure (5.43) represented as H = - 0.09545 *Q^2 - 0.3614 *Q+15. As the head increases, the pump flow rate decrease and vice versa.

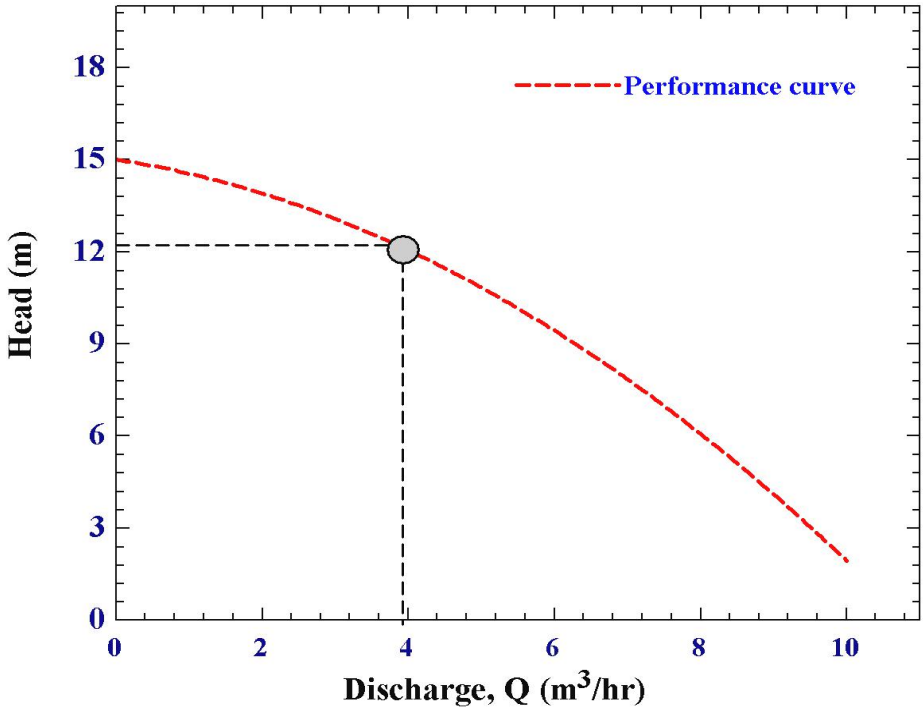

Figure 5.43: Performance curve of the pump (Head as a function of flow rate)

5.5 Scaling up and economic evaluation of the system

The system capacity required to meet the demand of water requirement for the irrigation field is estimated according to the equation stated in (4.69). The amount of water required for the crop is determined by evapotranspiration. Crop water requirement is the amount of water needed by a crop to grow or meet the loss through evapotranspiration. It depends on climate factors (sunshine, temperature, humidity, and wind velocity), crop type, and crop growth stage. For the sub-arid climate, the average crop water requirement is 26.66 mm per week [78].

By taking the irrigation efficiency 80 per cent, and assuming that the system operates eight hours per and six days per week, the amount of land area to be irrigated is estimated as follows;

$$A = \frac{(Q * H * D * E)}{(Net_{app})} \tag{5.1}$$

$$A = \frac{3.916 \left(\frac{m^3}{hr}\right) * (8hr) * 6 * 0.8}{26.66 * 10^{-3} m} = 0.463\ hectares$$

Based on the design of a unit system, the system's projection for 10 hectares of the irrigated area was carried out. As stated in the above equation, the system capacity to meet the water requirement depends on crop water need, irrigation efficiency, and area to be irrigated, and the system's operational performance.

As shown above, a single unit of the proposed system can irrigate up to 0.463 hectares or 4630 m^2 of land farm for a given pump flow rate of 3.917 m^3/hr or 128.117 W of hydraulic power.

By applying the same concept stated in equation (5.1), the hydraulic power required for a given land area could be estimated as;

$$P_P = \frac{A_P * P_S}{A_S} \tag{5.2}$$

Where; P_P is the hydraulic power required for the projection, A_P is an area given for the projection, A_S is an irrigated area for a unit system, and P_S is a hydraulic power from a unit system. By substituting the values into equation (5.3), the hydraulic power required to irrigate 10 hectares of farmland is as follows;

$$P_P = 10 * \frac{128.117W}{0.463} = 2767.1\ W\ or\ (2.767KW)$$

The amount of flow rate required by the system for the given irrigated area is evaluated as;

$$Q = \frac{0.367 * 2767.1}{12} = 84.627 \frac{m^3}{hr}$$

The total number of a proposed system required to meet the demand for 10 hectares of irrigated farmland is;

$$n = \frac{Q_P}{Q_S} = \frac{84.627}{3.917} = 21.6 \cong 22$$

So, around 22 series of the system can be required to irrigate 10 hectares through thermal Stirling pump. In another case, the amount of electric power produced through the thermoelectric generator for a single unit is 11.02 W. For the 22 series of dish concentrators coupled with TEG, the total electric power converted is 242.22 W. The energy generated through TEG is stored in the battery for the night pumping system and micro-electrification purposes. Otherwise, it can be used during the intermittence of solar radiation or as an energy source for the tracking system.

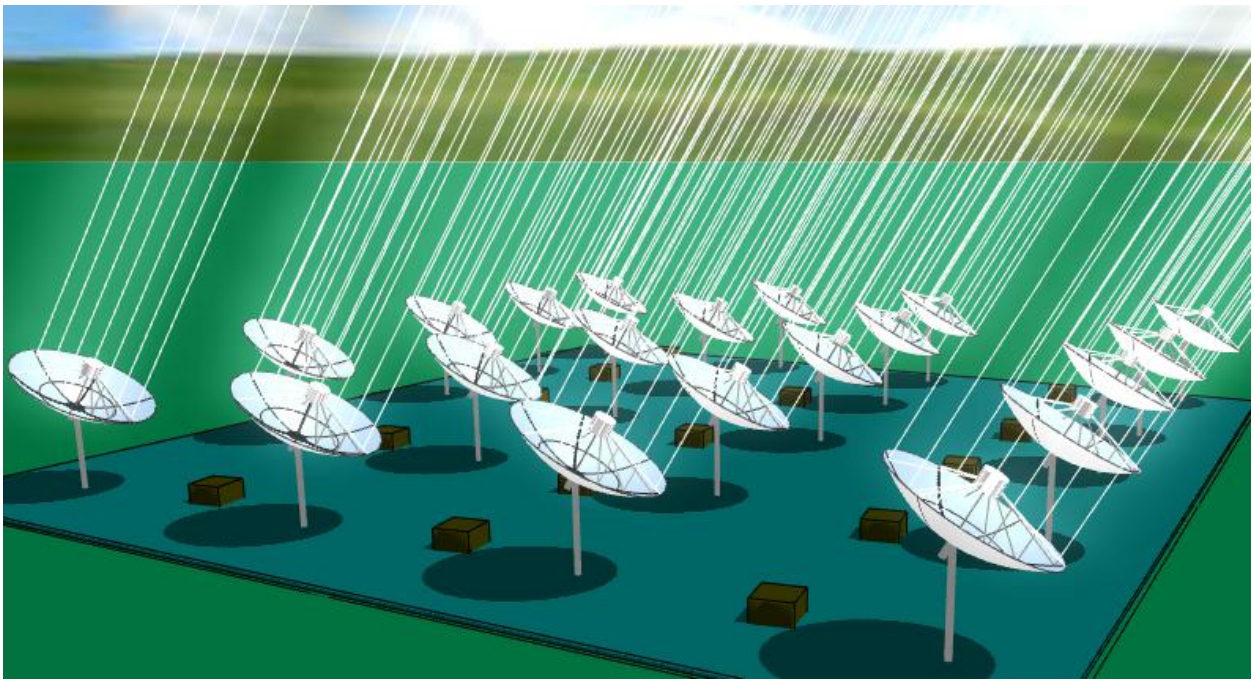

Figure 5.44: A series of dish concentrator coupled with TEG and Stirling engine

An economic evaluation of dish concentrator coupled with Stirling and TEG

The economic evaluation of the proposed system is required to show the economic viability in comparison with solar PV and diesel generator-based water pumping systems. To determine which system is most cost effective among the given alternative, the life cycle cost analysis is used. LCC involves initial investment, operation, maintenance, and replacement cost over its entire life span. LCC provides a better assessment of the cost for the long term, and all costs are adjusted to show the time value of money. Life cycle cost (LCC) analysis is a useful tool that

allows for an equal and useful comparison of solar and conventional water pumping technologies [79,81].

LCC of the concentrated solar power coupled with TEG and Stirling pumps includes initial capital investment, operation, maintenance costs, and replacement cost. The system's initial capital investment is the cost of manufacturing the concentrator, receiver, Stirling engine, thermoelectric generator, cooling system, electrical system, controlling system, transportation of the component to the site, and site preparation, and system installation. Operation and maintenance costs include the cost of labor, material, and maintenance. Replacement cost consists of the cost of replacement of the battery and is a function of the number of replacements over the plant lifetime.

The present value is given in terms of a future cash amount occurring at the end of year "n" and discount rate (d).

$$PV = F_n * \frac{1}{(1+d)^n} \tag{5.3}$$

Uniform present value also calculates the present value of a series of equal cash amounts (Ao) that repeat annually over a period of "n" year and discount rate (d).

$$PV = A_o * \frac{(1+d)^n - 1}{d * (1+d)^n} \tag{5.4}$$

The present worth factor is computed as;

$$P_R = \left(\frac{1+i}{1+d}\right)^n \tag{5.5}$$

Where; "i" is an inflation rate and "d" is a discount rate

LCC is estimated by adding the present worth of all costs of the components over the lifespan of the project. It is given as;

$$LCC = CC + OM + RC + FC \tag{5.6}$$

Where; CC is initial capital costs, OM is operation and maintenance cost, RC is replacement cost, and FC is fuel cost.

The projected lifespan is assumed to be 20 years, and the interest rate is assumed to be 5% in all calculations. The proposed system's daily energy demand for 10 hectares of the irrigation field is 2767.1 W. The battery can be replaced every five years, while the pump and controlling can be replaced every ten years by considering the time value of money. Two 150W batteries at the cost of $75 are considered to store the energy produced by TEG, and the replacement cost of the battery for five years, ten years, and 15 years are $58.76, $46.04, and $36.07, respectively. The pump and control system replacement costs are $1620.73 and $306.95, respectively.

Table 5.4: Life cycle cost analysis of dish concentrator coupled with TEG and thermal Stirling pump

Components	Initial capital cost ($)	Present worth ($)
Solar dish concentrator	3300	3300
Thermoelectric generator	1320	1320
Stirling engine [80]	2765.46	2765.46
Centrifugal pump	2640	2640
Centrifugal pump 10 years	2640	1620.73
Controlling system	1200	1200
Controlling system 10 years	1200	736.7
Battery (150 W)	75	75
Battery 5 years	75	58.76
Battery 10 years	75	46.04
Battery 15 years	75	36.07
Annual maintenance (1% CC)	45	900
	LCC	**$14698.76**

Comparative LCC analysis of the proposed model with PV pumping and diesel system

12 PV solar panels (235W each) are considered to meet the demand required to irrigate 10 hectares of land farm. The PV panel's total initial capital cost is $13835.5 by considering a $5/W peak cost [79]. For solar PV pump, $2400 is taken, which will be replaced every seven years, and $1020 for a pump controller, which is replaced every ten years.

The solar PV system's maintenance cost is assumed to be 2% of the initial capital cost. The PV pump's replacement cost for seven years and 14 years is $1705.63 and $1212.16, respectively. For the pump controller, by ten years, the replacement cost is $ 626.19.

Table 5.5: Life cycle cost analysis of PV solar pumping system

Components	Initial capital cost ($)	Present worth ($)
PV Solar Array	13835.5	13835.5
Submersible Pump	2400	2400
Submersible Pump 7 year	2400	1705.63
Submersible Pump 14 year	2400	1212.16
Pump Controller	1020	1020
Pump controller 10 year	1020	626.19
Annual Maintenance	276.71	5534.2
	LCC	**$26333.68**

Two 1.5 kW standard generator has been used to supply the same load, which costs $2/W peak and lifespan of 10 years. The initial cost of a diesel generator is $6000, and it consumes 1L/h of diesel oil [79]. The generator is assumed to operate six hours/day to cover the irrigation system's demand. The maintenance cost of the diesel generator system is taken as 10 % of the initial costs. The current price of diesel oil in Ethiopia is $0.488 per liter. Therefore, the annual fuel cost of the diesel generator is calculated as;

$$\text{Fuel consumption} = \text{Specific fuel consumption} * \text{Total operating hour} * \text{fuel rate}$$

$$F_C = 1\frac{L}{h} * \left(6\frac{h}{day} * 365\frac{day}{year}\right) * 0.488\frac{\$}{L} = 1068.75\frac{\$}{year}$$

The replacement cost of a diesel pump for five years, ten years, and 15 years is $ 2742.34, $2148.69, and $1683.56, respectively. For a pump controller, the replacement cost in five years, ten years, and 15 years are $783.526, $ 613.913, and $481.017, respectively. Since the pump generator's lifetime is assumed to be ten years, the replacement cost by considering the time value of money is $3683.47.

Table 5.6: Life cycle cost analysis of diesel generator pumping system

Components	Initial capital cost($)	Present worth ($)
Diesel generator	6000	6000
Diesel generator 10 year	6000	3683.47
Pump	3500	3500
Pump 5 year	3500	2742.34
Pump 10 year	3500	2148.69
Pump 15 year	3500	1683.56
Pump controller	1000	1000
Pump controller 5 year	1000	783.526
Pump controller 10 year	1000	613.913
Pump controller 15 year	1000	481.017
Fuel cost	1068.75	21375
Annual maintenance cost	600	12000
	LCC	**$56011.516**

The bar chart in figure (5.45) illustrates the life cycle cost comparison of the proposed system against solar PV and diesel water pumping systems. PV solar water pumping system has a higher initial capital cost than the proposed system and diesel water pumping system. However, the replacement cost, maintenance cost, and fuel cost are more increased in diesel water pumping systems. The comparison of life cycle cost between the system shows that the proposed system is more viable and feasible relative to PV and diesel generators. As can be seen from the LCC result, the proposed system's lifetime cost is 12% lower than PV solar and 443 % lower than diesel generator pumping systems for the same demands. So, the system is considered the most

cost-effective and economically feasible and encourages smallholder farmers in Ethiopia's rural area for a small scale irrigation system.

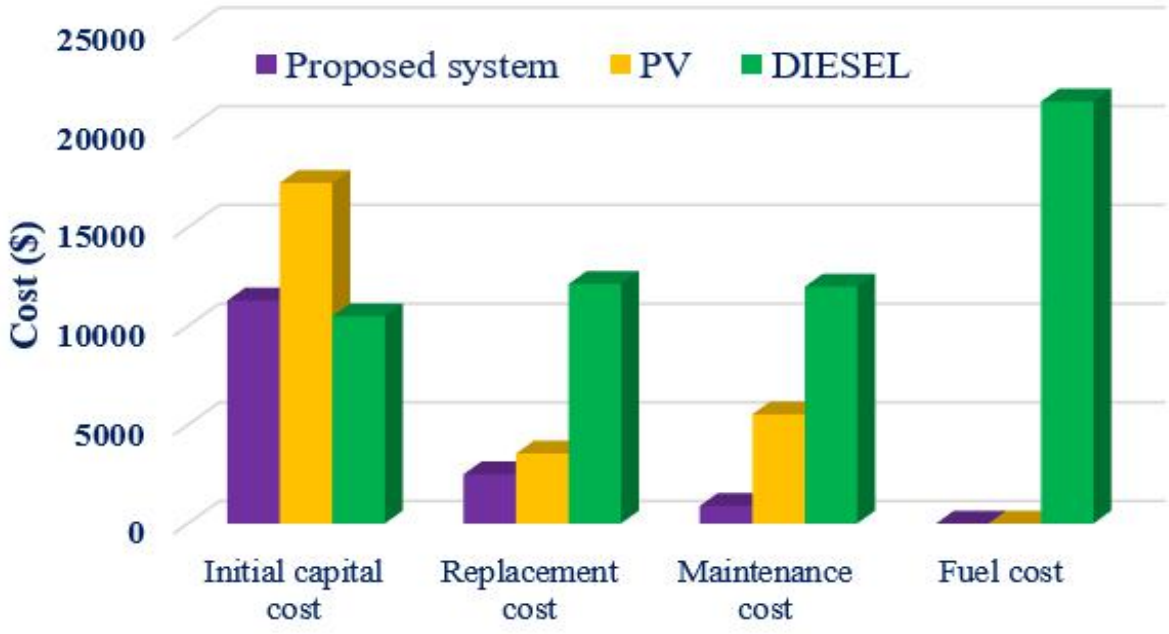

Figure 5.45: Life cycle cost comparison of the proposed system with PV and diesel water pumping system

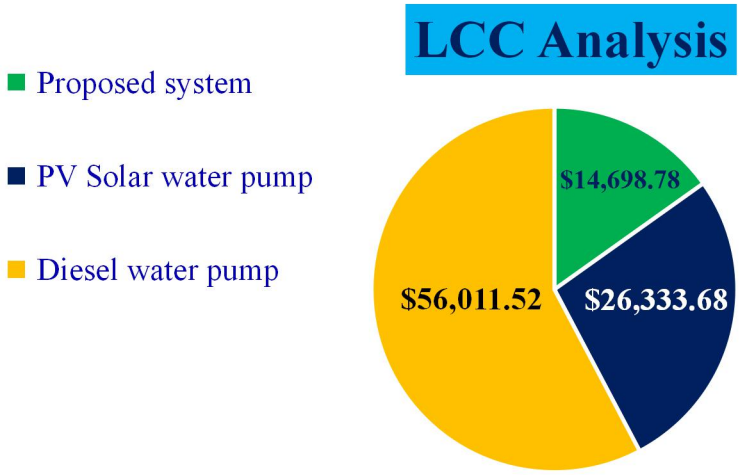

Figure 5.46: LCC comparison of the proposed system with PV solar and diesel water pumping system

CHAPTER SIX

6. CONCLUSION AND RECOMMENDATION

6.1 CONCLUSION

This paper presents a transient performance analysis of a solar dish concentrator integrated with Stirling and a thermoelectric generator for small-scale irrigation systems. The work involves weather data estimation in a study area, design and analysis of dish concentrator performance at different operating conditions, Multiphysics simulation of a thermoelectric generator, transient performance prediction of Stirling engine through a second-order analysis, projection and economic evaluation for small scale irrigation system.

The following conclusion was drawn from this work;

- The site has good potential of solar radiation for the irrigation system, and the predicted solar data shows good agreement against different software's.
- Based on evapotranspiration value, six months (December, January, February, March, April, and May) are considered as irrigation periods in the sites.
- The outlet fluid temperature, useful heat, and thermal efficiency increase with increasing the DNI. For 1000 W/m^2 of DNI, the dish concentrator's outlet fluid temperature and thermal efficiency are 488.2 K and 81.15%, respectively.
- Both heat flux and temperature at the concentrator's focal plane increases with increasing beam solar radiation. For 1000 W/m^2 of DNI, the average flux intensity and temperature distribution at the receiver of the concentrator reach 4.75MW/m^2 and 923K, respectively.
- At an operational temperature of 488.15 K on the module's hot side, TEG's electrical power and electrical efficiencies are 11.01 W and 3.715%, respectively. At a given absolute temperature of 405.6 K, the figure of merit and maximum conversion efficiency of TEG is 0.7256 and 5.366%, respectively.
- For the selected month of the irrigation season, the cumulative power generated by TEG during a day is maximum in May with an output power of 26.87 W and electrical efficiency of 2.78%.

- The Stirling engine's ideal adiabatic output power and thermal efficiencies are 108.96 W and 27.93%, respectively. The Stirling engine's thermal efficiency increases with increasing heat source temperature and regenerator effectiveness.
- Higher beam solar radiation leads to higher heat source temperature so that higher output power and thermal efficiency of the Stirling are achieved.
- The pump flow rate and power output are maximum at noontime during the sunny day, and at 128.12W of hydraulic power, the pump flow rate is 3.917 m^3/hr to deliver the water for the irrigation system.
- To irrigate 10 hectares of the land farm using the proposed system, 2767 W of hydraulic power or a flow rate of 84.6 m^3/hr is required to meet the demand.
- The proposed system's LCC value is 12% lower than PV and 43% lower than the diesel pumping system. So, the proposed system taken as cost-effective and economically feasible for the application of small-scale irrigation systems.

6.2 RECOMMENDATION

The following recommendation can be addressed for future research work.

- Further improvement of thermoelectric performance would be made by using a high ZT value of TEG material and considering different cooling methods.
- Experimental Investigation of the proposed system could be carried out to analyze the system's performance to compare with theoretical and numerical analysis.
- Future investigations are required to validate the kinds of conclusions that can be drawn from this study.
- Further work must be done to analyze and optimize the Stirling engine using the non-ideal adiabatic and CFD method.
- Analyzing a tracking system for parabolic dish concentrator and investigating how an incident angle affects the system's performance.
- Analysis of 3D solar flux intensity and temperature distribution at the absorber of the concentrator must be done for a detailed investigation of losses and improvement of thermal performance.

REFERENCE

[1]. Ferroukhi, R., Nagpal, D., Lopez-Pena, A., Hodges, T. Renewable Energy in the Water, Energy and Food Nexus. IRENA, Abu Dhabi.2015.

[2]. Ledent, J. United Nations Department of Economy and Social Affairs. World Urbanization Prospects: The 2018 Revision, Highlights.

[3]. Wazed, S.M., Hughes, B.R., O'Connor, D., Calautit, J.K. Solar Driven Irrigation System for Remote Rural Farms. Energy Procedia. 2017; 142: 184-191. **https://doi.org/10.1016/j.egypro.2017.12.030**

[4]. Unite Nation Annual Reports on human development, August 2019.

[5]. Agrawal, S., Jain, A. Sustainable deployment of solar irrigation pumps: Key determinants and strategies. Wiley Interdisciplinary Reviews. Energy and Environment. 2019; 2(3): e325. **https://doi.org/10.1002/wene.325**

[6]. Al-Saidi, M., Schellenberg, T., Roach, E. "Nexus Country Profiles: Ethiopia Nexus Research Focus," TH Köln - University of Applied Sciences. 2016. DOI:**10.13140/RG.2.2.35554.73923**

[7]. Mendes, D.M., Paglietti, L. Ethiopia: Irrigation market brief. FAO Investment Centre. Country Highlights. 2015.

[8]. Hordofa, T., Menkir, M., Bekele, S., Erkossa, T. Irrigation and rain-fed crop production system in Ethiopia. 2015. **https://hdl.handle.net/10568/38244**

[9]. Tesfaw, M.Small Scale Irrigation Development. Irrigation and Drainage System Engineering .2018; 7(1). **https://doi.org/10.4172/2168-9768.1000206**

[10]. Tesfaye, A., Bogale, A., Namara, R.E. The Impact of Small-Scale Irrigation on Household Food Security: The Case of Filtino and Godino Irrigation Schemes in Ethiopia Irrigation.2012

[11]. Isaias, D.M.S., Cuamba, B.C., Leao, A.J. A Review on Renewable Energy System for Irrigation in Arid and Non-Arid Regions. Journal of Power and Energy Engineering.2019; 7:21-58. **https://doi.org/10.4236/jpee.2019.710002**

[12]. Dubey, K.K., Mishra, R.S., Sinha, G.P. Thermodynamic Analysis of a Solar Thermal Syphon Pump. International Journal of Advanced Research and Innovation. 2014; 2(3):568-573.

[13]. Wazed, S.M., Hughes, B.R., O'Connor, D., Calautit, J.K. A Review of Sustainable Solar Irrigation Systems for Sub-Saharan Africa. Renewable and Sustainable Energy Reviews. 2018; 81: 1206-1225. **https://doi.org/10.1016/j.rser.2017.08.039**

[14]. Hadi, S.M., Owaid, A.I., Ahmmed, R.A. Performance Optimization of Hybrid Solar Heating System Using Thermoelectric Generator. International Journal of Advanced Research in Engineering and Technology.2016; 7(2): 9-20.

[15]. Nenad, M., Wang, E.N. Modeling and Optimization of Hybrid Solar Thermoelectric Systems with Thermosiphons. Solar Energy.2011; 85(11):2843-2855. **https://doi.org/10.1016/j.solener.2011.08.021**

[16]. Nayak, A., Nayak, R.K. A computational approach thermoelectric power generator to estimate heat flux. Journal of mechanical engineering and sciences.2019;13(1):4718-4742

[17]. Kumar, P.M., Babu, V.J., Subramanian, A., Bandla, A., Thakor, N., Ramakrishna, S., Wei, H. The Design of Thermoelectric Generator and Its Medical Applications. Journal of Design. 2019. **https://doi.org/10.3390/designs3020022**

[18]. Feiyang, S., Minghou, L., Lv, S., He, W., Hu, Z., Jinwei, M., Chen, H. Experimental investigation of solar thermoelectric (STEG) co-generation system. International Conference on Applied Energy. 2019; 158: 892-897. **https://doi.org/10.1016/j.egypro.2019.01.227**

[19]. Barbosa, F.V., Afonso, J.L., Rodrigous, F.B., Teixeira, J.C. Development Of Solar Concentrator With Tracking System. Mechanical Science.2016. **https://doi.org/10.5194/ms-7-233-2016**

[20]. Lertsatitthankorn, C., Jamradloedluk, J., Rungsiyopas, M. Electricity generation from a solar parabolic concentrator coupled to a thermoelectric module. Energy Procedia.2014; 52:150-158. **https://doi.org/10.1016/j.egypro.2014.07.065**

[21]. Muthu, G., Shanmugam, S., Veerappan, A. Solar parabolic dish thermoelectric with acrylic cover. Energy Procedia.2014; 54:2-10. **https://doi.org/10.1016/j.egypro.2014.07.244**

[22]. Çolak L., Kıllış, B. Irrigation by PHVT system. *Global Journal on Advances in Pure & Applied Sciences*.2014; 2:116-123. Available from: **http://www.world-education center.org/index.php/paas**

[23]. Bamroongkhan, P., Lertsatitthanakorn, C., Soponronnarit, S. Experimental performance study of a solar parabolic dish photovoltaic-thermoelectric generator. Energy Procedia. 2019; 158: 528-533. **https://doi.org/10.1016/j.egypro.2019.01.147**

[24]. https://en.m.wikipedia.org/wiki/fiche.Accessed in July 2020.

[25]. Duffie, J. A., Beckman, W. A. Solar Engineering of Thermal Processes.4th edition. New Jersey: John Wiley & Sons; 2013.

[26]. Xiao, M., Yu, Z., Cui, Y. Evaluation and Estimation of Daily Global Solar Radiation from The Estimated Direct and Diffuse Solar Radiation. Journal of Theoretical and Applied Climatology. Springer, 2020. **https://doi.org/10.1007/s00704-020-03140-4**

[27]. https://globalsolaratlas.info/download/ethiopia. Accessed in September 2020.

[28]. Maleki, S.A.M., Hizam, H., Gomes, CH. Estimation of Hourly, Daily, and Monthly Global Solar Radiation on Inclined Surfaces: Models Re-Visited. Journal of Energies, MPDI. 2017. **https://doi.org/10.3390/en10010134**

[29]. Zegeye, M., Tadiwos, T., Aman, A. Optimal Sizing of Solar Water Pumping System for Small Scale Irrigation: Case Study of Dangila. International Journal of Renewable and Sustainable Energy.2014; 3(5):99-107. **https://doi.org/10.11648/j.ijrse.20140305.13**

[30]. Kalogirou, S.A. Solar Thermal Collectors and Applications. Journal of Energy and Combustion Science. 2004; 30:231-295.

[31]. Missana, W.P., Park, E., Kivevele, T. Thermal Performance Analysis of Solar Dryer Integrated with Heat Energy Storage System and A Low-Cost Parabolic Solar Dish Concentrator for Food Preservation. Journal of Energy. 2020**.** **https://doi.org/10.1155/2020/9205283**

[32]. https://parabola-calculator.software.informer.com/2.0/. Accessed August 2020.

[33]. Thakkar V, Doshi A, Rana A. Performance Analysis Methodology for Parabolic Dish Solar Concentrator for Process Heating Using Thermic Fluid. IOSR. J Mech Civ Eng 2015; 12(1):101–14.**https://doi.org/10.9790/1684-121210114**

[34]. Hafez, A.Z., Soliman, A., El-Metwally, K.A., Ismail, I.M. Solar Parabolic Dish Stirling Engine System Design, Simulation, and Thermal Analysis. Energy Conversion and Management. 2016; 126:60-75. **https://doi.org/10.1016/j.enconman.2016.07.067**

[35]. Craig, O.O, Dobson, R.T. "MSc Thesis on Stand Alone Parabolic Solar Cooker for African Conditions" .2015

[36]. Hafez, A.Z., Soliman, A., El-Metwally, K.A., Ismail, I.M. Design Analysis Factors and Specifications of Solar Dish Technologies for Different Systems and Applications. Renewable and Sustainable Energy Reviews. 2017; 67:1019-1036. **https://doi.org/10.1016/j.rser.2016.09.077**

[37]. Skouri, S., Bouadila, S., Nassrallah, S.B. Improvement of Solar Parabolic Concentrator Thermal Efficiency Correlated to Different Factors. IOSR Journal of Mechanical and Civil Engineering .2017; 67-73. **https://doi.org/10.9790/1684-16053026773**

[38]. Stine, W.B., Diver, R.B. A compendium of solar dish/Stirling technology; 1994.

[39]. Fraser, P.R. Stirling dish system performance prediction model. (Doctoral dissertation). University of Wisconsin-Madison; 2008.

[40]. Sup, B.A., Zainudin, M.F, Ali T.Z.S, Bakar R.A, Ming, G. L. Effect of rim angle to the flux distribution diameter in solar parabolic dish collector. Energy Procedia, 2015; 68:45–52. **https://doi.org/10.1016/j.egypro.2015.03.231**

[41]. Kribus A, Kaftori D, Mittelman G, Hirshfeld A, Flitsanov Y, Dayan A. A miniature Concentrating photovoltaic and thermal systems. Energy Conversion Management. 2006; 47(20):3582–90. **https://doi.org/10.1016/j.enconman.2006.01.013**

[42]. Wu, S.Y., Xiao, L., Cao, Y., Li, Y.R.A Parabolic Dish/AMTEC Solar Thermal Power System and Its Performance Evaluation, Applied Energy.2009;87:452–462. **https://doi.org/10.1016/j.apenergy.2009.08.041**

[43]. Gholamalizadeh, E., Chung, J.D. Exergy Analysis of a Pilot Parabolic Dish-Stirling System. Journal of Entropy.2017. **https://doi.org/10.3390/e19100509**

[44]. Yang, S., Wang, J. Lund, P.D., Jiang, Ch., Liu, D. Assessing the Impact of Optical Errors in A Novel 2-Stage Dish Concentrator Using Monte-Carlo Ray-Tracing Simulation. Renewable Energy.2018; 123:603-615. **https://doi.org/10.1016/j.renene.2018.02.034**

[45]. Wendelin, T., Dobos, A., Lewandowski, A., 2013. SolTrace: A Ray-Tracing Code for Complex Solar Optical Systems, National Renewable Energy Laboratory.2013; 15013. NREL/TP-5500-59163. **http://www.nrel.gov/csp/soltrace/download.html**

[46]. Pavlovic S.R., Stefanovic, V.P., Dr. Sci, R.P., Petrovic, E.P., Ayed, S. Ray Tracing Study to Determine the Characteristics of the Solar Image in the Receiver for A Thermal Solar Concentration System. Journal of Solar Energy 2015(3):1-10. **http://dx.doi.org/10.1155/2015/326536**

[47]. Cherif, H., Ghomrassi, A., Sghaier, J., Mhiri, H., Bournot, Ph. A Receiver Geometrical Details on a Solar Parabolic Dish Collector Performance. Energy Reports.2019; 5:882-897. **https://doi.org/10.1016/j.egyr.2019.07.010**

[48]. COMSOL Multiphysics V5.5, a Heat Transfer Module User's Guide. Stockholm, Sweden (2012).

[49]. Ngendahayo, A. Design, Modeling, and Fabrication of Thermoelectric Generator for Waste Heat Recovery in Local Process Industry. Master Thesis. 2017

[50]. Prasad, A., Thiagarajan, R. Multiphysics Modelling and Multilevel Optimization of Thermoelectric Generator for Waste Heat Recovery. COMSOL Conference. 2018

[51]. Specification of the thermoelectric module. https://www.thermonamic.com.cn. Accessed October 2020.

[52]. Cengel, Y.A, Klein, S., Beckman, W. Heat transfer: a practical approach. Boston: WBC McGraw-Hill.1998.

[53]. Ramadan, M.Y. K. Hybrid Solar Thermo-Electric Systems for Combined Heat and Power. PhD. Dissertation Cardiff University.2014

[54]. Hogblom, O., Andersson, R. Analysis of Thermoelectric Performance by Use of Simulation and Experiments. Journal of Electronic Materials.2014;43(6):2247-2254 **https://doi.org/10.1007/s1164-014-3020-x**

[55]. Patowary R, Baruah DC. Feasibility study of TEG-integrated biomass cookstove for electrical power generation specific to rural areas with inadequate electricity. Energy Sources, Part A: Recovery, Utilization, and Environmental Effects. 2019; 13:1-22. **https://doi.org/10.1080/15567036.209.1673503**

[56]. Sundarraj, P., Taylor, R.A., Banerjee, D., Maity, D., Roy, S.S. Experimental and Theoretical Analysis of A hybrid Solar Thermoelectric Generator with Forced Convection Cooling. Journal of Physics. 2017. **https://doi.org/10.1088/1361-6463/50/1/015501**

[57]. Koysal, Y. Performance Analysis on Solar Concentrating Thermoelectric Generator Coupled with Heat Sink. International Journal of Precision Engineering and Manufacturing. 2018. **https://doi.org/10.1007/s12541-019-00060-w**

[58]. Miljkovic, N., Evelyn, N. W. Modeling and Optimization of Hybrid Solar Thermoelectric Systems with Thermosyphons. Solar Energy. 2011; 85(11):2843-2855. **https://doi.org/10.1016/j.solener.2011.08.021**

[59]. Kanimba, E., Tian, Zh. Modeling of a Thermoelectric Generator Device. INTECH.2016. Chapter 18, **Http://Dx.Doi.Org/10.5772/65741**

[60]. Muthu, G., Thulasi, S., Dhinakaran, V., Mothilal, T. Performance of solar parabolic dish thermoelectric generator with PCM, Materials Today: Proceedings.2020. **https://doi.org/10.1016/j.matpr.2020.06.123**

[61]. Nasri, W., Djebali, R., Dhaoui, S., Abboudi, S., Kharroubi, H. Finite Elements Multiphysics Investigation of Thermoelectric System for Electricity and Cooling Generation. International Journal of Modern Studies in Mechanical Engineering.2017;3(4):1-13

[62]. Tian, H., Sun, X., Jia, Q., Liang, X., Shu, G., Wang, X. Comparison and Parameter Optimization of Segmented Thermoelectric Generator by Using the High-Temperature Exhaust of a Diesel Engine. Energy Journal. 2015; 84:121-130. **http://dx.doi.org/10.1016/j.energy.2015.02.063**

[63]. Bumataria, R.K, Patel, N.K. Review of Stirling Engine for Pumping Water Using Solar Energy as a Source of Power. International Journal of Engineering Research and Applications. 2013; 3(1):864-868.

[64]. Prof. Dr. Dosli Bin Abu Bakar. Stirling Engines: Operational Theory, Development History, Design Configuration, and Applications. 2019.

[65]. Martini, W.R. Stirling Engine Design Manual, 2nd Ed. NASA CR-168088. 1983

[66]. Hirata, K. Schmidt Theory for Stirling Engines. National Maritime Research Institute. **http://www.nmri.go.jp/envi/khirata/**

[67]. Dyson, R.W, Wilson, S., Tew, R.C. Review of Computational Stirling Analysis Method. Second International Energy Conversion Engineering Conference. 2004. **https://doi.org/10.2514/6.2004-5582**

[68]. Synman, H., Harms, T.M, Strauss, J.M. Design Analysis Methods for Stirling Engines. Journal of Energy in Southern Africa.2008; 19(3).

[69]. Urieli, I., Berchowitz, D. Stirling Cycle Machine Analysis. Adam Higler.1984

[70]. Chaharaghi, M., Sheykhi, M. Energy and Exergy Analyses of Beta Type Stirling Engine at Different Working Conditions. Energy Conversion and Management.2018; 169:279-290. **https://doi.org/10.1016/j.enconman.2018.05.064**

[71]. Hirve, N.S.Thermodynamics Analysis of a Stirling Engine Using Second-Order Isothermal and Adiabatic Models for Application in Micropower Generation Systems. Master Thesis., 2015.

[72]. http://irrigation.wsu.edu/Content/Calculators/Center-Pivot/System-Pumping-Requirements.php; September 2, 2020.

[73]. Ramos, J.A.A. Thermodynamics Analysis of Stirling Engine Systems: Application for Heat and Power. Dissertation.2015

[74]. Roldan, C., Pieretti, P., Solórzano, L.R. Conceptual and Basic Design of Stirling Engine Prototype for Electrical Power Generation Using Solar Energy.ASME.2010. **https://doi.org/10.1115/ES2010-90384**

[75]. Thombare, D.G., Verma, S.K. Technological Development in the Stirling Cycle Engines. Renewable and Sustainable Energy Reviews. 2008; 12:1-38. **https://doi.org/10.1016/j.rser.2006.07.001**

[76]. Dong, S., Shen, G., Xu, M., Zhang, S., An, L. The effect of working fluid on the performance of a large-scale thermoacoustic Stirling engine. Energy.2019; 181:378-86. **https://doi.org/10.1016/j.energy.2019.05.142**

[77]. Sharaf Eldean, M.A., Rafi, K.M., Soliman, A.M. Performance Analysis of Different Working Gases for Concentrated Solar Gas Engines: Stirling & Brayton.2019; 150:651-668. **http://dx.doi.org/10.1016/j.enconman.2017.08.008**

[78]. **http://www.fao.org/chapter_three_crop_water_needs/**. Accessed December 9, 2020.

[79]. Girma, Z. Techno-economic analysis of photovoltaic pumping system for rural water supply in Ethiopia, International Journal of Sustainable Energy.2015. **http://dx.doi.org/10.1080/14786451.2015.1017498**

[80]. Girma, M., Assefa, A., Molinas, M. Feasibility Study Of A Solar Photovoltaic Pumping System For Rural Ethiopia. Environmental Science.2015.

[81]. Krishnaiah, T., Srinivasa Rao, S., Madhumurthy, K. The Life Cycle Cost Analysis of a Solar Stirling Dish Power Generation System, Energy Sources, Part B: Economics, Planning, and Policy. 2012; 7 (2):131-139. **http://dx.doi.org/10.1080/15567240903047566**